Experimental Evidence of the Phobos Magnetic Field[1]

V. G. Mordovskaya*, V. N. Oraevsky, V. A. Styashkin, and J. Rustenbach[1]

Institute of Terrestrial Magnetism, the Ionosphere, and Radiowave Propagation,
Russian Academy of Sciences, Troitsk, Moscow region, 142092 Russia
* e-mail: valen@izmiran.rssi.ru
[1] Max-Plank-Institut fur extraterrestrische Physik, 12489 Labor Berlin, Berlin, Germany
Received August 7, 2001

A detailed analysis of the disturbances of a magnetic field near Phobos was carried out. Two types of force lines were found. Some of them correspond to the force lines of the solar wind disturbed by an obstacle. The others are related to Phobos. The character and the direction of the disturbances give strong evidence for the existence of the Phobos magnetic field and magnetosphere. Assuming the dipole approximation, the value of magnetic field of Phobos at its surface is 0.6 G. It is comparable to the magnetic field at the surface of the Earth. © *2001 MAIK "Nauka/Interperiodica".*

PACS numbers: 96.30.Gc; 96.35.Kx

1. The origin of planets and planetary bodies is one of the basic problems of the research in the Solar System. The Phobos exploration is of special interest. According to the modern concepts, Phobos refers to seized asteroid bodies, and its substance may carry information about the origin and evolution of the Solar System.

In July 1988, two probes were launched to Phobos for studying Mars and Phobos. It was the expansive program developed by scientists of the Soviet Union in collaboration with the participations from many other countries.

In March 1989, *Phobos-2* approached Phobos at a distance of 180–400 km and was placed in a "quasi-synchronous" orbit. Figure 1 gives the examples of the satellite trajectory relative to Phobos. The satellite was orbiting on a circular trajectory. It approached Phobos to a distance of 180 km and moved away from it by 400 km. Simultaneously, the satellite, together with Phobos, rotated around Mars. Figure 1 is the scheme of the orbit around Mars and the coordinate system used. The X axis points to the Sun, the Y axis is opposite to the direction of Mars movement around the Sun, and the Z axis completes the coordinate system. Thus, the satellite approached Phobos three times a day to a distance of 180 km from the Phobos dayside (P). In addition, the satellite approached Phobos three times a day on the Phobos and Mars night side (M). The labels P and M indicate this situation. The location of the Mars bow shock, deduced from the *Phobos-2* data, is shown by the solid line. We will consider the magnetic events

for the P field. The magnetic events relate only to the vicinity of Phobos.

Eroshenko [1] pointed out the existence of an obstacle near Phobos. The effects of local depression of a magnetic field near the Phobos orbit were considered in [2]. We carried out very thorough study of the magnetic-field data near Phobos and arrived at an unexpected conclusion. Phobos has a magnetic field. It is probable that the Phobos magnetic field and the Mars crystal magnetism, discovered by the Mars Global Surveyor MAG/ER experiment [3], have a common nature.

2. The overview of the magnetic-field measurements near Phobos. Aboard the spacecraft, the magnetic-field measurements were carried out by two magnetometers, FGMM and MAGMA. The description of the devices and the first results can be found in [4].

The general review of the measurements of the magnetic field B on the "quasi-synchronous" orbits from March 22 to March 26, 1989, is given in Fig. 2. The label P marks the measurements of the magnetic field on the Phobos dayside upon approaching it at 180 km. The behavior and the value of magnetic field attract attention from 20:00 to 22:00 on March 22, 1989. The measured value of the modulus of magnetic field *B* was 17 nT at this period on the Phobos dayside. It is a higher than the value *B* measured earlier in the Mars tail.

Let us now consider the events that occurred at times the satellite (CA) approached Phobos at 180 km from the dayside. Every time, the magnetometers detected distinct disturbances of the magnetic field. One can see either structured disturbances or simple disturbances of the magnetic field. The review of the magnetograms gives only a rough idea of the phenomena.

3. Analysis of the magnetic disturbances. For better understanding of the phenomenon, we draw the gra-

---

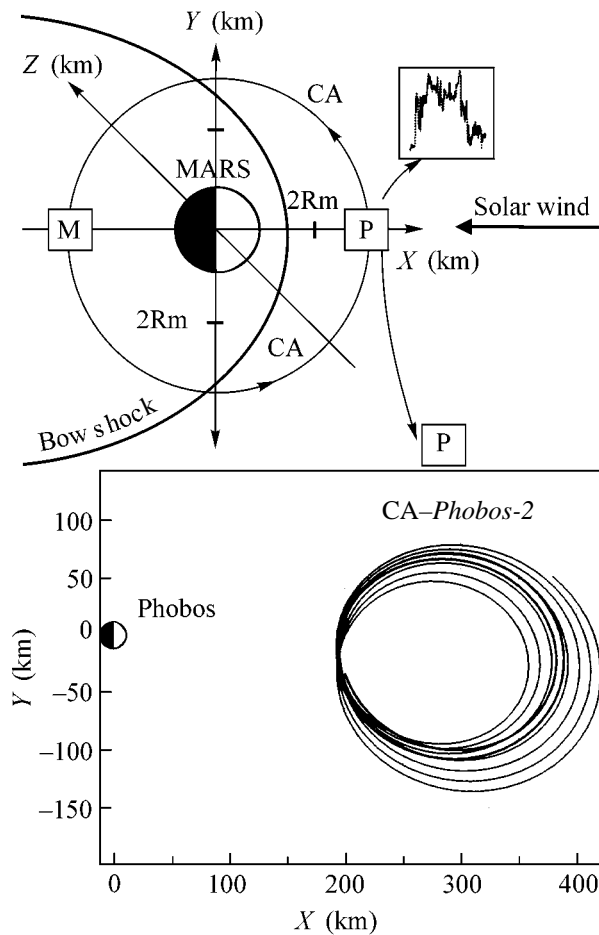[1] This article was submitted by the authors in English.

Fig. 1. Top: the spacecraft trajectory (CA) in the solar orbital coordinate system of Mars. Bottom: the spacecraft trajectory in the centric coordinate system of Phobos. The *X* axis points to the Sun.

Fig. 2. The overview of the magnetic field *B* along all "quasi-synchronous" orbits around Mars from March 22 to 26, 1989. The label P indicates the measurements near the dayside of Phobos on approaching it at 180 km.

dients of the measured magnetic field at the points of satellite trajectory. Since we are limited to the volume of a short letter, only the projection onto the plane of ecliptic will be considered. It will not affect the essence of the phenomenon.

The amplitudes and directions of the magnetic field are given in Fig. 3 in the ecliptic plane for three characteristic disturbances of the magnetic field. Recall that the *X* axis points to the Sun. Each field vector is the tangent to the magnetic force line going through the point of the trajectory at the moment when the measurement was made. The arrows indicate the location of the Phobos magnetopause. We will use the magnetic-field vector between the arrows to reconstruct the Phobos magnetosphere. In Fig. 4, a model of the Phobos magnetosphere is shown for this case.

Using Fig. 3 and the magnetograms, we will illustrate the real picture of interaction of the solar wind plasma with the Phobos magnetosphere. A simple set of pictures illustrates the dayside part of the Phobos magnetosphere. We will use the magnetic force lines. The
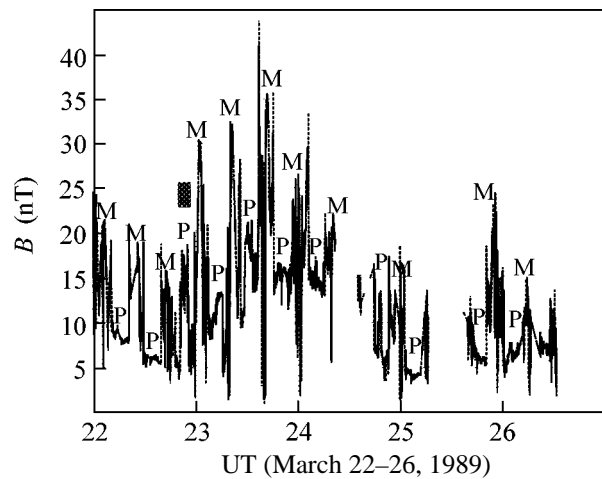
results are presented for the plane of the ecliptic in Figs. 5–7. At the top of the figures, the magnetograms of the phenomenon and the plasma parameters (the speed *V* and the plasma concentration *n*) are given. At the bottom, the magnetic phenomenon is described with the help of the magnetic force lines.

It is necessary to note that Phobos is a small body with sizes 18–21–27 km, so that the interaction picture is quite intricate. The flow direction in the subsolar point may vary very rapidly depending on the radial speed of the solar wind. And, as follows from the data presented here for the disturbance interval, the initial magnetic-field direction may strongly differ from the direction of the magnetic field of the undisturbed solar wind.

We begin the analysis with the most interesting interaction picture detected by the magnetometers at the Phobos dayside. In Fig. 5, the sharp rise in the magnetic field was observed from 20:15 to 22:00 on March 22, 1989. Except for the almost fivefold increase in the *B* value, a "shocklike" behavior is seen along the edges and in the middle of the event. The speed *V* of the solar wind increased from 400 to 600 km/s. The concentration *n* of the solar wind increased from 2 to 10 cm³ in this period. In terms of force lines, the same picture of interaction appears in clearer form. First, we see that the magnetic force lines of the solar wind are compressed by an obstacle. Then, the force lines go to Phobos, and, next, the magnetometers detect the reverse direction of the magnetic field. In addition, the loops are extended. We cannot assert that the force lines are dipole, because the appropriate analysis was not carried out. Next, the satellite again observed the solar wind plasma compressed by the obstacle.
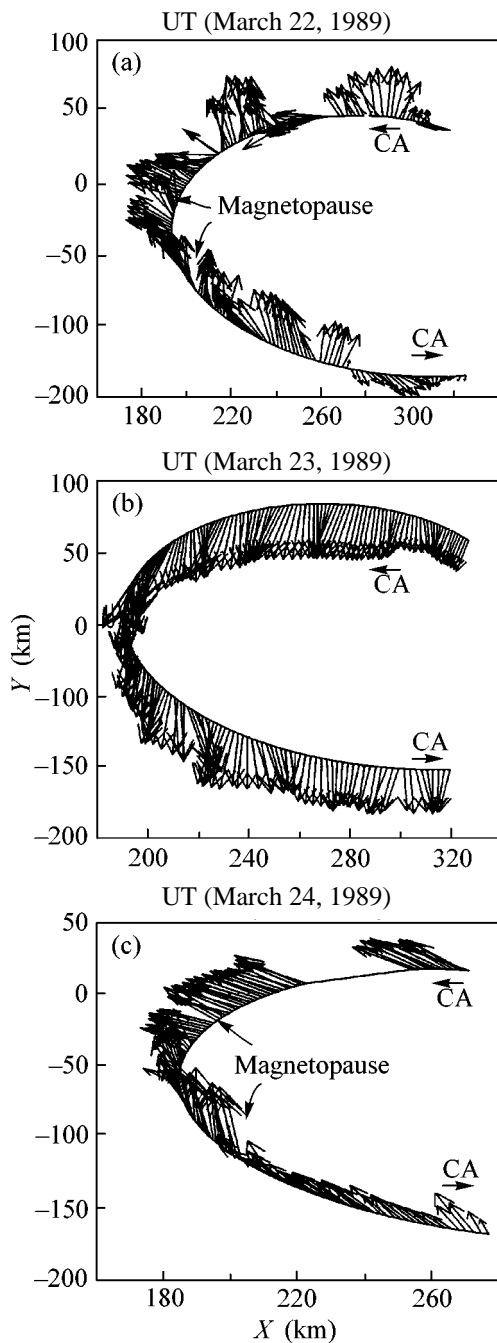
UT (March 22, 1989)

(a)

Magnetopause

CA

CA

UT (March 23, 1989)

(b)

CA

CA

Y (km)

UT (March 24, 1989)

(c)

CA

Magnetopause

CA

X (km)

Fig. 3. The amplitudes and the direction of the magnetic-field vectors (B_x/B_y) and the trajectory of the satellite (CA) in the centric coordinate system of Phobos for three characteristic disturbances at its dayside. Each vector is the tangent passing along the magnetic force line through the point of the trajectory at the moment of measurement. The data obtained at (a) 20:00–23:30 on March 22, 1989; (b) 11:00–14:00 on March 23, 1989; and (c) 18:00–20:00 on March 24, 1989.

Figure 6 shows the magnetic-field disturbance that was observed from 11:30 to 13:20 on March 23, 1989, i.e., for a rather long time—almost two hours—and, practically, at the same portion of the satellite trajec-
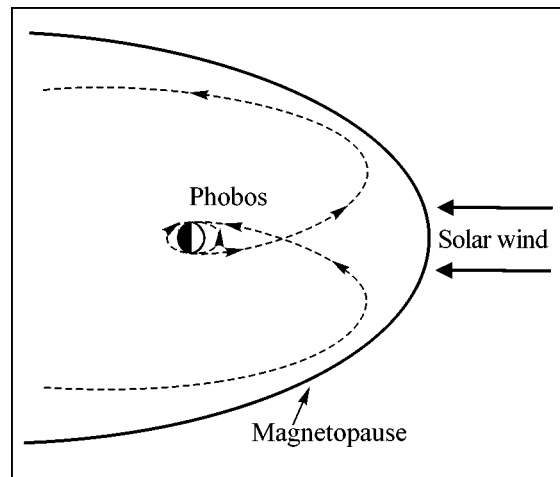

Phobos

Solar wind

Magnetopause

Fig. 4. The model of the Phobos magnetosphere, as deduced from the Phobos data.

tory. There is a well-defined feature in the behavior of the magnetic field. It does not show a "shocklike" behavior. The field increased twofold. On March 23, 1989, the dynamic pressure of the solar wind was increased to the extent that it compressed the Phobos magnetic field. The speed V of the solar wind increased from 650 to 750 km/s. The concentration n of the solar wind increased from 5 to 7 cm^{-3} in this period. Therefore, during this period, the magnetometers detected only the compressed magnetic field of the solar wind. The force line picture clearly demonstrates this. The curvature of force lines has practically a spherical type.

On March 24, 1989, the dynamic pressure of the solar wind dropped. The speed V of the solar wind decreased to 600 km/s. The concentration n of the solar wind decreased to 1 cm^{-3} in this period. Therefore, it became possible to observe a prominent event that we see in Fig. 7. This magnetogram shows a characteristic "shocklike" behavior. We will designate it by the magnetopause. Figure 7 allows the conclusion to be drawn that the satellite flew under the subsolar point of the magnetosphere. During this period, the magnetic field of the solar wind reversed its direction.

In closing the analysis, it is necessary to stress that the force lines going to Phobos and from it are observed at the same section of the trajectory. The characteristic anisotropy axis of the observations is deflected at an angle of about 15°–20° from the X axis pointed to the Sun for all events.

In conclusion, it should be noted that, in actuality, the magnetic field was measured only on the satellite trajectory, so that one can speak confidently about the direction and its value only for these points. However, near Phobos, the measured force lines always go to Phobos and then from it.
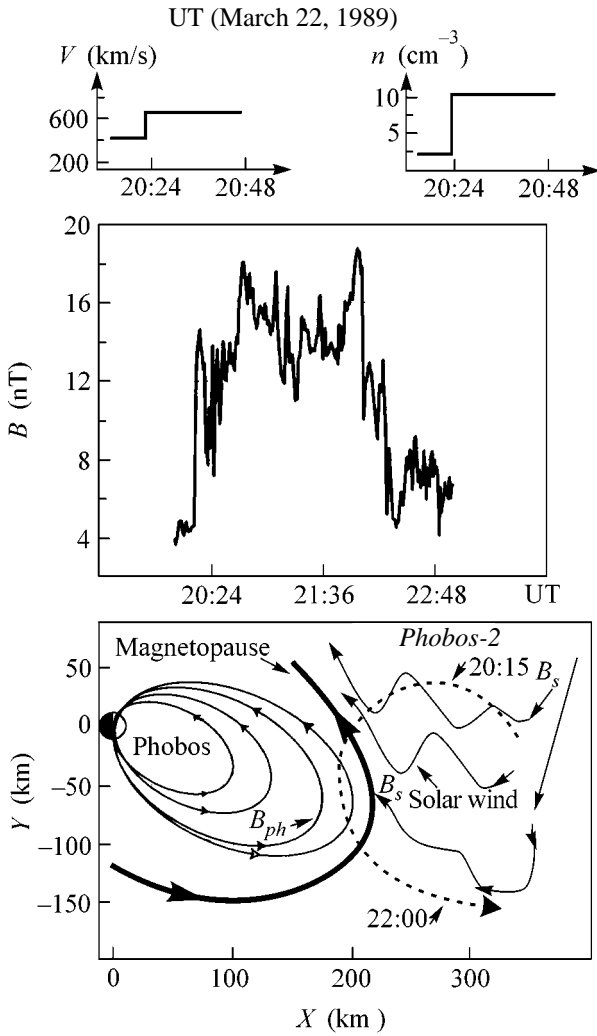
UT (March 22, 1989)

UT (March 23, 1989)

Fig. 5. Top: a sharp rise in the magnetic field B on March 22, 1989, is shown. Bottom: the magnetic phenomenon is described using the force lines of magnetic field. The gray solid lines B_s are the force lines of the magnetic field of the solar wind. The solid lines B_{ph} are the force lines of the magnetic field of Phobos. The dashed line is the trajectory of the satellite (CA) near Phobos. The dark solid line indicates the Phobos magnetopause.
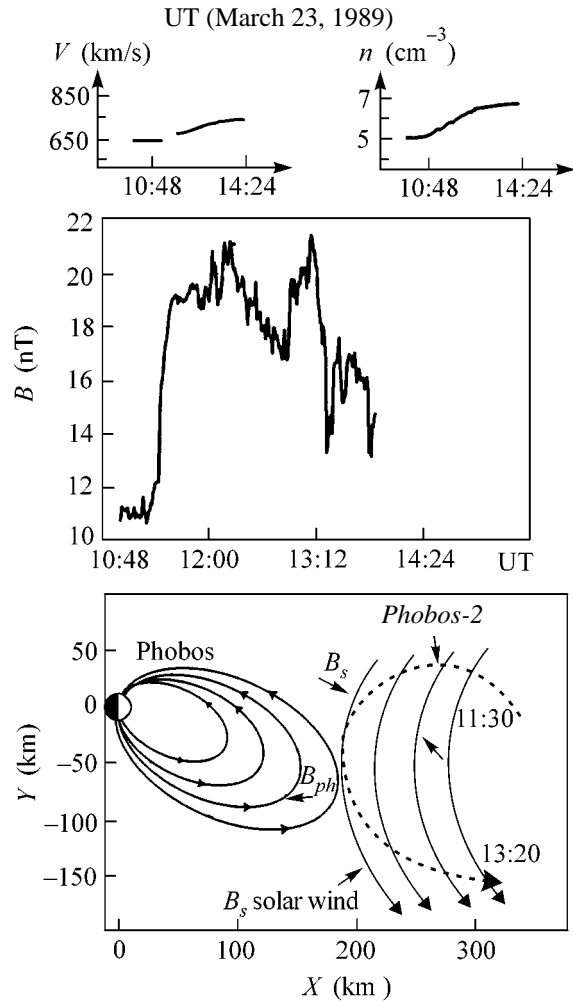
Fig. 6. The same as in Fig. 5, but the magnetic phenomenon is observed on March 23, 1989. The magnetopause is absent.

4. The magnetic field of Phobos. The existence of the Phobos magnetic field is the natural explanation for the observed magnetic disturbances near Phobos. We will make estimates of the field at its surface. Assuming the dipole character of the Phobos magnetic field H_{ph}, one can calculate its value at the Phobos surface by two independent ways from the experimental data.

First, we can calculate its value by using the measurements of the magnetic field from 18:55 to 19:40 on March 24, 1989. For the analysis of the magnetic properties of Phobos, the data are ideal. The measured magnetic field was about 13 nT (Fig. 6). $H_{ph} = 13 \times$

$(h/R_{ph})^3 = 13 \times (180/11)^3 = 0.57$ G, where R_{ph} is the Phobos radius.

Second, we can calculate the magnetic moment M' from the balance equation between the solar wind pressure and the pressure of the planet's dipole field at the magnetopause, and then the magnetic field of Phobos at its surface: $2nm_pV^2 = 1/8\pi \ (2M'/D^3)^2$, where $D = R_{ph} + h$ is the distance from the center of the planet to its subsolar point; n and V are the concentration and the speed of the solar wind, respectively; and m_p is the mass of a proton. The measured concentration and speed of the solar wind were used to estimate the magnetic moment M'. The data are $n = 0.17$ cm^{-3} and $V = 617$ km/s at 18:55–19:40 on March 24, 1989 [1]. Thus, we assume that the satellite was at the subsolar point of the Phobos magnetosphere at 19:30–19:40 on March 24, 1989, and the force line picture in Fig. 7 clearly demonstrates this. The magnetic moment is $M' = 0.8 \times 10^{18}$ G cm^3, $H_{ph} = 0.6$ G.
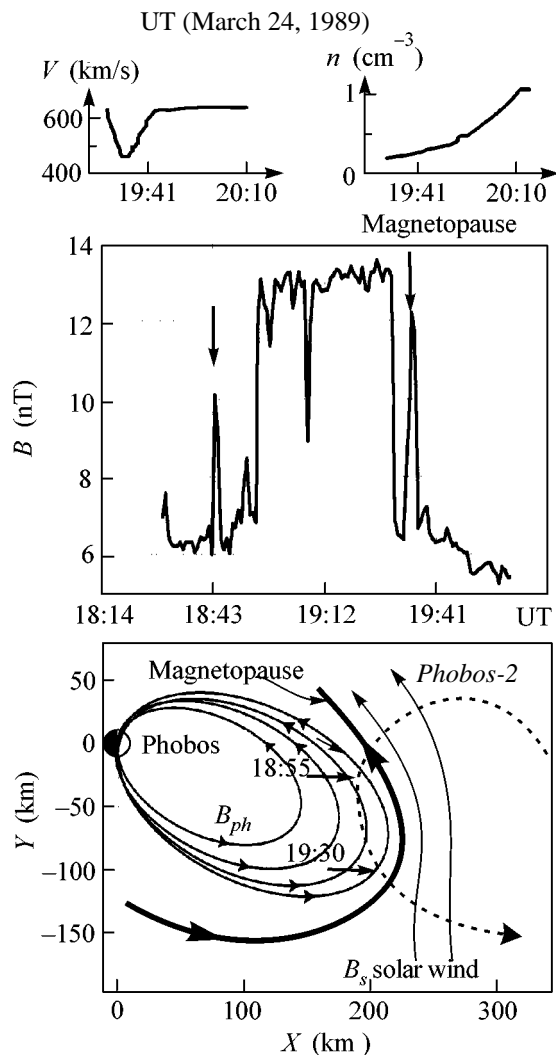
UT (March 24, 1989)

Fig. 7. The same as in Fig. 5, but the magnetic phenomenon is observed on March 24, 1989. The dark solid line shows the Phobos magnetopause.

We have arrived at the same value. The value of 0.6 G obtained for the magnetic field at the Phobos surface is mystical, because it is the same as at the Earth surface. The Earth and Phobos sizes are incommensu-

rable. The data of measurements can be used to determine the distance from Phobos to the subsolar point of its magnetosphere. It is equal to about 13–16 radii of Phobos. For the Earth, this value is about ten radii of the Earth. For Mars, this value hardly exceeds one radius of Mars.

5. In summary, let us sum up the results obtained by the magnetometers during the *Phobos-2* mission. Phobos has a magnetosphere. The distance from Phobos to the subsolar point of its magnetosphere is about 13–16 of its radii. The unusual behavior of the magnetic field observed near Phobos is explained in terms of its magnetic field. Phobos has its own magnetic field. The calculated value in the dipole approximation is equal to 0.6 G at its surface. Its steady anisotropy is observed.

At present, the origin of the magnetic field of Phobos is unknown. Since the density of Phobos is 2 g/cm^3, it seems reasonable to assume two things for the explanation. (1) Phobos is nonuniform. There exists an immense piece of a magnetic material. (2) Phobos consists of small pieces of a magnetic material in a low-density filler. The magnetization of the Phobos substance is 0.15 CGS. There are some meteorites with a magnetization of 3 CGS [5].

REFERENCES

1. E. G. Eroshenko, Kosm. Issled. **38**, 127 (2000).

2. V. G. Mordovskaya, V. N. Oraevskiĭ, and J. Rustenbach, Kosm. Issled. **39**, 477 (2001).

3. M. H. Acuna, J. E. P. Connerney, N. F. Ness, *et al.*, Science **284**, 790 (1999).

4. W. Riedler, D. Mohlmann, V. N. Oraevsky, *et al.*, Nature **341**, 604 (1989).

5. E. G. Gus'kova, *Magnetic Properties of Meteorites* (Nauka, Moscow, 1972).

Efficiency of Electron–Positron Pair Production by Neutrino Flux from Accretion Disk of a Kerr Black Hole

A. A. Gvozdev* and I. S. Ognev**

Yaroslavl State University, ul. Sovetskaya 14, Yaroslavl, 150000 Russia
* e-mail: gvozdev@uniyar.ac.ru
** e-mail: ognev@uniyar.ac.ru
Received July 18, 2001; in final form, August 21, 2001

Dominant processes of neutrino production and neutrino-induced e^+e^--pair production are examined in the model of a disk hyperaccreting onto a Kerr black hole. The efficiency of plasma production is analytically estimated for both the presence and the absence of a strong magnetic field. It is shown that the efficiency of plasma production by a neutrino flux from the disk in this model is no more than several tenths of percent and, therefore, cannot account for the origin of cosmological gamma-ray bursts. © *2001 MAIK "Nauka/Interperiodica".*

PACS numbers: 97.60.Lf; 13.15.+g; 95.30.Cq; 97.10.Gz; 98.70.Rz

The problem of the gamma-ray burst origin is among the most important problems of modern astrophysics. Various observations agree well with the phenomenological model implying that gamma-ray bursts are produced by an ultrarelativistic e^+e^- plasma jet (fireball) [1]. Observations indicated that gamma-ray bursts rapidly vary and some of these bursts arrive from cosmological distances. This suggests that a fireball is produced in a compact region and has a vast energy of $\mathcal{E} \gtrsim 10^{51}$ erg [2]. Neutrinos could be one of the natural sources of such a fireball. Indeed, neutrino radiation can carry away up to ten percent of the gravitational energy released in a collapse in compact systems. Because of small weak-interaction cross sections, only several percent of this energy is transferred to the e^+e^- plasma, but this amount can be enough to produce a typical fireball with an energy of $\mathcal{E} \sim 10^{51}$ erg. However, the produced plasma can escape and remain ultrarelativistic (which is necessary for its subsequent transformation into an observed gamma-ray burst) only from a region with sufficiently low baryon density [3].

These conditions can exist in systems involving an accretion disk around a Kerr black hole, e.g., unrealized supernova [4], collapsar with hyperaccretion [5], and hypernova [6]. Because of a high accretion rate and viscosity, the density and temperature in the inner part of the disk can attain values ($\rho \sim 10^{10}$–10^{11} g/cm³ and $T \sim$ 5–10 MeV) for which neutrino luminosity reaches $L_\nu \sim 10^{53}$ erg/s. At the same time, a region of low baryon density can be formed near the rotation axis [4, 5]. Thus, a large neutrino flux from the disk generates a plasma which can escape with an energy sufficient for producing a gamma-ray burst.

It is important that strong magnetic fields can arise in the accretion disk. The field strength in the viscous disk with densities of interest can attain the values [7]

$$B \lesssim 10^{15}\ \text{G} \left(\frac{\alpha}{0.1}\right)^{1/2}\left(\frac{c_s}{10^9\ \text{cm/s}}\right)\left(\frac{\rho}{10^{11}\ \text{g/cm}^3}\right)^{1/2}, \quad (1)$$

where α is the dimensionless viscosity parameter and c_s is the speed of sound. This magnetic field has a complex structure. However, only its strength is important for the elementary processes under consideration.

It is believed that a neutrino flux in a rarefied medium produces plasma primarily through the process

$$(\nu_i + \tilde{\nu}_i) \longrightarrow e^+ + e^- \quad (i = e, \mu, \tau), \quad (2)$$

which has long been studied. In early studies, the effect of this process on the explosion dynamics of a type-II supernova was examined through calculating its luminosity in e^+e^- pairs using the simplest models of neutrino blackbody emission to vacuum [8] and, later, with inclusion of the neutrino flux passage through the partially transparent shell medium [9]. As the evidence for the cosmological origin of a gamma-ray burst was accumulated, process (2) began to be treated as a possible energy source of a fireball [10]. However, the detailed numerical calculations of the fireball production were performed only in recent papers [4, 5, 11], where the magnetic-field effects on plasma production in the neutrino reactions were ignored. However, these effects can be substantial in a strong field. Indeed, the new reactions

$$\nu_i \longrightarrow \nu_i + e^+ + e^-, \quad (3)$$

$$\tilde{\nu}_i \longrightarrow \tilde{\nu}_i + e^+ + e^- \quad (4)$$

of e^+e^--pair production are not excluded kinematically in this case and, moreover, can dominate. Gvozdev *et al.* [12] were, probably, the first to point out the importance of this process as a possible energy source of a cosmological gamma-ray burst.

In this paper, the efficiency of e^+e^--plasma production in the processes involving neutrinos is estimated using the model of a disk hyperaccreting onto a Kerr black hole. The efficiency is defined as the ratio of the e^+e^--pair luminosity $L_{e^+e^-}$ (energy emitted per unit time) to the neutrino luminosity $L_\nu + L_{\tilde\nu}$ from the disk:

$$\epsilon = L_{e^+e^-}/L_{tot}, \quad L_{tot} = L_\nu + L_{\tilde\nu}. \tag{5}$$

This paper focuses on deriving analytical expressions for the efficiency of plasma production in the dominant neutrino processes using a simplified model of accretion disk with inclusion of a strong magnetic field. Of course, the efficiency will only be estimated, but this approach clearly demonstrates the e^+e^--pair luminosity as a function of the basic parameters of the system.

We neglect general relativity effects on plasma production. As is well known, the gravitational field has two effects: the neutrino redshift reduces the e^+e^--pair luminosity, whereas the bending of neutrino trajectories increases it due to an increase in the collision frequency. An analysis of these effects indicates that the bending effect dominates only at sufficiently large radii of the Kepler orbit ($R_0 \gtrsim 3r_g$, where r_g is the gravitational radius of a black hole) [13]. However, the efficiency even in this case increases by no more than a factor of 2.

As was mentioned above, to ensure the required neutrino luminosities, the inner part of the disk should have high densities and temperatures. Such parameters can be attained in hyperaccretion onto a Kerr black hole [5]. Leaving aside the stability problem for a system with such accretion rates, we determine the disk parameters by using the results obtained in [5], where the resulting density and temperature gradients suggest that the neutrino-emitting part of the disk is uniform. At an accretion rate of $\dot M \sim 0.1 M_\odot/s$, the typical densities and temperatures are $\rho \sim 10^{11}$ g/cm^3 and $T \sim 5$ MeV, respectively. For these parameters, neutrinos are predominantly emitted from the Urca processes

$$p + e^- \longrightarrow n + \nu_e, \tag{6}$$

$$n + e^+ \longrightarrow p + \tilde\nu_e. \tag{7}$$
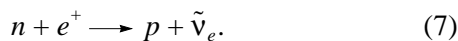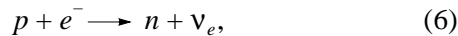
An analysis indicates that a magnetic field of $B \sim 10^{15}$ G has a negligible effect on the cross sections for these reactions. The neutrino mean free path in such a medium is estimated as

$$l_\nu \sim 10 \text{ km} \left(\frac{10^{11} \text{ g/cm}^3}{\rho}\right)\left(\frac{5 \text{ MeV}}{T}\right)^2. \tag{8}$$

Thus, the disk part under consideration can be treated as transparent to neutrinos. Note that the typical times of establishing the β equilibrium in Urca processes (6) and (7) are $\tau_\beta \sim 10^{-2}$ s for the medium parameters used. The characteristic dynamical accretion time can roughly be estimated as the time it takes for a nucleon flux to pass through the neutrino-emitting disk part and is also about $\tau_d \sim 10^{-2}$ s. Thus, the accreting matter does not arrive at the β equilibrium, and, therefore, the parameter $Y = N_p/(N_p + N_n)$ is indeterminate and can vary in the interval

$$Y_\beta < Y < 0.5, \tag{9}$$

where N_p and N_n are the proton and neutron densities in the disk and Y_β is the Y parameter at β equilibrium ($Y_\beta \sim 0.1$ for the densities and temperatures under consideration).

Because the neutrino mean free path exceeds the characteristic transverse dimension of the disk, neutrinos are freely streaming through the disk. In this case, the neutrino luminosity is calculated in the standard way by using the Lagrangian for the interaction of charged electron–neutrino and nucleon currents in the low-energy approximation [14] and can be represented as

$$L_{\nu, \tilde\nu} = \int \omega F_{\nu, \tilde\nu} d^3n, \tag{10}$$

$$F_{\nu, \tilde\nu} = \frac{G_F^2 \cos^2\theta_c(1 + 3g_a^2)}{\pi} \frac{\omega^2 N_{p,n}}{\exp[\omega/T \mp a] + 1}. \tag{11}$$

Here, ω is the neutrino energy; d^3n is the neutrino phase-space element; T is the temperature of the medium; $a = (\mu - m_n + m_p)/T$, where μ is the electron chemical potential and m_n and m_p are the neutron and proton masses, respectively; N_n and N_p are the neutron and proton densities, respectively; g_a is the axial constant of the charged nucleon current ($g_a \simeq 1.26$ in the low-energy limit); G_F is the Fermi constant; and θ_c is the Cabibbo angle. Integral (10) can easily be calculated for the simplified model of a uniform disk. As a result, the (anti)neutrino luminosity in the Urca processes from the disk is written as

$$L_{\nu, \tilde\nu} = \frac{(G_F \cos\theta_c)^2}{2\pi^3}(1 + 3g_a^2)N_{p,n}T^6 V I_5(\pm a),$$

$$\tag{12}$$

$$I_s(a) = \int_0^\infty \frac{y^s dy}{\exp(y - a) + 1},$$

where V is the emitting disk volume. The ratio of the neutrino luminosity in the Y interval (9) is $L_{\tilde\nu}/L_\nu \ll 1$. As is seen in the figure, even in the most favorable case of β equilibrium, this ratio is about one-tenth and decreases very rapidly as Y increases. Thus, we set $L_{tot} \simeq L_\nu$ in all cases unless this will lead to confusion.
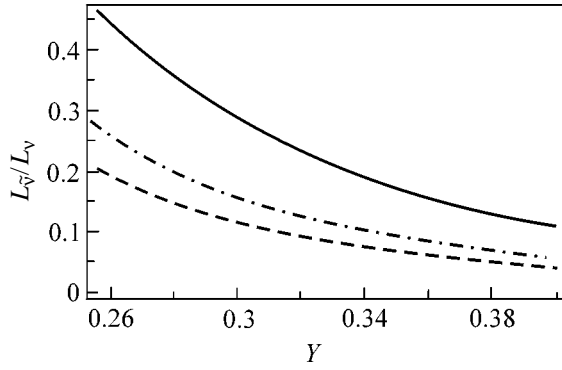
The ratio of neutrino luminosities $L_{\tilde{\nu}}/L_\nu$ vs. the parameter Y for (solid line) $\rho = 10^{11}$ g/cm³, $T = 7$ MeV, and $Y_\beta = 0.30$; (dash–dotted line) $\rho = 5 \times 10^{10}$ g/cm³, $T = 5$ MeV, and $Y_\beta = 0.26$; and (dashed line) $\rho = 10^{11}$ g/cm³, $T = 6$ MeV, and $Y_\beta = 0.24$.

We calculate the e^+e^--pair luminosity for the case where the magnetic field is sufficiently strong but the parameter eB is much less than the neutrino characteristic energy squared:

$$m_e^2 \ll eB \ll \omega^2, \tag{13}$$

which is satisfied well in the case under consideration. Here, m_e is the electron mass and $e > 0$ is the elementary charge. As was argued above, it is most important to estimate the plasma production efficiency within a small solid angle around the system rotation axis. Because the medium in this cone is rarified, its effect on the processes can be neglected. The magnetic field can have a complex structure in this region, but we treat its field lines as directed along the rotation axis.

The electron–positron-pair emissivity per a unit volume in reaction (2) is determined by

$$Q_{\nu\tilde{\nu} \to e^+e^-} = \int j\sigma q_0 dN_\nu dN_{\tilde{\nu}},$$
$$dN_{\nu,\tilde{\nu}} = \frac{\omega^2 F_{\nu,\tilde{\nu}}}{8\pi^3 R^2} dV d\omega, \tag{14}$$

where σ is the cross section for the process, $j = q^2/2\omega_1\omega_2$ is the relative velocity in the rest frame of one of the colliding particles, $dN_{\nu,\tilde{\nu}}$ is the (anti)neutrino density at a distance R from the element dV of the isotropically emitting disk, and $q = q_1 + q_2$ is the 4-momentum transfer in the reaction. An analysis shows that the magnetic field only slightly affects the cross section in the approximation (13):

$$\sigma = \sigma_0\left(1 + O\left(\frac{eB}{\omega^2}\right)\right), \quad \sigma_0 = \frac{G_F^2}{3\pi}(c_v^2 + c_a^2)q^2, \tag{15}$$

where σ_0 is the cross section for the process in vacuum; $c_v = 1/2 + 2\sin^2\theta_W \simeq 0.96$ and $c_a = 1/2$ are, respectively,

the vector and axial constants of the charged neutrino–electron current; and θ_W is the Weinberg angle $(\sin^2\theta_W \simeq 0.23)$. Therefore, the luminosity in the reaction under study can be estimated in the vacuum approximation. By integrating Eq. (14) over the volume of a cone with a solid angle of $\Delta\Omega \ll 4\pi$ along the black-hole rotation axis, we obtain the formula for the e^+e^--pair luminosity. It is reasonable to relate this expression to the neutrino–antineutrino luminosity from the inner part of the disk:

$$L_{\nu\tilde{\nu} \to e^+e^-} = \frac{G_F^2(c_v^2 + c_a^2)}{128\pi} L_\nu L_{\tilde{\nu}} \frac{T}{R_0}\left(\frac{\Delta\Omega}{4\pi}\right)$$
$$\times \left[\frac{I_6(a)}{I_5(a)} + \frac{I_6(-a)}{I_5(-a)}\right], \tag{16}$$

where R_0 is the radius of the last Kepler orbit.

The luminosity for processes (3) and (4) can be calculated by using the expression obtained in [15] for the rate of energy transfer to e^+e^- plasma per one neutrino. In approximation (13), this expression can be represented with logarithmic accuracy as

$$\dot{E} = \frac{7G_F^2(c_v^2 + c_a^2)}{432\pi^3}(eB\omega\sin\theta)^2 \ln[eB\omega\sin\theta/m_e^3], \tag{17}$$

where θ is the angle between the initial neutrino momentum and the magnetic field. By integrating this formula over neutrino distribution dN_ν (14) and cone volume, we obtain the total luminosity from the disk for the e^+e^- plasma produced in process (3):

$$L_{\nu \to \nu e^+e^-} = \frac{7G_F^2(c_v^2 + c_a^2)}{1728\pi^2}L_\nu(eB)^2 TR_0$$
$$\times\left(\frac{\Delta\Omega}{4\pi}\right)\frac{I_6(a)}{I_5(a)}\ln[eBT/m_e^3]. \tag{18}$$

The antineutrino luminosity in process (4) is determined by the same formula with replacement

$$L_\nu \longrightarrow L_{\tilde{\nu}}, \quad a \longrightarrow -a. \tag{19}$$

Because the ratio $L_{\tilde{\nu}}/L_\nu$ is small (see figure), antineutrino reaction (4) makes a small contribution to the total plasma luminosity.

Can new reactions (3) and (4) be competitive with basic process (2) of plasma production? The luminosity ratio for these processes can be written as

$$\frac{L_{\nu \to \nu e^+e^-}}{L_{\nu\tilde{\nu} \to e^+e^-}} = \eta\left(\frac{eB}{T^2}\right)^2\left(\frac{l_{\tilde{\nu}}}{R_0}\right), \tag{20}$$

where η is a dimensionless constant on the order of unity. Therefore, both processes can make comparable contributions to the e^+e^--pair luminosity for the disk parameters used. However, the new processes become

efficient only if magnetic fields (1) attain their maximum strengths in the disk–black hole system.

The efficiency of plasma production in process (2) is numerically estimated as

$$\epsilon_{\nu\tilde{\nu} \to e^+e^-} \simeq 10^{-2}\frac{L_{\tilde{\nu}}}{L_{\nu}}\left(\frac{\Delta\Omega}{4\pi}\right)\left(\frac{L_{\text{tot}}}{10^{53}\text{ erg}}\right)$$
$$\times\left(\frac{T}{5\text{ MeV}}\right)\left(\frac{R_0}{30\text{ km}}\right)^{-1}. \qquad (21)$$

This expression depends strongly on the chemical composition of the medium through the ratio $L_{\tilde{\nu}}/L_{\nu}$ (see figure) and decreases rapidly from its maximum value as the disk medium deviates from the β equilibrium. Thus, the efficiency of plasma production in the absence of a magnetic field does not exceed several tenths of percent and becomes negligible at a sizable deviation of the disk nucleon medium from β equilibrium.

A similar estimate for process (3) yields

$$\epsilon_{\nu \to \nu e^+e^-} \simeq 2\times 10^{-3}\left(\frac{\Delta\Omega}{4\pi}\right)\left(\frac{B}{4\times 10^{15}\text{ Gs}}\right)^2$$
$$\times\left(\frac{T}{5\text{ MeV}}\right)\left(\frac{R_0}{30\text{ km}}\right). \qquad (22)$$

It is easy to see that the efficiency in this process is independent of the disk chemical composition. This implies that the plasma production by a single neutrino in a strong magnetic field may prevail over the annihilation if there is a deviation from the β equilibrium. However, even in this case, the efficiency of plasma production does not exceed several tenths of percent and decreases quadratically as the magnetic field decreases. Thus, the neutrino mechanism of plasma production in collapsing systems with hyperaccretion is likely to be inefficient. Ruffert and Janka [11] arrived at a similar conclusion for the model of a close binary system coalescing into a black hole.

REFERENCES

1. N. J. Shaviv and A. Dar, Astrophys. J. **447**, 863 (1995); A. Dar, Astrophys. J. Lett. **500**, L93 (1998).

2. K. A. Postnov, Usp. Fiz. Nauk **169**, 545 (1999).

3. M. J. Rees and P. Meszaros, Mon. Not. R. Astron. Soc. **258**, 41 (1992); P. Meszaros and M. J. Rees, Astrophys. J. **405**, 278 (1993).

4. S. E. Woosley, Astrophys. J. **405**, 273 (1993); A. Mac Fadyen and S. E. Woosley, Astrophys. J. **524**, 262 (1999).

5. R. Popham, S. E. Woosley, and C. Fryer, Astrophys. J. **518**, 356 (1999).

6. B. Paczynski, Astrophys. J. Lett. **494**, L45 (1998).

7. N. I. Shakura and R. A. Syunyaev, Astron. Astrophys. **24**, 337 (1973); G. S. Bisnovatyi-Kogan and A. A. Ruzmaikin, Astron. Space Sci. **42**, 401 (1976); G. S. Bisnovatyi-Kogan, Astron. Astrophys. **274**, 796 (1993).

8. V. S. Berezinsky and O. F. Prilutsky, Astron. Astrophys. **175**, 309 (1987); J. Cooperstein, L. J. van den Horn, and E. Baron, Astrophys. J. Lett. **321**, L129 (1987).

9. H.-Th. Janka, Astron. Astrophys. **244**, 378 (1991).

10. B. Paczynski, Astrophys. J. **363**, 218 (1990); A. Dar, B. Z. Kozlovsky, S. Nussinov, and R. Ramati, Astrophys. J. **388**, 164 (1992); P. Meszaros and M. J. Rees, Mon. Not. R. Astron. Soc. **257**, 29 (1992).

11. M. Ruffert and H.-Th. Janka, Astron. Astrophys. **338**, 535 (1998); **344**, 573 (1999).

12. A. A. Gvozdev, A. V. Kuznetsov, N. V. Mikheev, and L. A. Vasilevskaya, Yad. Fiz. **61**, 1125 (1998) [Phys. At. Nucl. **61**, 1031 (1998)].

13. K. Asano and T. Fukuyama, astro-ph/0009453 (2000).

14. G. G. Raffelt, *Stars as Laboratories for Fundamental Physics* (Univ. of Chicago Press, Chicago, 1996).

15. A. V. Kuznetsov and N. V. Mikheev, Yad. Fiz. **60**, 2038 (1997) [Phys. At. Nucl. **60**, 1865 (1997)].

Translated by R. Tyapaev

Experimental Studies of Very Cold Neutrons Passing Through Solid Deuterium[1]

**A. P. Serebrov, E. A. Kolomenski, M. S. Lasakov, V. A. Mityukhlyaev, A. N. Pirozhkov,
I. A. Potapov, V. E. Varlamov, A. V. Vasiliev, A. R. Young[1], and A. A. Zakharov**

Institute of Nuclear Physics, Russian Academy of Sciences, Gatchina, St. Petersburg, 188300 Russia
[1] Princeton University, Princeton, NJ 08544, USA
Received August 16, 2001

The studies of spectral dependences for neutrons passing through solid deuterium were carried out using a vertical beam of very cold neutrons with the wavelength $\lambda \sim 40$–150 Å. The results show the dependence of the observed neutron scattering cross sections on the method of preparation of a solid deuterium sample and on the ortho–para composition of deuterium. © *2001 MAIK "Nauka/Interperiodica".*

PACS numbers: 28.20.Cz

1. Introduction. The ability of ultracold neutrons (UCN) to be stored in material and magnetic traps makes them an effective tool in experimental low-energy physics. A search for the static electric dipole moment (EDM) of the neutron and measurements of the free-neutron lifetime and neutron β-decay angular-correlation constants are the most significant experiments in this field. At present, the most accurate value of neutron lifetime [1] and the limits for the value of neutron EDM [2, 3] have been obtained using UCN. The scientific impact of these measurements of neutron properties is sweeping. For example, the existence of a nonzero neutron EDM would mean the violation of the fundamental CP symmetry in particle physics. Violation of this symmetry is manifested by the observed asymmetry between matter and antimatter in the universe. In fact, the matter/antimatter asymmetry is believed to be inconsistent with the standard model of particle physics, a belief which has triggered a proliferation of proposed extensions to the standard model and incorporation of new phenomenology such as supersymmetry. One- or two-orders-of-magnitude increase in the sensitivity of neutron EDM measurements might serve as a decisive test for many of these proposed models.

However, methodical improvements of these neutron experiments, without a substantial (by orders of magnitude) increase in the intensity of UCN sources, cannot increase accuracy to a desired level. The first practical step in achieving increased UCN intensities using a solid deuterium (SD$_2$) UCN source at liquid helium temperature was accomplished at PNPI, Gatchina, Russia [4–6]. The advantages of SD$_2$ can be used best under conditions of heat loads that are somewhat smaller than for the conventional reactor cold sources; in this connection, a pulsed mode with a spallation neutron source was proposed [7]. At present, work on the creation of new high-intensity SD$_2$ UCN sources is being carried out at several international scientific centers: LANL (USA), PSI (Switzerland), and TUM (Germany). For source calculations and UCN yield evaluations, theoretical values of cross sections for the interaction of very cold neutrons (VCN) and UCN with SD$_2$ were used. More recently, detailed calculations of the incoherent inelastic scattering processes and measurements of the UCN lifetime and production in SD$_2$ as functions of paradeuterium concentration and temperature were performed at LANL [8, 9]. However, no direct experimental cross-section data in this neutron energy range are available to date.

This work is an attempt to study experimentally the passage of very cold neutrons through SD$_2$. The apparatus described in detail in [10] was used as a solid deuterium target. The spectral dependence for neutrons passing through the target was studied by the time-of-flight technique.

2. Experimental setup. The experimental scheme is presented in Fig. 1. A bent vacuum-processed mirror neutron guide (2) was installed at the exit of the horizontal neutron guide (1), which was connected to the SD$_2$ cold neutron source of the PNPI WWR-M reactor [5]. The bent neutron guide served to form a vertical VCN beam. It was made of a sheet polished stainless steel; the neutron-guide cross section was 60×140 mm^2, and its bending radius was 1 m. The neutron-guide output window was made from aluminum and was 0.5 mm thick. The cadmium mask (4) with a 14×140 mm^2 slot was installed ahead of the output window inside the neutron-guide vacuum jacket. The mask slot was

---

[1] This article was submitted by the authors in English.

placed closer to the outer (larger radius) wall of the curved neutron guide and served to cut off a part of the neutron beam, which ran mainly along this wall. The shield (3) provided for the absorption of the direct beam from the horizontal channel and ensured satisfactory background conditions for the scattering measurements.

The neutron beam chopper (9) was placed over the neutron guide. The chopper itself was a flat disc with a radial slot, which was made from a neutron-absorbing material. The chopper rotation frequency was $1500~min^{-1}$. A detector (5), which monitored the neutron flux incident on the target, was placed between the chopper and the neutron guide. It blocked a part of the neutron-guide output cross section and provided a method of controlling the intensity of the initial neutron beam.

The target and cryostat (6) was located over the chopper. The input and output windows of the cryostat vacuum jacket and the target internal vessel (10) with the sample studied were made of zirconium and were 0.2 mm thick. The primary neutron counter (11) was placed over the cryostat output window. Proportional ^3He counters served as neutron detectors. The distance between the chopper (9) and the detector (11) was 50 cm.

Deuterium with $D_2 = 99.79\%$ was used in this work; the primary contaminants were HD and H_2, and the percentages of N_2 and O_2 were less than 2×10^{-2}. Deuterium was confined in an internal zirconium vessel (10) equipped with a heat exchanger. The target was cooled by helium flowing from the liquid-He reservoir (8). It was possible to have both liquid and solid deuterium in the hydrogen vessel, thanks to the cold gaseous-helium consumption control through the target heat exchanger. The SD_2 layer thickness was determined by the volume of gas condensed in the target, with account taken of the volume of displacers (heat exchanger and lithium-6 shield).

Neutrons scattered in the target were captured by a 2-mm-thick protective shield made from metallic ^6Li. This shield was placed in the internal vessel of the cryostat and formed the operating volume of the target with a cross section of $104 \times 40~mm^2$ and a height of 196 mm. As a result, the heat exchanger and the side walls of the zirconium vessel were not irradiated with the scattered neutrons. The high lithium heat conductivity provided a good leveling off of the temperature along the entire target volume.

The time-of-flight neutron spectra were measured without the target and with an empty target. They showed that the beam of neutrons, which were distributed along the external wall of the neutron guide and reached the main detector, was characterized by wavelengths of 40–150 Å with a maximum in the 60–65 Å interval. This corresponds to the energy range $E_n = (0.4–5) \times 10^{-5}$ eV. An example of such spectrum is pre-
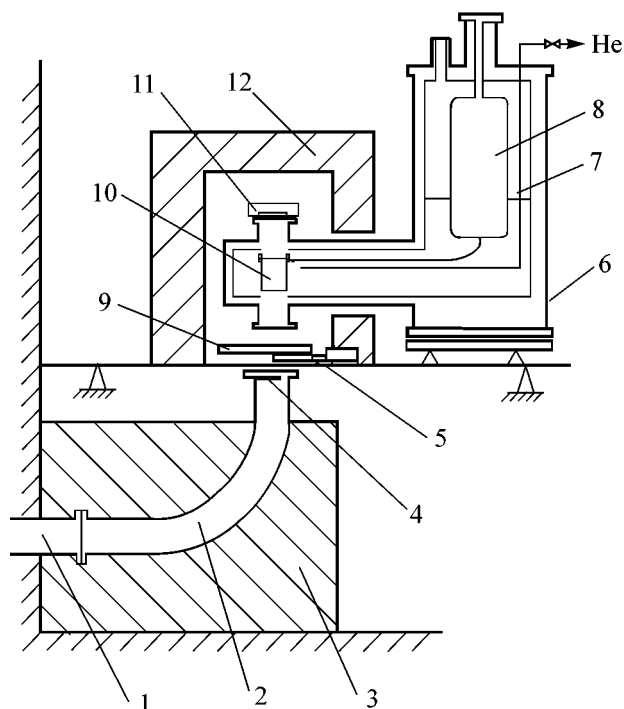

Fig. 1. Experimental setup: (1) horizontal neutron guide; (2) bent mirror neutron guide; (3) combined protection; (4) cadmium mask; (5) monitor detector; (6) target and cryostat; (7) liquid nitrogen tank; (8) helium tank; (9) neutron-beam chopper; (10) deuterium vessel; (11) main neutron detector; (12) polyethylene shield.

sented in the figures. Neutrons with a wavelength of less than 35–40 Å were incapable of passing through the neutron guide with the bending radius used in our system. There were practically no neutrons with $\lambda \sim$ 150 Å (close to ultracold neutrons and UCNs themselves) in the recorded spectrum, because of, first, their very large angular scatter at the end of the neutron guide and, second, a high probability of them being captured in the air and in the materials of the neutron guide and target "windows."

3. Orthodeuterium and its preparation. Molecular deuterium can be divided into two states on the basis of their rotational spectra. These states differ in the relative orientation of spins of the deuteron nuclei forming the molecule. If the total nuclear spin of the molecule is denoted by $\mathbf{S}$, then these two states are orthodeuterium ($\mathbf{S} = 0, 2$) and paradeuterium ($\mathbf{S} = \mathbf{1}$). The total wave function of the molecule is symmetric. This means that orthodeuterium can only have rotation states with even $\mathbf{J}$, whereas paradeuterium can only have rotation states with odd $\mathbf{J}$. The molecular vibrational states are not excited under normal conditions.

The ground-state energy of the orthodeuterium rotational band is 7 meV lower than that of the paradeuterium molecule. At a given temperature, the equilibrium ortho–para composition is determined by the ratio of

level populations for the even and odd rotational states. At room temperature, the ortho–para concentration ratio is 2/1, and such deuterium is called "normal." At low temperatures, it is possible to obtain a higher concentration of orthodeuterium. For instance, at a temperature of 20 K, the equilibrium concentration C_{ortho} is ~98%. Spontaneous transition to the equilibrium concentration is a very slow process; however, relaxation to the equilibrium state can be accelerated by paramagnetic catalysts.

A finely dispersed $Fe(OH)_3$ powder was used as a catalyst in our work. Deuterium targets with different orthophase concentration were obtained by passing gas through a cooled container with the catalyst. The container with iron hydroxide was either placed in a bath with liquid nitrogen or cooled by cold helium to temperatures of about 20–25 K in a conversion apparatus [10]. The reverse conversion without a catalyst runs very slowly; therefore, after conversion, gaseous deuterium was transported into the target through "warm" supplying lines and then was condensed and frozen there. Analysis of the deuterium ortho–para concentration was carried out using a gas chromatograph LCM-8MD. The measured gaseous samples were taken directly from the target.

4. Measurement procedure and results. The measurements were carried out in the following way. First, after cooling the cryostat, neutron spectra with the empty target were measured. The total counting rate in the primary neutron detector for the empty target was ~70 n/s. Neutron spectra were accumulated in a series of 500-s runs. These runs were then summed in the analysis, with account taken of the monitor detector readings. Adequate statistics were typically obtained after several hours of operation in this mode. The target was then filled with a certain volume of deuterium without removing the cryostat from the beam and without disturbing the positioning of the apparatus. The condensation time of $V = 232$ normal liters of gaseous D_2 into liquid deuterium took roughly two hours. This gas volume corresponds to approximately 3 cm of SD_2 along the beam axis. In different experiments, we had the 3-cm and 6-cm SD_2 layers. The main uncertainty in the pathlength is associated with the error of calculations of the volume of displacers immersed into deuterium. It is equal to about 5%.

Further sample cooling could be accomplished at different rates by regulating the cold helium flow through the target heat exchanger. The first cooling from the deuterium triple point (18.7 K) to temperatures below 6 K took approximately an hour. The subsequent neutron spectra were measured over a time interval of several hours. The deuterium state was controlled by regulating the vapor pressure over the liquid or solid deuterium. Additional temperature sensors (carbon Allen–Bradley resistors) were installed on the jacket of the deuterium vessel.

Then deuterium in the target was heated and fully melted at the temperature $T \sim 19$ K and subsequently was frozen again to the temperature $T < 6$ K. The second freezing was carried out slower than the first one—over an interval of about two hours. The neutron spectra were measured anew.

In all measurements, the intensity of the initial neutron beam was recorded in the monitoring detector. This permitted us to normalize the neutron flux variations caused by changes in the reactor power and in the cold neutron source temperature.

The normalized time-of-flight spectra for neutrons transmitted through the SD_2 samples and the empty target were used to calculate the spectral dependence of the cross section for neutron interaction with SD_2. Since the VCN capture cross section by deuterium is small, the changes in the transmitted neutron flux are due to the scattering processes. The neutron background was taken into account in the cross-section calculations. It was determined from the counts in the first and the last channels of the time base and was found to be equal, on average, to 0.8 n/s, when integrated over the entire spectrum.

The total cross sections for neutron interactions with the SD_2 sample studied were calculated using the formula

$$\sigma(\lambda) = \frac{\ln[N_0(\lambda)/N_L(\lambda)]}{nL}, \qquad (1)$$

where N_0 and N_L denote the total numbers of counted neutrons for the empty target and the target with SD_2, respectively; n is the number of deuterium molecules in 1 cm^3; and L is the sample length along the neutron beam. The errors presented in the figures correspond to the statistical uncertainty of calculating only σ.

The experiments were performed with the deuterium having various ortho–para compositions: 66%, 72%, and 93% of orthophase. The "transparency" of the deuterium target was found to depend on the freezing rate. For example, Fig. 2 depicts the cross-section curves for the deuterium with orthophase concentration of (93 ± 3)%. With our construction of the cooled target volume, the best neutron transmission was obtained for a freezing time of about two hours for all samples. The neutron cross sections $\sigma(\lambda)$ are congruent in the short-wavelength portion of the spectrum, but they differ from each other for large λ. The observed difference can only be explained by the difference in the sample structures obtained by the different procedures of manufacturing SD_2. It is associated, apparently, with the "ice" quality: the scatter of crystal sizes, density heterogeneities in the sample volume, cracks, etc. Because the neutron wavelength sets a rough upper limit on the size scale over which the neutron transport is sensitive to the structural variations, it also seems reasonable that the sample macrostructure should have the strongest
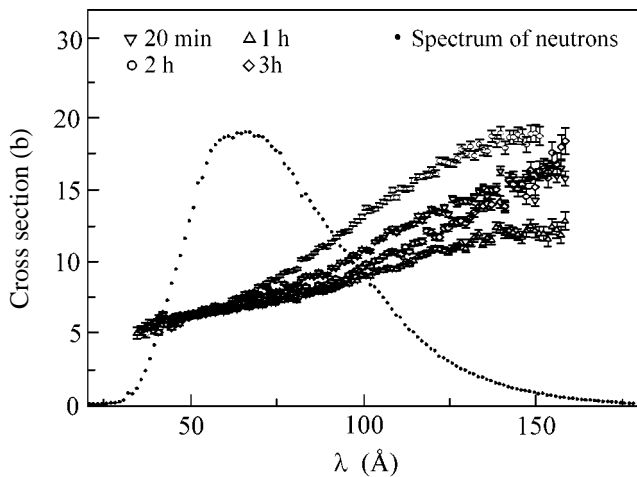
Fig. 2. Cross section as a function of the neutron wavelength for deuterium with the orthophase concentration of $(93 \pm 3)\%$ for different freezing times.
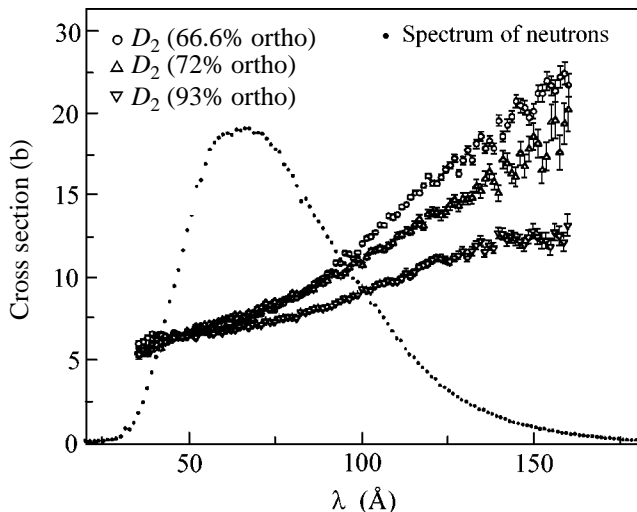

Fig. 3. Cross section as a function of neutron wavelength for different ortho–para ratios and for the same freezing time of 2 hours.

effect in the long-wavelength portion of the spectrum. This trend is also evident from our data.

To obtain the dependence of the scattering cross section on the ortho–para composition of deuterium, we compared the data obtained using the identical procedures of preparing the samples. Figure 3 depicts the cross-section data for different ortho–para ratios and for a freezing time of 2 h. A dependence of the scattering cross section on the deuterium ortho–para composition is observed for large λ. For instance, for neutrons

with a wavelength of about 150 Å, the total cross section for interaction with the normal deuterium molecules (66% of orthophase) is approximately 1.5 times larger than for the orthodeuterium (~93%). The behavior of the cross sections for neutrons with $\lambda > 150$ Å cannot be extracted from these data because of poor statistics for these portions of the spectrum and because of a relatively large uncertainty in our knowledge of the backgrounds.

This work demonstrates the importance of the SD_2 manufacturing technology for VCN and UCN sources, since the yield of these sources depends on the deuterium "transparency" to neutrons. The experimental dependence of the total cross section for VCN scattering on the ortho–para composition of deuterium was observed for the first time.

REFERENCES

1. S. Arzumanov, L. Bondarenko, S. Chernyavsky, *et al.*, Nucl. Instrum. Methods Phys. Res. A **440**, 511 (2000).
2. K. F. Smith, N. Camprin, J. M. Pendlebury, *et al.*, Phys. Lett. B **234**, 191 (1990).
3. I. S. Altarev, Yu. V. Borisov, N. V. Borovikova, *et al.*, Yad. Fiz. **59**, 1204 (1996) [Phys. At. Nucl. **59**, 1152 (1996)].
4. A. P. Serebrov, V. A. Mityukhlyaev, A. A. Zakharov, *et al.*, Pis'ma Zh. Éksp. Teor. Fiz. **59**, 728 (1994) [JETP Lett. **59**, 757 (1994)].
5. A. P. Serebrov, V. A. Mityukhlyaev, A. A. Zakharov, *et al.*, Pis'ma Zh. Éksp. Teor. Fiz. **62**, 764 (1995) [JETP Lett. **62**, 785 (1995)].
6. A. P. Serebrov, V. A. Mityukhlyaev, A. A. Zakharov, *et al.*, Nucl. Instrum. Methods Phys. Res. A **440**, 658 (2000).
7. A. P. Serebrov, V. A. Mityukhlyaev, A. A. Zakharov, *et al.*, Pis'ma Zh. Éksp. Teor. Fiz. **66**, 765 (1997) [JETP Lett. **66**, 802 (1997)].
8. C.-Y. Liu, A. R. Young, and S. K. Lamoreaux, Phys. Rev. B **62**, R3581 (2000).
9. A. Saunders, T. J. Bowles, B. W. Filippone, *et al.*, Bull. Am. Phys. Soc. **45**, 75 (2000).
10. A. N. Bazhenov, V. I. Medvedev, and A. N. Pirozhkov, Prib. Tekh. Éksp., No. 4, 63 (1992) [Instrum. Exp. Tech. **35**, 607 (1992)].

Equilibrium Orientation States in a System of Two Magnetic Layers with Antiferromagnetic Coupling

D. I. Sementsov and A. M. Shutyǐ

Ul'yanovsk State University, ul. L'va Tolstogo 42, Ul'yanovsk, 432700 Russia

Received July 31, 2001

The equilibrium orientations of magnetic moments are found for a system of two antiferromagnetically coupled magnetic films in an external magnetic field. Field intervals are found where the noncollinear and orientational bistability states occur, resulting in the orientation hysteresis and phase transition. © *2001 MAIK "Nauka/Interperiodica".*

PACS numbers: 75.70.Cn

1. In recent years, increased attention has been given to studying the magnetization ordering [1–3] and dynamics [4–6] of multilayer systems composed of alternating layers of a ferromagnetic metal and a nonmagnetic material. These processes are primarily governed by the type of coupling between the magnetic moments of the neighboring layers. In the absence of an external magnetic field, this coupling results either in ferromagnetic or antiferromagnetic ordering or in noncollinear ordering in the case of biquadratic exchange [7, 8]. A nonlinear interaction of an alternating field with magnetically ordered structures is accompanied by a number of effects such as a drastic increase in the precession angle under the FMR conditions [9, 10], the dynamic bistability, and the magnetization fractalization [11]. The same effects occur in a system of two dipole-coupled magnetic moments [12]. A search for the conditions which are most suitable for the excitation by a weak microwave field in various dynamic regimes, as well as the revelation of unstable states sensitive to small changes in the system parameters and field strength, primarily necessitates analysis of the equilibrium states of the system. In this connection, the equilibrium orientation states of magnetic moments are studied in this work for a system composed of two ferromagnetic layers separated by a nonmagnetic spacer to provide their antiferromagnetic coupling, with emphasis on various dynamic regimes which may occur in the system.

2. Let the system of two magnetically coupled layers be magnetized in its xy plane by an external field **H** oriented in this plane at an angle of α to the y axis. Each layer of thickness d_i possesses magnetization **M**$_i$, in-plane uniaxial anisotropy with a constant K_i, and easy axis coinciding with the y axis. In this case, the free energy of the system per film unit area is

$$E = \sum_{i=1,2} d_i \{ K_i \sin^2 \varphi_i - HM_i \cos(\alpha - \varphi_i) \cos \psi_i$$
$$- 2\pi M_i^2 \cos^2 \psi_i \} + AM_1 M_2 d_1 d_2 (d_1 + d_2)^{-1} \quad (1)$$
$$\times [\cos \psi_1 \cos \psi_2 \cos(\varphi_1 - \varphi_2) + \sin \psi_1 \sin \psi_2],$$

where A is the interlayer coupling constant, which, generally, depends on the spacer thickness, its material, and its structural characteristics; φ_i is the azimuthal angle (measured from the y axis) of the vector **M**$_i$; and ψ_i is the angle of its departure from the film plane. These angles specify the magnetization directions in the horizontal and vertical planes for each of the layers. For the assumed high demagnetizing fields ($4\pi M_i \gg H_{ki}$, AM_i) and the chosen orientation of the applied magnetic field about the layers, the equilibrium magnetizations lie in the plane of the system, so that the angles $\psi_i = 0$. To determine the equilibrium azimuthal angles φ_i, we use the equilibrium conditions $\partial E/\partial \varphi_i = 0$ and $\partial^2 E/\partial \varphi_i^2 > 0$ to obtain, using Eq. (1), the system of equations

$$K_i \sin 2\varphi_i - HM_i \sin(\alpha - \varphi_i)$$
$$- Ad_{3-i}(d_1 + d_2)^{-1} M_1 M_2 \sin(\varphi_i - \varphi_{3-i}) = 0,$$
$$H_{ki} \cos 2\varphi_i + H \cos(\alpha - \varphi_i) \quad (2)$$
$$- Ad_{3-i}(d_1 + d_2)^{-1} M_{3-i} \cos(\varphi_i - \varphi_{3-i}) > 0, \quad i = 1, 2.$$

We will assume that $A > 0$ to provide the antiferromagnetic coupling between the magnetic moments of the layers in the absence of the applied field, i.e., to provide their antiparallel orientation, namely, $\varphi_1 = 0$ and $\varphi_2 = \pi$ or vice versa. The applied field is chosen to be directed along the coinciding easy axes of the layers and, correspondingly, along their magnetizations; i.e., $\alpha = 0$ or π.

The calculations will be carried out with parameters close to those of real films of the Permalloy class: the anisotropy field $H_{ki} = 2K_i/M_i$; the magnetization of the first film $H_{k1} = 10$ Oe, $4\pi M_1 = 1.1 \times 10^4$ G; the magnetization of the second film $H_{k2} = 5$ Oe, $4\pi M_2 = 8 \times 10^3$ G; and the thicknesses of both films are the same, $d_1 = d_2 = 0.1$ μm.

3. Figure 1 shows the equilibrium azimuthal angles φ_1 and φ_2 for the magnetic moments of both films vs. applied field H oriented along the vector $\mathbf{M}_1$ in the initial state ($\alpha = 0$) for different coupling constants $A = (1, 2, 3, 4, 5) \times 10^{-2}$ (curves *1–5*). The dashed lines indicate the critical fields H_c for which the collinear equilibrium state with angles $\varphi_1 = 0$ and $\varphi_2 = \pi$ disappears. As the external magnetic field reaches H_c, the orientational phase transition occurs either in the film magnetized counterfield or in both films. In the first (collinear) case, which takes place at small coupling constants (curves *1, 2*), the magnetization of the second film reverses its direction and the vector $\mathbf{M}_2$ becomes parallel to $\mathbf{M}_1$. In the second (noncollinear) case, which occurs at large constants A (curves *3–5*), the magnetization reversal in the second film differs from 180° and induces a change in the magnetization direction in the first film as a result of the interaction of magnetic moments (angular repelling). The curves in Fig. 1 illustrate only one of the two possible noncollinear states of orientational bistability: as the $\varphi_2 = \pi$ state becomes unstable with an increase in the magnetic field, the magnetization of the second film can turn with equal probability to both $\varphi_2 < \pi$ and $\varphi_2 > \pi$ sides. Accordingly, the magnetization of the first film turns to the $\varphi_1 < 0$ or $\varphi_1 > 0$ side. The two resulting equilibrium states are symmetric about the direction of the applied field. As the field increases further, the angle between the film magnetizations decreases and becomes zero at $H = H_a$; i.e., the noncollinear states become degenerate.

If the magnetic moments of the films are initially codirected and the external field decreases, then one of the two symmetric noncollinear states will appear upon reaching the bifurcation point at $H = H_a$. The noncollinear regime occurs in the interval $H_b < H < H_a$, which broadens with increasing coupling constant. At $H = H_b$, the orientational phase transition occurs, resulting in the state with oppositely directed magnetic moments of the films. Note that $H_b \approx H_a$ at a small coupling constant (e.g., at $A = 0.01$), so that the noncollinear equilibrium states are practically absent. In addition, H_a and H_b may be both larger and smaller than H_c, depending on the value of coupling constant A. If $H_c > H_b$, as in the cases considered, then the orientational hysteresis appears upon cycling the external field. The hysteresis loop may be multiply shaped because of the presence of two equilibrium branches in the bifurcation pattern.

The exact value of the field H_c at which the state with antiparallel magnetic moments, i.e., the state with
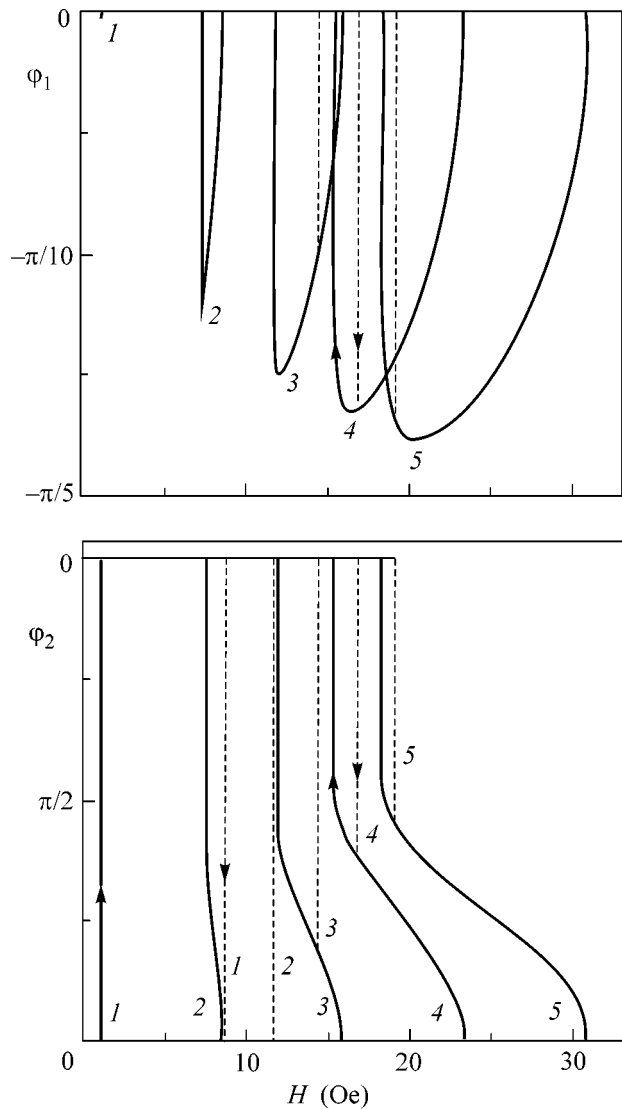

Fig. 1. Equilibrium orientations of the magnetic moments of both layers vs. external magnetic field H for different coupling constants A.

angles $\varphi_1 = 0$ and $\varphi_2 = \pi$, ceases to be equilibrium is given by

$$H_c = \frac{1}{4}(G_1 + \sqrt{G_1^2 + 8G_2}), \qquad (3)$$

where $G_1 = A(M_2 - M_1) + 2(H_1 - H_2)$ and $G_2 = A(M_1H_1 + M_2H_2) + 2H_1H_2$. The field H_a can be obtained from Eq. (3) by changing the signs of M_1 and H_1.

For the reversed direction of the applied field ($\alpha = \pi$), the situation is analogous: the equilibrium state with angles $\varphi_1 = 0$ and $\varphi_2 = \pi$ disappears upon reaching the critical field, and the magnetization of the first film changes its direction and induces a change in the magnetization direction in the second film if A is large enough ($A \geq 0.03$ in the case considered). The indicated
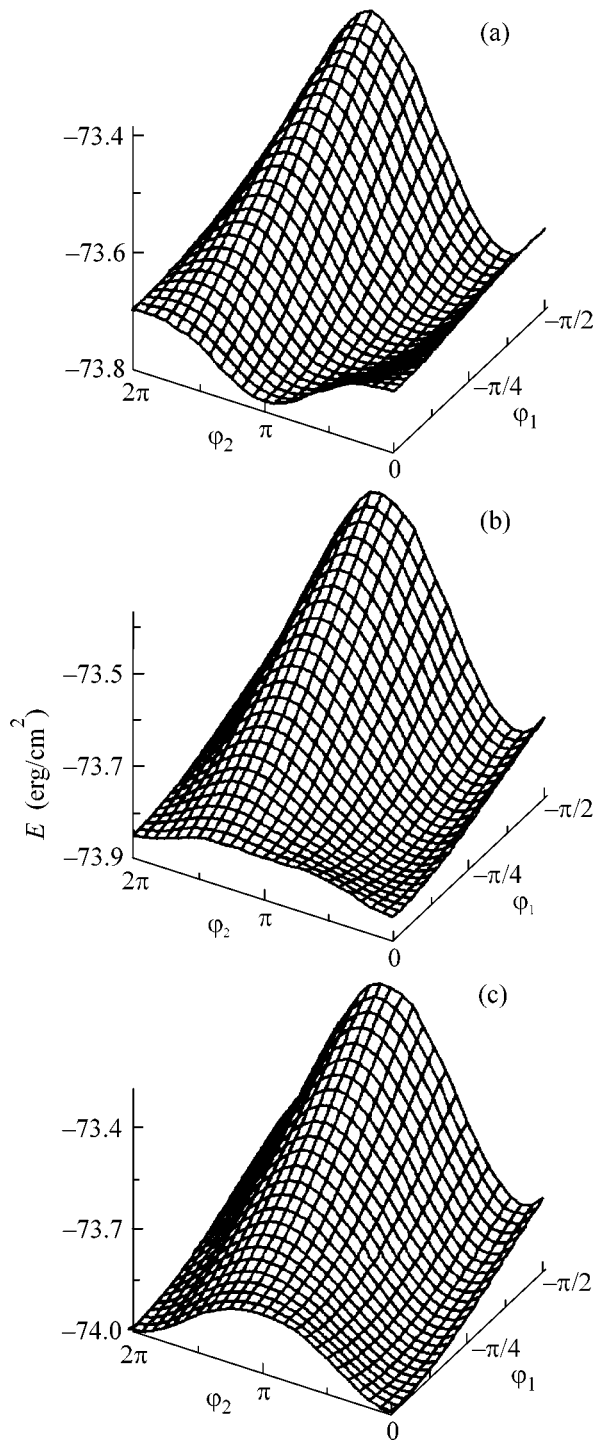
Fig. 2. Angular dependences of the free energy of the system for different values of magnetic field H.

critical field can be determined from Eq. (3) upon changing the sign of G_1.

Figure 2 shows the dependence of the free energy of the system on the orientations of the magnetic moments of both films for coupling constant $A = 5 \times 10^{-2}$ and external fields $H = 15$, 25, and 35 Oe (Figs. 2a, 2b, 2c,

respectively). It is seen that, at low fields ($H < H_c$), the energy minima correspond to oppositely directed magnetic moments (Fig. 2a). As the magnetic field increases, these energy minima are smoothed out and disappear. Simultaneously, another two centrosymmetric energy minima appear for the following orientations of magnetic moments: $-\pi/2 < \varphi_1 < 0$, $0 < \varphi_2 < \pi$ and $0 < \varphi_1 < \pi/2$, $-\pi < \varphi_2 < 0$ (Fig. 2b). These minima are shifted upon further increase in H, and, eventually, a state with parallel magnetic moments is established (Fig. 2c).

The above analysis demonstrates that a two-layer magnetically coupled system with a nonmagnetic interlayer providing the antiferromagnetic type of interaction between the magnetic moments of the layers ($A > 0$) undergoes orientational phase transitions resulting in the collinear and noncollinear states of the film magnetic moments. It is found that a change in the magnetic field strength is accompanied by the appearance of variously shaped orientational hystereses. The latter appear because the states with both two and three stationary orientations of magnetic moments are present in the system.

REFERENCES

1. V. V. Ustinov, M. M. Kirillov, I. D. Lobov, *et al.*, Zh. Éksp. Teor. Fiz. **109**, 477 (1996) [JETP **82**, 253 (1996)].

2. V. V. Kostyuchenko and A. K. Zvezdin, J. Magn. Magn. Mater. **176**, 155 (1997).

3. R. W. Wang and D. L. Mills, Phys. Rev. B **50**, 3931 (1994).

4. R. S. Iskhakov, I. V. Gavrishin, and L. A. Chekanova, Pis'ma Zh. Éksp. Teor. Fiz. **63**, 938 (1996) [JETP Lett. **63**, 989 (1996)].

5. N. G. Bebenin and V. V. Ustinov, Fiz. Met. Metalloved. **84**, 29 (1997).

6. N. M. Kreines, A. N. Kolmogorov, and V. F. Mescheriakov, J. Magn. Magn. Mater. **177–181**, 1913 (1998).

7. A. Schreyer, J. F. Ankner, Th. Zeidder, *et al.*, Phys. Rev. B **52**, 16066 (1995).

8. G. S. Patrin, N. V. Volkov, and V. P. Kononov, Pis'ma Zh. Éksp. Teor. Fiz. **68**, 287 (1998) [JETP Lett. **68**, 307 (1998)].

9. A. G. Temiryazev, M. P. Tikhomirova, and A. V. Maryakhin, in *Proceedings of the 16th International School-Workshop on New Magnetic Materials for Microelectronics, Moscow, 1998*, Part 1, p. 270.

10. A. M. Shutyĭ and D. I. Sementsov, Zh. Éksp. Teor. Fiz. **118**, 110 (2000) [JETP **91**, 531 (2000)].

11. S. M. Rezende and F. M. de Aguiar, Proc. IEEE **78** (6), 893 (1990).

12. F. V. Lisovskiĭ and O. P. Polyakov, Pis'ma Zh. Éksp. Teor. Fiz. **68**, 643 (1998) [JETP Lett. **68**, 679 (1998)].

Translated by V. Sakun

Raman Scattering Enhancement using Crystallographic Surface of a Colloidal Crystal[1]

S. V. Gaponenko[1]*, A. A. Gaiduk[1], O. S. Kulakovich[1], S. A. Maskevich[2], N. D. Strekal[2], O. A. Prokhorov[3], and V. M. Shelekhina[3]

[1] *Institute of Molecular and Atomic Physics, National Academy of Sciences of Belarus, Minsk, 220072 Belarus*
*e-mail: gaponen@imaph.bas-net.by
[2] *Kupala State University, Hrodna, 230023 Belarus*
[3] *Institute for Powder Metallurgy, Minsk, 220600 Belarus*
Received August 7, 2001

Deposition of coinage metals on a crystallographic surface of a colloidal crystal is proposed with the aim of fabricating metal surfaces with a regular relief on a scale of 200–300 nm to get strong surface-enhanced Raman scattering (SERS). The approach is implemented through thin gold-film deposition on a surface of a crystal consisting of silica globules. Mitoxantrone molecules, a DNA intercalator, were used to prove high SERS efficiency of the structures proposed. As compared to other SERS-active substrates, metal–dielectric colloidal crystal structures possess well-defined surface parameters (globule diameter and film thickness), high stability and reproducibility. These advantages are important for systematic analysis of SERS mechanisms in mesoscopic structures and its application in single-molecule detection. © 2001 MAIK "Nauka/Interperiodica".

PACS numbers: 81.16.-c; 33.20.Fb; 82.70.Dd

Strong enhancement of Raman scattering of light by molecules adsorbed at surfaces of coinage metals (Au, Pt, Ag, Ni) with a complicated nanorelief, as compared to solutions and flat dielectric surfaces (so-called surface-enhanced Raman scattering, SERS), has been extensively investigated over more than two decades ([1–3] and refs. therein). A description of this complex phenomenon, in spite of an extensive research, is far from being complete. Recent pioneering experiments on single-molecule detection by means of SERS [4, 5] showed that local Raman scattering enhancement factor in metal–dielectric structures can be as large as 10^{14}. These findings stimulated further experimental studies of interaction of electromagnetic field with metal colloidal [6], fractal [7], and periodic surface structures [8], as well as with metal nanoshells [9]. A serious obstacle in systematic SERS research, its quantitative description, and practical applications is the absence of reliable techniques allowing fabrication of reproducible and well-defined SERS-active substrates with homogeneous size and shape of metal nanoparticles. Etched metal electrodes, island films, isolated colloidal particles, their small and larger fractal clusters, and other metal–dielectric structures with irregular nanorelief and complicate topology are used in SERS experiments. Each of these SERS-active structures features spatial inhomogeneities which are hard to describe mathematically and reproduce experimentally. Because of the uniqueness of each structure, a systematic analysis of data reported by different groups and their comparison with model theoretical calculations become ambiguous. In spite of challenging opportunities of SERS in single-molecule detection, further research is necessary for the understanding of underlying physical processes and its practical applications.

Several groups outlined pronounced SERS effect for molecules adsorbed at metal surfaces with regular displacement of islands, rods, or globules [2, 10, 14]. In this case, SERS can be described in terms of the model in which 10^6-fold enhancement occurs due to excitation of surface plasmons [11, 12]. Resonant enhancement of Raman scattering was reported at a specific laser wavelength for a given metal particle size [13]. Therefore, for the highest SERS efficiency, a regular two-dimensional arrangement of monodisperse metal islands or globules is desirable. Though monodispersity can be achieved by means of size fractionating and using nanoshells over monodisperse colloidal globules, spatial ordering of structures remains to be performed by other means. To fabricate periodic SERS-active substrates, nanolithography has been proposed [14] providing superior SERS response. This technique, however, is rather complicated, expensive, and includes specific processes which cannot be reduced to chemical processing.

In this letter, we propose to fabricate SERS-active periodic metal–dielectric two-dimensional nanostructures by means of metal deposition on a crystallographic surface of a colloidal crystal and report the first

---

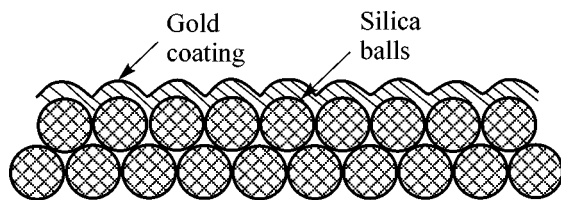[1] This article was submitted by the authors in English.

Fig. 1. A scheme of periodic metal–dielectric structures formed by gold deposition on silica colloidal crystal surface.
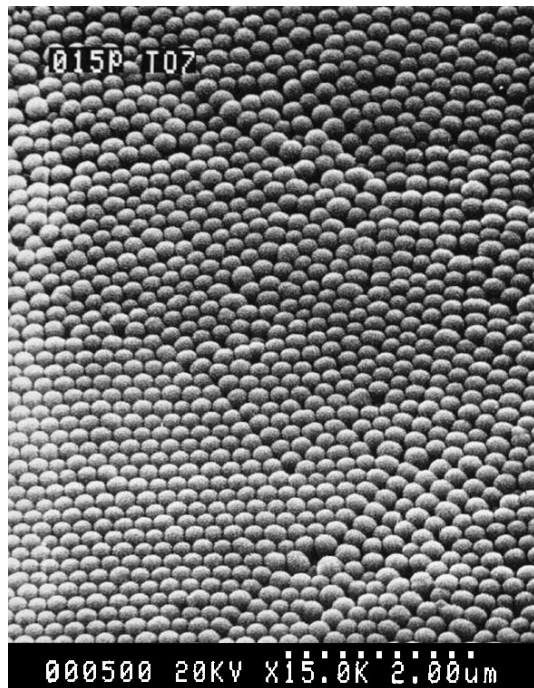

Fig. 2. Transmission electron microscopy image of a colloidal crystal coated with 20-nm Au film. The globule size is about 200 nm.
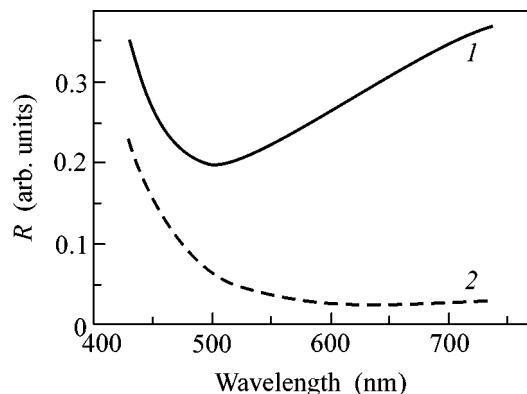

Fig. 3. Reflection spectrum of the colloidal crystal surface (*1*) with and (*2*) without a thin gold film deposited thereon.

observation of pronounced Raman scattering enhancement at a colloidal crystal surface.

In the experiments, colloidal silica crystals were developed by means of centrifugation of monodisperse silica sol with the mean particle diameter varying in the range 200–500 nm. Similar structures fabricated by means of sedimentation were used earlier as model systems in fabricating three-dimensional photonic crystals for the optical spectral range [15–17]. Gold films 20 nm thick were developed on a colloidal crystal surface by means of a conventional vacuum deposition. A scheme of the structure proposed and a surface image obtained with a scanning electron microscope are presented in Figs. 1 and 2. Macroscopically, the colloidal structures investigated are polycrystals with total volume in the range of 1 to 100 mm^3 with single crystal blocks from a few to tens of microns.

The original surface of a colloidal crystal exhibits diffuse reflectance similar to that established for α-quartz (Fig. 3). Because of macroscopic disorder inherent in the structures over sample surface and volume, coherent effects of light propagation were not pronounced when relatively large samples (10 mm^3) of colloidal crystals were examined. A colloidal crystal surface coated with a thin gold film exhibits pronounced enhancement of reflectivity, with the reflection coefficient monotonically increasing with wavelength (Fig. 3). This behavior is characteristic of thin metal films.

To test SERS efficiency of the substrates developed, mitoxantrone molecules were deposited from an aqueous (10^{-6} M) solution on the surface of gold-coated colloidal crystals. Mitoxantrone is a DNA intercalator and an anticancer drug currently used in clinical trials of non-Hodgkin's lymphomas, acute myeloid leukemia, and advanced breast cancer [18]. It is a promising complex for single-molecule detection in cell organelles [19]. Earlier mitoxantrone probes were used to show that the same gold film, if properly processed, can be used both for Raman scattering and for fluorescence enhancement [20].

Measurements performed with a cw laser excitation (wavelength 633 nm, excitation power density about 10 mW/cm^2) showed that the metal-coated surface of a colloidal crystal provided an extreme Raman scattering enhancement (Fig. 4). Raman signal intensity is at least 5 times higher for molecules adsorbed at the colloidal crystal surface, as compared to molecules at the reference metal island film deposited under similar conditions on a plane glass plate. Note that the Raman signal for mitoxantrone deposited on a dielectric surface with the same excitation/registration setup is not detectable at all. The true local enhancement factor of Raman scattering by molecules adsorbed at the colloidal crystal surface is significantly larger than that observed in the experiments under condition of data acquisition from a relatively large (as compared to the globule size) surface area. Because of colloidal crystal porosity, the sur-
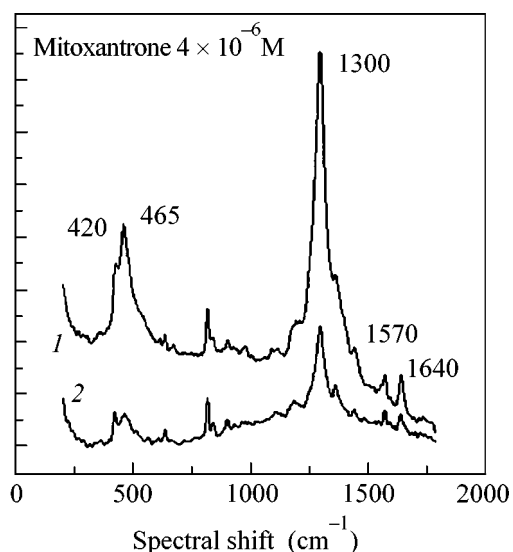
Fig. 4. Raman scattering spectra by mitoxantrone molecules adsorbed at a 20-nm thick gold film deposited (*1*) on a colloidal crystal and (*2*) on a reference glass plate.

face concentration of test molecules is lower than in the case of deposition on a flat surface.

A controllable lattice period provided by means of the original sol precipitation made it possible to examine size-selective features of the SERS effect. In accordance with the previously reported observations [13], we found that the size-selective enhancement with respect to a given laser wavelength occurs. For a laser wavelength of 633 nm, the Raman signal was found to decrease by more than one order of magnitude when the globule diameter increased from 250 to 500 nm.

Diffuse scattering at the long-wavelength side of the Rayleigh component in the structures investigated results from multiple incoherent scattering in a complex colloidal structure. It can be diminished when using a small number of colloidal layers (down to a single monolayer) or impregnating a colloidal crystal with immersing gel [21]. Optimization of excitation conditions (increase in excitation wavelengths to 700–800 nm or decrease in globule size to 150–180 nm) can increase SERS intensity considerably. With constant globule size, SERS efficiency can be increased for laser wavelengths in the visible region if silver films are used instead of gold ones. This will happen because of the better overlap of the laser wavelength with plasmon resonance.

In conclusion, the first observation of strong Raman scattering enhancement of molecules adsorbed at a metallized colloidal crystal surface is reported. Well-defined physical and geometrical characteristics of the structures proposed, along with their good reproducibility and high durability, will make it possible to perform systematic studies of Raman scattering enhancement due to excitation of surface plasmons and its

application in single-molecule detection. As compared to the recently reported three-dimensional metal structures fabricated by means of colloidal templating [22], the metal-coated colloidal crystals considered in this letter provide adsorption of the probe molecules directly at the surface, which increases sensitivity of the method and is of vital importance in single-molecule detection.

REFERENCES

1. *Surface Enhanced Raman Scattering*, Ed. by R. K. Chang and T. E. Furtak (Plenum, New York, 1982; Mir, Moscow, 1984).
2. I. Nabiev, R. G. Efremov, and G. D. Chumanov, Usp. Fiz. Nauk **154**, 459 (1988) [Sov. Phys. Usp. **31**, 241 (1988)].
3. Z. Q. Tian, Int. J. Vibr. Spectrosc. **4**, 2 (2000) (www.ijvs.com).
4. S. Nie and S. R. Emory, Science **275**, 1102 (1997).
5. K. Kneipp, Y. Wang, H. Kneipp, *et al.*, Phys. Rev. Lett. **78**, 1667 (1997).
6. A. M. Michaels, M. Nirmal, and L. E. Brus, J. Am. Chem. Soc. **121**, 9932 (1999).
7. W. Kim, V. P. Safonov, V. M. Shalaev, and R. L. Armstrong, Phys. Rev. Lett. **82**, 4811 (1999).
8. S. Linden, J. Kuhl, and H. Giessen, Phys. Rev. Lett. **86**, 4688 (2001).
9. S. J. Oldenburg, S. L. Westcott, R. D. Averitt, and N. J. Halas, J. Chem. Phys. **111**, 4729 (1999).
10. A. Feofanov, E. Ianoul, E. Kryukov, *et al.*, Anal. Chem. **69**, 3731 (1997).
11. F. J. Garacia-Vidal and J. B. Pendry, Prog. Surf. Sci. **50**, 55 (1995).
12. M. Xu and M. J. Dignam, J. Chem. Phys. **100**, 197 (1994).
13. J. T. Krug, G. D. Wang, S. R. Emory, and S. Nie, J. Am. Chem. Soc. **121**, 9208 (1999).
14. M. Kahl, E. Voges, S. Kostrewa, *et al.*, Sens. Actuators B **51**, 285 (1998).
15. V. N. Bogomolov, S. V. Gaponenko, I. N. Germanenko, *et al.*, Phys. Rev. E **55**, 7619 (1997).
16. E. P. Petrov, V. N. Bogomolov, I. I. Kalosha, and S. V. Gaponenko, Phys. Rev. Lett. **81**, 77 (1998); **83**, 5402 (1999).
17. S. V. Gaponenko, A. M. Kapitonov, V. N. Bogomolov, *et al.*, Pis'ma Zh. Éksp. Teor. Fiz. **68**, 131 (1998) [JETP Lett. **68**, 142 (1998)].
18. T. D. Shenkenberg and D. D. von Hoff, Ann. Intern. Med. **105**, 67 (1986).
19. A. Feofanov, S. Sharonov, I. Kudelina, *et al.*, Biophys. J. **73**, 3317 (1997).
20. N. Strekal, A. Maskevich, S. Maskevich, *et al.*, Biopolymers **57**, 325 (2000).
21. M. Kapitonov, N. V. Gaponenko, V. N. Bogomolov, *et al.*, Phys. Status Solidi A **165**, 119 (1998).
22. M. Tessier, O. D. Velev, A. T. Kalambur, *et al.*, J. Am. Chem. Soc. **122**, 9554 (2000).

New Mechanism of Current-Induced Cooling of Quantum Systems

E. B. Dogonkin and G. G. Zegrya

Ioffe Physicotechnical Institute, Russian Academy of Sciences, Politekhnicheskaya ul. 26,
St. Petersburg, 194021 Russia

Received August 8, 2001

A new mechanism of current-induced cooling of heterostructures is proposed and studied. As an example, a structure with two quantum wells was taken to determine the conditions under which electric current can flow in the situation where electrons and holes transfer from one well to another via indirect phonon-assisted tunneling. It is shown that this system can be used to create an inverse electron and hole population and simultaneously cool the laser active region by injection current. The universal relation is obtained according to which the cooling temperature of a quantum system is expressed only in terms of energy difference between the carrier size-quantization levels. © *2001 MAIK "Nauka/Interperiodica".*

PACS numbers: 72.15.Jf; 73.40.Gk

1. Mechanism of carrier tunneling through heterostructure with phonon absorption. At present, it has become possible to devise practically ideal semiconducting nanoheterostructures and defectless, due to lattice matching, superlattices on their basis [1]. The corresponding geometrical sizes of layers and the heterobarrier heights can be controlled with a high accuracy. For such ideal heterostructures, the mechanism of current flow through the interfaces is highly topical.

It is known that the current flow through a contact of two different metals is accompanied by Peltier heat absorption (or release) [2]. In semiconducting heterostructures, one more mechanism of current-induced cooling is possible.

Let us consider the mechanism of current flow through a heterostructure with quantum wells (QWs), as shown in Fig. 1. The quantum structure (QS) consists of two QWs of different width for electrons and two QWs for holes. The QWs are situated between the *N*- and *P*-doped regions, which serve as electron and hole emitters, respectively. The width of the second QW for electrons and holes is chosen so that the size-quantization level E_2 lies higher than the energy level E_1 in the first QW (Fig. 1).

Let an external direct bias be applied to this structure. Then electrons from emitter *N* can transfer to the first QW by tunneling through the first barrier; however, their tunneling into the second QW is suppressed due to the presence of two heterobarriers. Consequently, the probability of direct electron tunneling from emitter *N* to the second QW is exponentially low, because there is no resonance level in the first QW. The electrons localized in the first QW also cannot tunnel into the second QW in a usual way, because this transition is forbidden by the energy and longitudinal quasi-momentum conservation laws. The energies of electrons with identical longitudinal quasimomenta in the first and second QWs differ by $E_2 - E_1$ (Fig. 2). For this reason, electrons transfer from the first QW to the second one due to the indirect phonon-assisted tunneling effect [3].

Evidently, the hole transport proceeds in a similar fashion. For the sake of brevity, we restrict ourselves to electron tunneling involving optical phonons. The calculations for hole tunneling are fully analogous, except for the effective masses.

It is known that electrons and holes in semiconductors interact rather strongly with longitudinal optical phonons at high (on the order of room) temperatures [4, 5]. For this reason, the probability of indirect electron tunneling from the first QW to the second QW with absorption of a longitudinal optical (LO) phonon can be appreciable. Evidently, this tunneling will be particularly efficient if the size-quantization energies satisfy the equality $E_2 - E_1 = \hbar\omega_0$, where ω_0 is the frequency of the LO phonon.

The purpose of this work was to investigate the ambipolar mechanism of current flow through a heterostructure with indirect electron and hole tunneling from one QW to another followed by electron–hole recombination (Fig. 1). With such a mechanism, Joule heat is released in emitters *N* and *P*, while in the QS heat is absorbed, because, when passing through the heterostructure, every charge carrier (electron or hole) takes away a portion of lattice energy equal to the energy of an LO phonon and recombines with an oppositely charged carrier to emit a $\hbar\omega$ photon. We assume that the band gap in emitters *N* and *P* is larger than $\hbar\omega$, so that light is not absorbed in the system. As a result, the quantum structure is cooled to a temperature T_Q, which
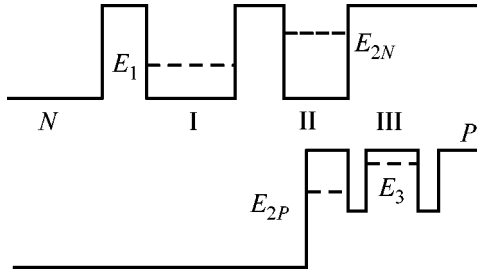
Fig. 1. Ambipolar quantum structure. From left to right: *N*-doped region (electron emitter), QW I for electrons, QW II for electrons and holes, QW III for holes, and *P*-doped region (hole emitter).
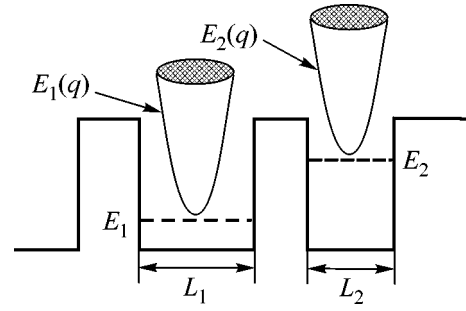

Fig. 2. Electron dispersions in the first and second QWs. As can be seen, electrons with the same longitudinal quasimomenta have different energies. The situation for holes is similar.

depends nonmonotonically on the current j flowing through the system. In this work, the current j_E is determined for which the cooling temperature T_C (difference between the heat-bath temperature T_0 and the QS temperature T_Q, $T_C = T_0 - T_Q$) is maximal. A universal relation is deduced according to which the maximum cooling temperature is expressed only in terms of the characteristic size-quantization energies $E_2 - E_1$ [see below Eq. (24)].

The rate W^c_{12} of electron tunneling from the size-quantization level E_1 to the level E_2 with phonon absorption can be calculated using the standard first-order perturbation theory to arrive at the Fermi golden rule [3, 6]

$$W^c_{12} = \frac{2\pi}{\hbar}\Sigma_{1,2,P}|M|^2 f_1(E_1)(1 - f_2(E_2))$$
$$\times b(\hbar\omega_0)\delta(E_2 - E_1 - \hbar\omega_0), \quad (1)$$

where $f_i(E_i)$ is the Fermi electron distribution function, $b(\hbar\omega_0)$ is the Planck phonon distribution function, and the matrix element of electron–phonon interaction is [5, 7]

$$M = g(\mathbf{q}_P)\int d^3 r \psi_1(\mathbf{r})\frac{\exp(i\mathbf{q}_P\mathbf{r})}{\sqrt{V}}\psi_2(\mathbf{r}), \quad (2)$$

where $g(\mathbf{q}_P)$ is the electron–phonon coupling constant, $\psi_i(\mathbf{r})$ are the electron wave functions, V is volume, and q_P is the phonon quasimomentum.[1] Due to the weak dispersion of LO phonons, $g(\mathbf{q}_P)$ can be approximated as [4, 7]

$$|g(\mathbf{q}_P)|^2 = 2\pi e^2 \hbar\omega_0/q_P^2 \epsilon^*, \quad (3)$$

where $1/\epsilon^* = 1/\epsilon_\infty - 1/\epsilon_0$.

Substituting Eqs. (2) and (3) into Eq. (1), averaging over the initial states, and integrating over the final

---

[1] The phonons are assumed to be three-dimensional.

states, one obtains the following expression for the rate of electron tunneling with phonon absorption:

$$W^c_{12} = \frac{e^2 \omega_0 m_c \tilde{c}^2}{8\pi^2 L_2 \epsilon^* \hbar}$$
$$\times \frac{\exp((\mu_1 + \hbar\omega_0 - \mu_2)/2kT)}{\exp(\hbar\omega_0/kT) - 1}(J_1 + J_2), \quad (4)$$

where

$$J_i = \frac{1}{2A_i}\int_{\sqrt{B_i}}^{\infty}\frac{dx}{C + \cosh(x^2/x_i^2 + \gamma_i)},$$

$$A_i = (k_1 \pm k_2)^2,$$

$$B_i = k_1(k_1 \pm k_2)\left(k_1^2 \pm k_1 k_2 + 2\frac{m_c\omega_0}{\hbar}\right) + \left(\frac{m_c\omega_0}{\hbar}\right)^2,$$

$$C = \cosh\frac{\mu_2 - \mu_1 - \hbar\omega_0}{2kT}, \quad (5)$$

$$\tilde{c} = \frac{1}{\cos(k_2 L_1)\cosh(\kappa_2 L) + \frac{\kappa_2}{k_2}\sin(k_2 L_1)\sinh(\kappa_2 L)},$$

$$x_i = \frac{\sqrt{2m_c kT}}{\hbar}(k_2 \pm k_1),$$

$$\gamma_i = \frac{2E_1 + \hbar\omega_0 - \mu_1 - \mu_2}{2kT} - \frac{B_i}{A_i},$$

k_i and κ_i are the transverse quasimomenta of electrons with energy E_i in the QW and under the barrier, respectively; L_i is the width of the *i*th QW; and L is the barrier width.

Similarly, one obtains for the rate W_{21}^c of electron tunneling from level E_2 to level E_1 with emission of an LO phonon

$$W_{21}^c = W_{12}^c \frac{b(\hbar\omega_0) + 1}{b(\hbar\omega_0)} \exp\left(\frac{\mu_2 - \mu_1 - \hbar\omega_0}{kT}\right)$$

$$= W_{12}^c \exp\left(\frac{\mu_2 - \mu_1}{kT}\right). \tag{6}$$

The hole tunneling rates can be obtained from Eq. (6) by substituting hole parameters for the electron parameters.

2. Stationary regime. Since the characteristic time τ_I of intraband carrier relaxation is much shorter than the tunneling time τ_T and the radiative recombination time τ_R ($\tau_I \ll \tau_T, \tau_R$) [8], one can assume that each QW has its own electronic μ_1 or hole μ_2 Fermi quasilevel in the stationary regime (Fig. 1). We will assume that the electron tunneling from emitter N to QW I and the hole tunneling from emitter P to QW III are fast enough so that the Fermi quasilevels in the emitters and in the corresponding QWs coincide with each other. The electronic Fermi quasilevel in the second QW can be found from the balance equation for electrons

$$W_R = W_{12}^c - W_{21}^c, \tag{7}$$

where W_R is the carrier radiative recombination rate in QW II.

The hole Fermi quasilevel in QW II is found from the analogous balance equation for holes,

$$W_R = W_{32}^h - W_{23}^h. \tag{8}$$

In what follows, the leakage currents and the Auger recombination will be ignored, because one can always choose an optimum structure where these processes are suppressed. In particular, the spatially indirect (diagonal) tunneling recombination of electrons from QW I and holes from QW III will be disregarded. The two-dimensional radiative recombination rate can be represented as [9]

$$W_R \approx \frac{\pi}{2} \frac{\epsilon_\infty}{\sqrt{\epsilon_0}} \frac{e^2}{\hbar c} \frac{\tilde{E}_g}{\hbar} \frac{\tilde{E}_g}{m_c c^2} \frac{\hbar^2}{2m_h kT} n_2 p_2, \tag{9}$$

where $\tilde{E}_g$ is the effective band gap in the second QW, $\tilde{E}_g = E_g + E_2 + E_h$ (E_h is the ground size-quantization hole level), and n_2 and p_2 are the two-dimensional electron and hole concentrations in the second QW, respectively:

$$n_2 = \frac{m_c kT}{\pi\hbar^2} \ln\left(\exp\frac{\mu_2 - E_2}{kT} + 1\right)$$

$$= N_c^{2D} \ln\left(\exp\frac{\mu_2 - E_2}{kT} + 1\right) \tag{10}$$

and

$$p_2 = \frac{m_h kT}{\pi\hbar^2} \ln\left(\exp\frac{\mu_2^h - E_2}{kT} + 1\right)$$

$$= N_h^{2D} \ln\left(\exp\frac{\mu_2^h - E_2}{kT} + 1\right). \tag{11}$$

Since the right-hand sides of balance Eqs. (7) and (8) monotonically decrease with increasing carrier concentration in QW II, while the radiative recombination rate increases, the stationary state is established in the system. When solving numerically the set of balance equations, we first equalize the right-hand sides of Eqs. (7) and (8) to obtain the relationship between the hole and electron concentrations in QW II, whereupon we solve Eq. (7) using Eq. (9) for the radiative recombination rate, where the hole concentration is expressed through the electron concentration. The current density $j = e W_R$ through the system is determined by the QS temperature T_Q and the pump level (i.e., position of the Fermi quasilevel μ_1 in emitters N and P) (Fig. 3).

Let us now consider the conditions under which the inverse charge-carrier population can be created in the second QW. The maximum gain at $\hbar\omega = \tilde{E}_g$, as calculated using the Kane model, has the form [10]

$$g_0^{max} \approx I_{cv}^2 \frac{\pi}{L_2} \frac{e^2}{\hbar c \sqrt{\kappa}} \frac{E_g(E_g + \Delta_{so})}{E_g + \frac{2}{3}\Delta_{so}} \frac{1}{\tilde{E}_g}$$

$$\times \left[\left(\exp\left(\frac{E_2 - \mu_2}{kT}\right) + 1\right)^{-1} \right. \tag{12}$$

$$\left. + \left(\exp\left(\frac{E_h - \mu_h}{kT}\right) + 1\right)^{-1} - 1\right],$$

where I_{cv} is the overlap integral between the electronic and hole wave functions in QW II, and Δ_{so} is the spin–orbit splitting constant. The inversion threshold is achieved at $g_0^{max} = 0$. The equation for the threshold electron n_2^{thr} and hole p^{thr} concentrations in QW II can be obtained from Eq. (12):

$$\exp\left[-\frac{n_2^{thr}}{N_c^{2D}}\right] + \exp\left[-\frac{1}{M}\frac{p_2^{thr}}{N_c^{2D}}\right] = 1, \tag{13}$$

where $M = m_h/m_c$. When deriving Eq. (13), relationship (10) between the two-dimensional carrier concentration and the position of the Fermi quasilevel was taken into account. Using conditions (7)–(9) and (13), one can find the electron concentration at the inversion threshold n_2^{thr}.

3. Heat balance. Let us consider the passage of electric current through the system composed of the QS and two emitters N and P, each of length L_0, placed

between two heat sinks (Fig. 1). We assume that the heat-bath temperature is T_0. The passage of current j through the emitters is accompanied by Joule heat release with power density P_J,

$$P_J = 2L_0 j^2 \rho, \qquad (14)$$

where ρ is the emitter resistivity; it is assumed, for simplicity, that ρ is identical for the N and P regions.[2]

When passing through the quantum-dimensional structure considered above (Fig. 1), each electron and each hole absorbs a phonon and takes away a portion of lattice energy $\hbar\omega_0$, leading to heat absorption with power density

$$P_Q = 2j\hbar\omega_0/e \qquad (15)$$

in the quantum structure.

The temperature distribution in the system can be found from the heat energy (Q) conservation law,

$$dQ/dt = \operatorname{div} \underline{j}_Q = 0, \qquad (16)$$

where

$$j_Q = -\kappa \frac{dT}{dx} \qquad (17)$$

is the heat flux density and κ is the heat conductivity.

Equation (16) must be solved with the boundary conditions

$$T(x = -L_0) = T(x = L_0) = T_0. \qquad (18)$$

This yields the following spatial temperature distribution in emitters N and P:

$$T(x) = T_0 - \frac{1}{\kappa}\left((L_0 - |x|)\frac{j\hbar\omega_0}{e} - (L_0^2 - x^2)\frac{j^2\rho}{2}\right). \quad (19)$$

The temperature distribution for different values of electric current flowing through the system is shown in Fig. 4a.

Now, the following conclusions can be drawn. First, the system is cooled upon passing current if $P_J < P_Q$, and, second, the QS temperature $T_Q = T(x = 0)$ is lower than the ambient temperature T_0 if $P_J < 2P_Q$.

4. Cooling temperature. The current dependence of the QS temperature $T_Q = T(x = 0)$ can be determined by setting $x = 0$ in Eq. (19):

$$T_Q(j) = T_0 - \frac{jL_0\hbar\omega_0}{\kappa e} + \frac{j^2\rho L_0^2}{2\kappa} = T_0 + \frac{L_0}{2\kappa}(P_J - P_Q). \quad (20)$$

The corresponding curves are shown in Fig. 4b. It is seen that the $T_Q(j)$ dependence is nonmonotonic, and there is an optimum current density j_E in the system for which the cooling of the quantum structure is most efficient:

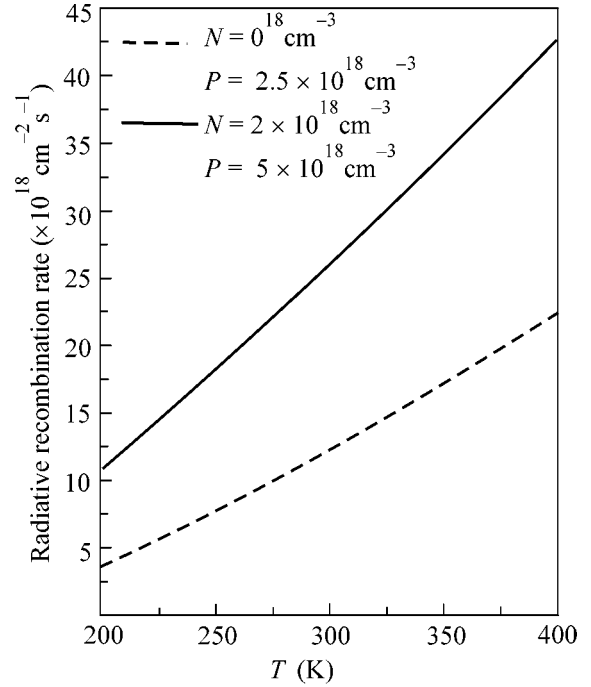[2] The Thompson heat is ignored because the temperature in emitters is assumed to be homogeneous.

Fig. 3. Current through the quantum structure vs. temperature for different levels of emitter doping: $N = 10^{18}$ cm^{-3}, $P = 2.5 \times 10^{18}$ cm^{-3} and $N = 2 \times 10^{18}$ cm^{-3}, $P = 5 \times 10^{18}$ cm^{-3}.

$$j_E(L_0) = \hbar\omega_0/L_0\rho e. \qquad (21)$$

Note that the maximum cooling temperature $T_C = \max(T_0 - T_Q)$ is independent of the emitter length L_0:

$$T_C = (\hbar\omega_0)^2/2e^2\rho\kappa. \qquad (22)$$

Making use of the Wiedemann–Franz law, i.e., the relation between heat conductivity κ and electrical conductivity $\sigma = 1/\rho$,

$$\kappa = \pi^2 T/3e^2\rho, \qquad (23)$$

one finally obtains an expression for the maximum cooling temperature T_C:

$$T_C = \frac{3}{2\pi^2}\frac{(\hbar\omega_0)^2}{T_0}. \qquad (24)$$

We obtained a universal relationship for the maximum cooling temperature of a quantum structure with ohmic contacts. The cooling temperature T_C depends on a single system parameter, namely, on the characteristic energy scale $E_2 - E_1 \approx \hbar\omega_0$ of the quantum structure. It should be noted that relationship (24) is valid only for sufficiently small cooling temperatures, $T_C \ll T_0$, otherwise it would be necessary to take into account the coordinate dependence of the electric and thermal conductivities.
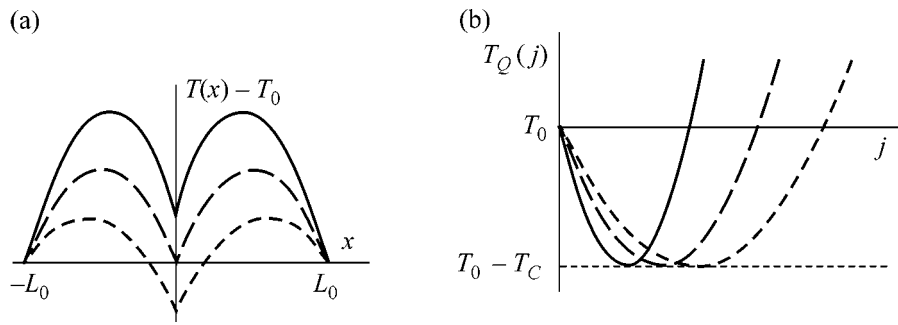
(a)

$T(x) - T_0$

x

$-L_0$ L_0

(b)

$T_Q(j)$

T_0

j

$T_0 - T_C$

Fig. 4. (a) Temperature T as a function of coordinate. As can be seen, the QS temperature $T_Q = T(x = 0)$ is lower than the heat-bath temperature $T_0 = T(x = \pm L_0)$. (b) The QS temperature T_Q as a function of the current flowing through the sample for different lengths L_0. As can be seen, the maximum cooling temperature $T_C = T_0 - T_Q(j_E)$ is independent of the emitter length L_0.

In a technologically simpler structure, in which only holes or only electrons are tunneling with the absorption of optical phonons, the maximum cooling temperature T_{SC} amounts to

$$T_{SC} = T_C/4. \tag{25}$$

5. Thermal stability. Note that, because of the nonmonotonic current dependence of cooling temperature, there is a region at $j < j_E$ where this temperature increases with current. One can see from Fig. 3 that the current flowing through the system monotonically increases with temperature. Therefore, there is a negative feedback from the current passing through the system on its temperature. This implies that a decrease in the QS temperature upon increasing current at $j < j_E$ partially compensates the carrier heating. As a result, the quantum system is thermally stable at these currents and, hence, it shows little sensitivity to the ambient temperature T_0.

The suggested principle of cooling quantum systems can be used for the temperature stabilization of semiconductor heterostructure lasers. As is pointed out above, the inverse charge-carrier population can be created using the cooling QSs (Fig. 1) [11]. Moreover, the temperature stabilization of semiconductor heterostructure lasers is also possible upon sequential disposition of the cooling structure and the laser active region. In the latter case, the leakage currents of one of these structures (cooling QS or laser active region) can function as operating currents for another structure.

6. Conclusions. A new mechanism of current-induced cooling of semiconducting heterostructures is suggested in this work. This mechanism is different from the Peltier effect [2], because the cooling temperature in our case is independent of the difference in the kinetic coefficients and is determined only by the difference in the size-quantization energies of charge carriers in the first and second QWs.

With an increase in temperature, the tunneling and radiative recombination rates also increase. As a result, the cooling efficiency increases.

The suggested cooling mechanism can be effectively used in optoelectronics in devising light emitting diodes and high-power semiconductor lasers [11]. This mechanism can also be used in devising semiconductor nanorefrigerators. Compared to the existing Peltier microrefrigerators which are actively used for the temperature stabilization of semiconductor lasers, nanorefrigerators have a number of advantages. First, the cooling and the temperature stabilization do not require additional expenditure of energy, because the cooling is accounted for by the injection or leakage current. Second, a nanorefrigerator is considerably smaller in size and directly cools the active region of an optoelectronic device.

Let us briefly discuss the influence of many-particle charge-carrier relaxation processes on the current-induced cooling of quantum systems. On the one hand, these processes increase the probability of charge-carrier radiative recombination and tunneling. On the other hand, the Auger recombination processes and the screening of electron–phonon interaction become significant at high carrier concentrations [12]. Although both these processes preclude QS cooling, many-particle relaxation has no qualitative effect on the current-induced cooling of quantum systems.

REFERENCES

1. L. Cheng and K. Plog, *Molecular Beam Epitaxy and Heterostructures* (M. Nijhoff, Dordrecht, 1985).

2. A. A. Abrikosov, *Fundamentals of the Theory of Metals* (Nauka, Moscow, 1987; North-Holland, Amsterdam, 1988).

3. L. Keldysh, Zh. Éksp. Teor. Fiz. **34**, 962 (1958) [Sov. Phys. JETP **7**, 665 (1958)].

4. V. F. Gantmakher and B. I. Levinson, *Carrier Scattering in Metals and Semiconductors* (Nauka, Moscow, 1984; North-Hooland, New York, 1987).

5. B. K. Ridley, J. Phys. C **15**, 5899 (1982).

6. L. D. Landau and E. M. Lifshitz, *Course of Theoretical Physics*, Vol. 3: *Quantum Mechanics: Non-Relativistic Theory* (Nauka, Moscow, 1982; Pergamon, New York, 1977).

7. A. I. Anselm, *Introduction to Semiconductor Theory* (Nauka, Moscow, 1978; Prentice-Hall, Englewood Cliffs, 1981).

8. *Quantum Well Lasers*, Ed. by P. S. Zory, Jr. (Academic, Boston, 1983).

9. G. G. Zegrya, A. D. Andreev, *et al.*, Proc. SPIE **2399**, 307 (1995).

10. L. M. Asryan, N. A. Gun'ko, A. S. Polkovnikov, *et al.*, Semicond. Sci. Technol. **15** (12), 1131 (2000).

11. E. B. Dogonkin and G. G. Zegrya, submitted to Electron. Lett. (2001).

12. A. S. Polkovnikov and G. G. Zegrya, Phys. Rev. B **58**, 4039 (1998).

Translated by V. Sakun

Charged Two-Dimensional Magnetoexciton and Two-Mode Squeezed Vacuum States[1]

A. B. Dzyubenko[2]

Department of Physics, University at Buffalo, SUNY, Buffalo, NY 14260, USA

Received August 8, 2001

A novel unitary transformation of the Hamiltonian that allows one to partially separate the center-of-mass motion for charged electron–hole systems in a magnetic field is presented. The two-mode squeezed oscillator states that appear at the intermediate stage of the transformation are used for constructing a trial wave function of a two-dimensional charged magnetoexciton. © *2001 MAIK "Nauka/Interperiodica".*

PACS numbers: 71.35.Ji; 73.20.Mf; 73.43.Lp

A problem of center-of-mass (CM) separation for a quantum-mechanical system of charged interacting particles in a magnetic field B was studied by many authors [1–5]. When a charge-to-mass ratio is the same for all particles, the CM and internal motions decouple [2–4] in B. For a neutral system, the CM coordinates can be separated [1, 2] in the Schrödinger equation. This is associated with the fact that translations commute for a neutral system in B. In general, only a partial separation of the CM in magnetic fields is possible [2, 4, 5]. In this letter, we propose a novel operator approach for performing such a separation in charged electron–hole (e–h) systems in B. This approach can be useful for studying in strong magnetic fields, e.g., atomic ions with not-too-large mass ratios [4] and charged excitations in two-dimensional (2D) electron systems, in particular, in the fractional quantum Hall effect regime in planar geometry [6, 7]. In this work, we study in 2D a three-particle problem of two electrons and one hole in a strong magnetic field, i.e., a negatively charged magnetoexciton X^- (see [5, 8, 9] and references therein). We consider an approximate X^- ground state in the form which is related to the two-mode squeezed [10] oscillator vacuum states.

The Hamiltonian describing the 2D three-particle $2e$–h complex in a perpendicular magnetic field B is $H = H_0 + H_{\text{int}}$, where the free-particle part is given by

$$H_0 = \sum_{i=1,2} \frac{\hat{\mathbf{\Pi}}_{ei}^2}{2m_e} + \frac{\hat{\mathbf{\Pi}}_h^2}{2m_h} \equiv \sum_{i=1,2} H_{0e}(\mathbf{r}_i) + H_{0h}(\mathbf{r}_h), \quad (1)$$

and $\hat{\mathbf{\Pi}}_j = -i\hbar\nabla_j - \dfrac{e_j}{c}\mathbf{A}(\mathbf{r}_j)$ are kinematic momentum operators. The interaction Hamiltonian $H_{\text{int}} = H_{ee} + H_{eh}$ is

$$H_{ee} = \frac{e^2}{\epsilon|\mathbf{r}_1 - \mathbf{r}_2|}, \quad H_{eh} = -\sum_{i=1,2} \frac{e^2}{\epsilon|\mathbf{r}_i - \mathbf{r}_h|}. \quad (2)$$

The Hamiltonian H commutes [2, 4, 9] with the operator of magnetic translations (MT) $\hat{\mathbf{K}} = \sum_j \hat{\mathbf{K}}_j$, where $\hat{\mathbf{K}}_j = \hat{\mathbf{\Pi}}_j - \dfrac{e_j}{c}\mathbf{r}_j \times \mathbf{B}$. In the symmetric gauge, $\mathbf{A} = \dfrac{1}{2}\mathbf{B} \times \mathbf{r}$, the operators satisfy the relation $\hat{\mathbf{K}}_j(\mathbf{B}) = \hat{\mathbf{\Pi}}_j(-\mathbf{B})$; independent of the gauge, $\hat{\mathbf{K}}_j$ and $\hat{\mathbf{\Pi}}_j$ commute. The important feature of $\hat{\mathbf{K}}$ and $\hat{\mathbf{\Pi}} = \sum_j \hat{\mathbf{\Pi}}_j$ is the noncommutativity of the components in B: $[\hat{K}_x, \hat{K}_y] = -[\hat{\Pi}_x, \hat{\Pi}_y] = -i\dfrac{\hbar B}{c}Q$, where $Q = \sum_j e_j$ is the total charge. This allows one to introduce the raising and the lowering Bose ladder operators for the whole system [2, 4, 9]

$$\hat{k}_\pm = \pm\frac{i}{\sqrt{2}}(\hat{k}_x \pm i\hat{k}_y), \quad [\hat{k}_+, \hat{k}_-] = -\frac{Q}{|Q|}, \quad (3)$$

$$\hat{\pi}_\pm = \mp\frac{i}{\sqrt{2}}(\hat{\pi}_x \pm i\hat{\pi}_y), \quad [\hat{\pi}_+, \hat{\pi}_-] = \frac{Q}{|Q|}, \quad (4)$$

where $\hat{\mathbf{k}} = \sqrt{c/\hbar B|Q|}\,\hat{\mathbf{K}}$, $\hat{\boldsymbol{\pi}} = \sqrt{c/\hbar B|Q|}\,\hat{\mathbf{\Pi}}$, and the phases of the operators (3) and (4) can be chosen arbitrary. The operator $\hat{\mathbf{k}}^2$ has the discrete oscillator eigenvalues $2k + 1$, $k = 0, 1, \ldots$, which are associated [2, 4]

---

with the guiding center of a charged complex in B. The values of k can be used,[3] together with the total angular momentum projection M_z and the electron, S_e, and hole, S_h, spin quantum numbers, for the classification of states [9]; the exact eigenenergies are degenerate [2, 4] in k.

In terms of the *single-particle* Bose ladder intra-Landau level (LL) operators [5, 6] $B_e^\dagger(\mathbf{r}_j) = -i\sqrt{c/2\hbar Be}(\hat{K}_{jx} - i\hat{K}_{jy})$ for the electrons and $B_h^\dagger(\mathbf{r}_h) = -i\sqrt{c/2\hbar Be}(\hat{K}_{hx} + i\hat{K}_{hy})$ for the hole, the raising operator takes the form $\hat{k}_- = B_e^\dagger(\mathbf{r}_1) + B_e^\dagger(\mathbf{r}_2) - B_h(\mathbf{r}_h)$. One needs to diagonalize $\hat{k}_-$ in order to maintain the exact MT symmetry. This can be achieved by performing first an orthogonal transformation [3, 4] of the electron coordinates $\{\mathbf{r}_1, \mathbf{r}_2, \mathbf{r}_h\} \longrightarrow \{\mathbf{r}, \mathbf{R}, \mathbf{r}_h\}$, where $\mathbf{r} = (\mathbf{r}_1 - \mathbf{r}_2)/\sqrt{2}$ and $\mathbf{R} = (\mathbf{r}_1 + \mathbf{r}_2)/\sqrt{2}$ are the electron relative and CM coordinates. In these coordinates, $\hat{k}_- = \sqrt{2}B_e^\dagger(\mathbf{R}) - B_h(\mathbf{r}_h)$ and can be considered to be a new Bose ladder operator generated by the Bogoliubov transformation [5]

$$\tilde{B}_e^\dagger(\mathbf{R}) = uB_e^\dagger(\mathbf{R}) - vB_h(\mathbf{r}_h) = \tilde{S}B_e^\dagger(\mathbf{R})\tilde{S}^\dagger, \qquad (5)$$

where the unitary operator [5, 6, 10] $\tilde{S} = \exp(\Theta\tilde{\mathcal{L}})$ and the generator $\tilde{\mathcal{L}} = B_h^\dagger(\mathbf{r}_h)B_e^\dagger(\mathbf{R}) - B_e(\mathbf{R})B_h(\mathbf{r})$. Here, Θ is the transformation angle and $u = \cosh\Theta = \sqrt{2}$, $v = \sinh\Theta = 1$. Now we have $\hat{k}_- = \tilde{B}_e^\dagger$ and $\hat{\mathbf{k}}^2 = 2\tilde{B}_e^\dagger\tilde{B}_e + 1$. The second linearly independent creation operator is

$$\tilde{B}_h^\dagger(\mathbf{r}_h) = \tilde{S}B_h^\dagger(\mathbf{r}_h)\tilde{S}^\dagger = uB_h^\dagger(\mathbf{r}_h) - vB_e(\mathbf{R}). \qquad (6)$$

A complete orthonormal basis compatible with both axial and translational symmetries can be constructed [5] as

$$\frac{A_e^\dagger(\mathbf{r})^{n_r}A_e^\dagger(\mathbf{R})^{n_R}A_h^\dagger(\mathbf{r}_h)^{n_h}\tilde{B}_e^\dagger(\mathbf{R})^k\tilde{B}_h^\dagger(\mathbf{r}_h)^lB_e^\dagger(\mathbf{r})^m\tilde{|0\rangle}}{(n_r!n_R!n_h!k!l!m!)^{1/2}} \qquad (7)$$
$$\equiv |n_rn_Rn_h; \widetilde{klm}\rangle.$$

Here, the inter-LL Bose ladder operators are given by $A_e^\dagger(\mathbf{r}_j) = -i\sqrt{c/2\hbar Be}(\hat{\Pi}_{jx} + i\hat{\Pi}_{jy})$ and $A_h^\dagger(\mathbf{r}_h) = -i\sqrt{c/2\hbar Be}(\hat{\Pi}_{hx} - i\hat{\Pi}_{hy})$; the explicit form is given in, e.g., [5, 6]. The tilde sign shows that the transformed

---

[3] Note that the operators $\hat{\pi}_\pm$ do not commute and, in general, do not form a simple algebra with the Hamiltonian. A special case is when the charge-to-mass ratio $e_j/m_j = $ const, and $[H, \hat{\pi}_\pm] = \mp\hbar(e_jB/m_jc)\hat{\pi}_\pm$, which corresponds to the CM separation.

JETP LETTERS   Vol. 74   No. 6   2001

vacuum state $\tilde{|0\rangle}$ (see below) and the transformed operators (5) and (6) are involved. In Eq. (7), the oscillator quantum number is fixed and equals k, while $M_z = n_r + n_R - n_h - k + l - m$. The permutational symmetry requires that $n_r - m$ should be even (odd) for electron spin singlet $S_e = 0$ (triplet $S_e = 1$) states; see [5] for more detail.

The transformation introduces a new vacuum state $\tilde{|0\rangle} = \tilde{S}|0\rangle$, for which, using the normal-ordered form [5, 6, 10] of $\tilde{S}$, one obtains

$$\tilde{|0\rangle} = \tilde{S}|0\rangle = \frac{1}{\cosh\Theta}\exp[\tanh\Theta B_h^\dagger(\mathbf{r}_h)B_e^\dagger(\mathbf{R})]|0\rangle. \quad (8)$$

The coordinate representation has the form

$$\langle\mathbf{r}\mathbf{R}\mathbf{r}_h|\tilde{0}\rangle = \frac{1}{\sqrt{2}(2\pi l_B^2)^{3/2}}$$
$$\times \exp\left(-\frac{\mathbf{r}^2 + \mathbf{R}^2 + \mathbf{r}_h^2 - \sqrt{2}Z^*z_h}{4l_B^2}\right), \qquad (9)$$

where $l_B = (\hbar c/eB)^{1/2}$ is the magnetic length, $Z^* = X - iY$, and $z_h = x_h + iy_h$. Equation (9) shows that $\tilde{|0\rangle}$ contains a *coherent superposition* of an infinite number of e and h states in zero LLs. In the terminology of quantum optics [10], $\tilde{|0\rangle}$ is a *two-mode squeezed state*; for particles in a magnetic field, the squeezing has a direct geometrical meaning (for studies on single-particle coherent and squeezed states in magnetic fields, see [11] and references therein). Indeed, the probability distribution function takes the factored form

$$\left|\langle\mathbf{r}\mathbf{R}\mathbf{r}_h|\tilde{0}\rangle\right|^2 = \frac{1}{2\pi l_B^2}\exp\left(-\frac{\mathbf{r}^2}{2l_B^2}\right)$$
$$\times\frac{2 + \sqrt{2}}{4\pi l_B^2}\exp\left[-\frac{2 + \sqrt{2}}{8l_B^2}(\mathbf{R} - \mathbf{r}_h)^2\right] \qquad (10)$$
$$\times\frac{2 - \sqrt{2}}{4\pi l_B^2}\exp\left[-\frac{2 - \sqrt{2}}{8l_B^2}(\mathbf{R} + \mathbf{r}_h)^2\right].$$

This shows that the distribution for the relative coordinate $\mathbf{R} - \mathbf{r}_h$ is squeezed *at the expense* of that for the coordinate $\mathbf{R} + \mathbf{r}_h$, and the variances are $\langle\tilde{0}|(\mathbf{R} \pm \mathbf{r}_h)^2|\tilde{0}\rangle = 4(2 \pm \sqrt{2})l_B^2$. The squeezing enhances the e–h attraction, which will be used below for constructing a trial wave function of the 2D magnetoexciton X^-.

Let us now perform the second unitary transformation corresponding to the diagonalization of the operator $\hat{\pi}_+ = A_e^\dagger(\mathbf{r}_1) + A_e^\dagger(\mathbf{r}_2) - A_h(\mathbf{r}_h)$. This introduces a

new state $|\bar{0}\rangle = \bar{S}\,\tilde{S}|0\rangle = \bar{S}\,|\tilde{0}\rangle$, which corresponds to the simultaneous diagonalization of the operators $\hat{k}_-$ and $\hat{\pi}_+$; the unitary operator $\bar{S} = \exp(\Theta\overline{\mathcal{L}})$, where the generator $\overline{\mathcal{L}} = A_h^\dagger(\mathbf{r}_h)A_e^\dagger(\mathbf{R}) - A_e(\mathbf{R})A_h(\mathbf{r}_h)$. The transformations effectively introduce new coordinates, $\{\mathbf{r}, \mathbf{R}, \mathbf{r}_h\} \longrightarrow \{\mathbf{r}, \boldsymbol{\rho}_1, \boldsymbol{\rho}_2\}$, where $\boldsymbol{\rho}_1 = \sqrt{2}\,\mathbf{R} - \mathbf{r}_h$ and $\boldsymbol{\rho}_2 = \sqrt{2}\,\mathbf{r}_h - \mathbf{R}$, which can be presented in the matrix form

$$\begin{pmatrix} \boldsymbol{\rho}_1 \\ \boldsymbol{\rho}_2 \end{pmatrix} = \hat{F}\begin{pmatrix} \mathbf{R} \\ \mathbf{r}_h \end{pmatrix}, \quad \hat{F} = \begin{pmatrix} \cosh\Theta & -\sinh\Theta \\ -\sinh\Theta & \cosh\Theta \end{pmatrix}, \quad (11)$$

with $\cosh\Theta = \sqrt{2}$, $\sinh\Theta = 1$; the matrix $\hat{F}$ corresponds to the $SU(1, 1)$ symmetry [10]. Indeed, the inter-LL ladder operators are changed under the Bogoliubov transformations as

$$\bar{S}\begin{pmatrix} A_e^\dagger(\mathbf{R}) \\ A_h(\mathbf{r}_h) \end{pmatrix}\bar{S}^\dagger = \hat{F}\begin{pmatrix} A_e^\dagger(\mathbf{R}) \\ A_h(\mathbf{r}_h) \end{pmatrix} = \begin{pmatrix} A_e^\dagger(\boldsymbol{\rho}_1) \\ A_h(\boldsymbol{\rho}_2) \end{pmatrix}. \quad (12)$$

The intra-LL operators (5) and (6) transform according to the same representation. The coordinate representation

$$\langle \mathbf{r}\boldsymbol{\rho}_1\boldsymbol{\rho}_2|\bar{0}\rangle = \frac{1}{(2\pi l_B^2)^{3/2}}\exp\left(-\frac{\mathbf{r}^2 + \boldsymbol{\rho}_1^2 + \boldsymbol{\rho}_2^2}{4l_B^2}\right) \quad (13)$$

shows that $|\bar{0}\rangle$ is a *true vacuum* for both the intra-LL $B_e^\dagger(\boldsymbol{\rho}_1)$, $B_h^\dagger(\boldsymbol{\rho}_2)$ and the inter-LL $A_h^\dagger(\boldsymbol{\rho}_2)$, $A_e^\dagger(\boldsymbol{\rho}_1)$ operators. Now, we can perform the change of the variables $\{\mathbf{r}, \mathbf{R}, \mathbf{r}_h\} \longrightarrow \{\mathbf{r}, \boldsymbol{\rho}_1, \boldsymbol{\rho}_2\}$ in the basis states:

$$|n_r n_R n_h; \widetilde{klm}\rangle$$

$$= \frac{\bar{S}^\dagger A_e^\dagger(\mathbf{r})^{n_r} A_e^\dagger(\boldsymbol{\rho}_1)^{n_R} A_h^\dagger(\boldsymbol{\rho}_2)^{n_h} B_e^\dagger(\boldsymbol{\rho}_1)^k B_h^\dagger(\boldsymbol{\rho}_2)^l B_e^\dagger(\mathbf{r})^m|\bar{0}\rangle}{(n_r!\,n_R!\,n_h!\,k!\,l!\,m!)^{1/2}}$$

$$\equiv \bar{S}^\dagger|\overline{n_r n_R n_h; klm}\rangle. \quad (14)$$

The overline shows that a state is generated in the usual way by the intra- and inter-LL Bose ladder operators acting on the true vacuum $|\bar{0}\rangle$, all in the representation of the coordinates $\{\mathbf{r}, \boldsymbol{\rho}_1, \boldsymbol{\rho}_2\}$. The Hamiltonian H is block-diagonal in the quantum numbers k, M_z (and S_e, S_h). Due to the Landau degeneracy [2, 9] in k, it is sufficient to consider the states with $k = 0$. This effectively removes one degree of freedom and corresponds to a partial separation of the CM motion. From now on, we will consider the $k = 0$ states only, designating such

states in Eq. (14) as $|n_r n_R n_h; \widetilde{lm}\rangle$. For the Hamiltonian, we arrive therefore at the unitary transformation

$$\langle \widetilde{m_2 l_2}; n_{h2}n_{R2}n_{r2}|H|n_{r1}n_{R1}n_{h1}; \widetilde{l_1 m_1}\rangle$$
$$= \langle \overline{m_2 l_2; n_{h2}n_{R2}n_{r2}}|\bar{S}H\bar{S}^\dagger|\overline{n_{r1}n_{R1}n_{h1}; l_1 m_1}\rangle, \quad (15)$$

which is the main formal result of this work.

The Coulomb interparticle interactions (2) in the coordinates $\{\mathbf{r}, \boldsymbol{\rho}_1, \boldsymbol{\rho}_2\}$ take the form

$$H_{ee} = \frac{e^2}{\sqrt{2}\epsilon r}, \quad H_{eh} = -\frac{\sqrt{2}e^2}{\epsilon|\boldsymbol{\rho}_2 - \mathbf{r}|} - \frac{\sqrt{2}e^2}{\epsilon|\boldsymbol{\rho}_2 + \mathbf{r}|}, \quad (16)$$

and H_{int} *does not depend* on $\boldsymbol{\rho}_1$. From Eq. (12), it follows that the free Hamiltonians transform as $\bar{S}H_{0e}(\mathbf{r})\bar{S}^\dagger = H_{0e}(\mathbf{r})$, $\bar{S}H_{0e}(\mathbf{R})\bar{S}^\dagger = H_{0e}(\boldsymbol{\rho}_1)$, and $\bar{S}H_{0h}(\mathbf{r}_h)\bar{S}^\dagger = H_{0h}(\boldsymbol{\rho}_2)$ and describe *new effective particles*—free e and h in a magnetic field—with the *modified interactions* (16). The Hamiltonian of the e–e interactions $H_{ee}(\sqrt{2}|\mathbf{r}|)$ does not depend on $\boldsymbol{\rho}_1$, $\boldsymbol{\rho}_2$ and, therefore, is invariant: $\bar{S}H_{ee}\bar{S}^\dagger = H_{ee}$. Thus, the matrix elements of the e–e interaction are easily obtained from Eq. (15): they reduce to the matrix elements $V_{n_1 m_1}^{n_1' m_1'}$ describing the interaction of the electron with a fixed negative charge $-e$:

$$\langle \widetilde{m_2 l_2}; n_{h2}n_{R2}n_{r2}|H_{ee}|n_{r1}n_{R1}n_{h1}; \widetilde{l_1 m_1}\rangle$$
$$= \langle \overline{m_2 l_2; n_{h2}n_{R2}n_{r2}}|H_{ee}|\overline{n_{r1}n_{R1}n_{h1}; l_1 m_1}\rangle \quad (17)$$
$$= \delta_{n_{R1}, n_{R2}}\delta_{n_{h1}, n_{h2}}\delta_{l_1, l_2}\delta_{n_{r1} - m_1, n_{r2} - m_2}\frac{1}{\sqrt{2}}V_{n_{r1}m_1}^{n_{r2}m_2}.$$

In, e.g., zero [5] LL, $V_{0m}^{0m} = [(2m - 1)!!/2^m m!]E_0$, where $E_0 = \sqrt{\pi/2}\,(e^2/\epsilon l_B)$. The generator $\overline{\mathcal{L}}$ and the Hamiltonian $H_{eh}(\mathbf{r}, \boldsymbol{\rho}_2)$ do not form a closed algebra of a finite order. Therefore, the explicit form of $\bar{S}H_{eh}\bar{S}^\dagger$ cannot be found. We can find, however, the form of the matrix elements of $\bar{S}H_{eh}\bar{S}^\dagger$ in Eq. (15). Because of the electron permutational symmetry $\mathbf{r} \longleftrightarrow -\mathbf{r}$, it is sufficient to consider the term $U_{eh}(\boldsymbol{\rho}_2 - \mathbf{r}) = -e^2/\epsilon|\boldsymbol{\rho}_2 - \mathbf{r}|$. Here, we only consider the states in zero LL $|\overline{000; lm}\rangle \equiv |\overline{lm}\rangle$. Using the normal-ordered form of $\bar{S}$, we have

$$\langle \overline{m_2 l_2}|\bar{S}U_{eh}\bar{S}^\dagger|\overline{l_1 m_1}\rangle \equiv \bar{U}_{0m_1 0l_1}^{0m_2 0l_2}$$
$$= \frac{1}{2}\langle \overline{m_2 l_2}|\exp\left\{-\frac{1}{\sqrt{2}}A_e(\boldsymbol{\rho}_1)A_h(\boldsymbol{\rho}_2)\right\}U_{eh} \quad (18)$$
$$\times \exp\left\{-\frac{1}{\sqrt{2}}A_h^\dagger(\boldsymbol{\rho}_2)A_e^\dagger(\boldsymbol{\rho}_1)\right\}|\overline{l_1 m_1}\rangle.$$

Expanding the exponents and exploiting the fact that $U_{eh}(\boldsymbol{\rho}_2 - \mathbf{r})$ does not depend on $\boldsymbol{\rho}_1$, we obtain a series

$$\overline{U}^{0m_2 0 l_2}_{0 m_1 0 l_1} = \frac{1}{2} \sum_{p=0}^{\infty} \left(\frac{1}{2}\right)^p U^{0 m_2 p l_2}_{0 m_1 p l_1}. \tag{19}$$

Note that Eq. (19) includes contributions of the *infinitely many* LLs. For the Coulomb interactions, the matrix elements can be calculated analytically; in zero LL, we obtain

$$\left\langle \overline{m_2 l_2} \left| \bar{S} H_{\mathrm{eh}} \bar{S}^\dagger \right| \overline{l_1 m_1} \right\rangle \tag{20}$$
$$= \delta_{l_1 - m_1, \, l_2 - m_2} 2\sqrt{2} \, \overline{U}_{\min(m_1, m_2), \, \min(l_1, l_2)}(|m_1 - m_2|),$$

$$\overline{U}_{mn}(s) = -\frac{E_0}{[m!(m+s)!n!(n+s)!]^{1/2} 2^{m+n+s} 3^{s+1/2}}$$

$$\times \sum_{k=0}^{m} \sum_{l=0}^{n} C_m^k C_n^l \left(\frac{2}{3}\right)^{k+l} [2(k+l+s)-1]!! [2(m-k)-1]!! \tag{21}$$

$$\times \sum_{p=0}^{n-l} C_k^p C_{n-l}^p (-1)^p p! [2(n-l-p)-1]!!.$$

The developed formalism can be used for performing a rapidly convergent [5] expansion of the interacting e–h states in the basis (15), which preserves all symmetries of the problem. Here we demonstrate a possibility of using the squeezed states for constructing *trial* wave functions. We consider the triplet charged 2D magnetoexciton in zero LL, X^-_{t00}, with $M_z = -1$, which is the only bound state [8, 9] in zero LL in the strictly 2D system in the high-field limit. The *simplest possible* wave function in zero LL compatible with *all* symmetries of the problem is

$$\langle \mathbf{r} \mathbf{R} \mathbf{r}_h | B_e^\dagger(\mathbf{r}) | \tilde{0}\rangle = \frac{1}{\sqrt{2}(2\pi l_B^2)^{3/2}} \left(\frac{z^*}{\sqrt{2} l_B}\right)$$

$$\times \exp\left(-\frac{\mathbf{r}^2 + \mathbf{R}^2 + \mathbf{r}_h^2 - \sqrt{2} Z^* z_h}{4 l_B^2}\right). \tag{22}$$

This form allows analytic calculations and, as a squeezed state (see above), already ensures the X^-_{t00} binding. Indeed, the total Coulomb interaction energy is given by

$$\frac{1}{\sqrt{2}} V^{01}_{01} + 2\sqrt{2} \, \overline{U}_{10}(0) = \left(\frac{\sqrt{2}}{4} - \frac{5\sqrt{6}}{9}\right) E_0 \simeq -1.007 E_0.$$

The corresponding binding energy (counted from the ground-state energy of the neutral magnetoexciton, $-E_0$) is $0.007 E_0$, which is 17% of the numerically "exact" value of $0.043 E_0$ [8, 5]. A similar type of squeezing can be applied to construct a trial wave function of the X^-_{t00}. The idea is to additionally squeeze the
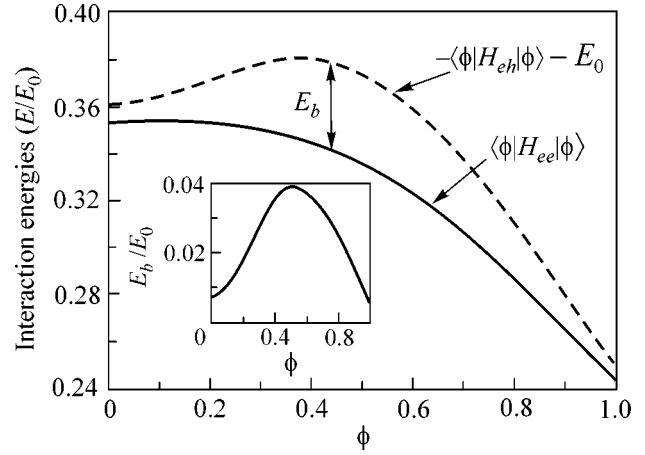
The expectation values of the e–e repulsion, $\langle\phi|H_{ee}|\phi\rangle$, and the e–h attraction, $\langle\phi|H_{eh}|\phi\rangle$ (with the opposite sign, counted from the neutral magnetoexciton binding energy $E_0 = \sqrt{\pi/2} \, (e^2/\epsilon l_B)$), for the trial wave function (23) of the charged triplet magnetoexciton in zero LLs, X^-_{t00}. The binding energy $E_b = -\langle\phi|H_{eh} + H_{ee}|\phi\rangle + E_0$ is shown in the inset.

effective hole $\boldsymbol{\rho}_2$ and electron $\mathbf{r}$ coordinates. Since the wave function must be antisymmetric under the permutation of the electron coordinates, we can use the form $|\phi\rangle \sim B_e^\dagger(\mathbf{r})(S_\phi + S_{-\phi}) \bar{S}^\dagger |\tilde{0}\rangle$, where the second two-mode squeezing operator is given by $S_\phi = \exp[\phi B_e^\dagger(\mathbf{r}) B_h^\dagger(\boldsymbol{\rho}_2) - \text{H.c.}]$ and we have used $|\tilde{0}\rangle = \bar{S}^\dagger|0\rangle$. The normalized *four*-mode squeezed wave function has the form

$$|\phi\rangle = \frac{1 + \tanh^2\phi}{\cosh^2\phi \sqrt{1 + \tanh^4\phi}} B_e^\dagger(\mathbf{r}) \tag{23}$$
$$\times \cosh[\tanh\phi \, B_e^\dagger(\mathbf{r}) B_h^\dagger(\boldsymbol{\rho}_2)] \bar{S}^\dagger |0\rangle.$$

The calculated energy of the Coulomb e–e repulsion, $\langle\phi|H_{ee}|\phi\rangle$, monotonically decreases with increasing transformation angle ϕ, whereas the energy of the e–h attraction, $-\langle\phi|H_{ee}|\phi\rangle$, has a maximum (see figure). The binding of the X^-_{t00} results from a rather delicate balance between the two terms, and for the state (23) the maximum achieved binding energy is $E_b \simeq 0.038 E_0$ (see inset in figure), which is 91% of the "exact" value [5, 8]; note that the inaccuracy is 0.3% of the e–h interaction energy. A similar type of squeezed trial wave functions may be useful in other solid state and atomic physics problems dealing with correlated e–h states in strong magnetic fields.

In conclusion, we have developed for charged e–h systems in magnetic fields an operator approach that allows one to partially separate the CM motion. This results in the appearance of new effective particles, electrons and holes in a magnetic field, with modified

interparticle interactions. A relation of the considered basis states to the two-mode squeezed oscillator states has been established.

REFERENCES

1. L. P. Gor'kov and I. E. Dzyaloshinskiĭ, Zh. Éksp. Teor. Fiz. **53**, 717 (1967) [Sov. Phys. JETP **26**, 449 (1968)].

2. J. E. Avron, I. W. Herbst, and B. Simon, Ann. Phys. (N.Y.) **114**, 431 (1978).

3. Yu. A. Bychkov, S. V. Iordanskiĭ, and G. M. Eliashberg, Pis'ma Zh. Éksp. Teor. Fiz. **33**, 152 (1981) [JETP Lett. **33**, 143 (1981)].

4. B. R. Johnson, J. O. Hirschfelder, and K. H. Yang, Rev. Mod. Phys. **55**, 109 (1983).

5. A. B. Dzyubenko, Solid State Commun. **113**, 683 (2000).

6. Z. F. Ezawa, *Quantum Hall Effects* (World Scientific, Singapore, 2000).

7. V. Pasquier, Phys. Lett. B **490**, 258 (2000).

8. J. J. Palacios, D. Yoshioka, and A. H. MacDonald, Phys. Rev. B **54**, R2296 (1996).

9. A. B. Dzyubenko and A. Yu. Sivachenko, Phys. Rev. Lett. **84**, 4429 (2000).

10. J. R. Clauder and B.-S. Skagerstam, *Coherent States* (World Scientific, Singapore, 1985).

11. I. A. Malkin and V. I. Man'ko, Zh. Éksp. Teor. Fiz. **55**, 1014 (1968) [Sov. Phys. JETP **28**, 527 (1969)]; A. Feldman and A. H. Kahn, Phys. Rev. B **1**, 4584 (1970); E. I. Rashba, L. E. Zhukov, and A. L. Efros, Phys. Rev. B **55**, 5306 (1997); M. Ozana and A. L. Shelankov, Fiz. Tverd. Tela (St. Petersburg) **40**, 1405 (1998) [Phys. Solid State **40**, 1276 (1998)].

π–0 Transition in Superconductor-Ferromagnet-Superconductor Junctions[1]

N. M. Chtchelkatchev[1]*, W. Belzig[2], Yu. V. Nazarov[3], and C. Bruder[2]

[1] *Landau Institute for Theoretical Physics, Russian Academy of Sciences, ul. Kosygina 2, Moscow, 117940 Russia*

*e-mail: nms@landau.ac.ru

[2] *Departement Physik und Astronomie, Universität Basel, 4056 Basel, Switzerland*

[3] *Department of Applied Physics and Delft Institute of Microelectronics and Submicrontechnology, Delft University of Technology, 2628 CJ Delft, The Netherlands*

Superconductor–ferromagnet–superconductor (SFS) Josephson junctions are known to exhibit a transition between π and 0 states. In this letter, we find the π–0 phase diagram of an SFS junction depending on the transparency of an intermediate insulating layer (I). We show that, in general, the Josephson critical current is nonzero at the π–0 transition temperature. Contributions to the current from the two spin channels nearly compensate each other, and the first harmonic of the Josephson current as a function of phase difference is suppressed. However, higher harmonics give a nonzero contribution to the supercurrent. © 2001 MAIK "Nauka/Interperiodica".

PACS numbers: 74.50.+r; 74.60.Jg; 74.80.-g

In the last years, many interesting phenomena were investigated in Superconductor (S)–Ferromagnet (F)–Superconductor (SFS) Josephson contacts. One of the most striking effects is the so-called π state of SFS junctions [1–4], in which the equilibrium ground state is characterized by an intrinsic phase difference of π between the two superconductors. Investigations of π junctions have not only academic interest; e.g., in [5, 6] a solid-state implementation of a quantum bit was proposed on the basis of a superconducting loop with 0 and π Josephson junctions.

The existence of the π state in an SFS junction was recently experimentally demonstrated by the group of Ryazanov [4]. In this experiment, the temperature dependence of the critical current was measured. At a certain temperature, the critical current was found to drop almost to zero; this has been interpreted as the transition from the 0 to the π state. The transition temperature $T_{\pi 0}$ was shown to exhibit a strong dependence on the concentration of ferromagnetic impurities, i.e., on the exchange field E_{ex} in the ferromagnetic film.

In this letter, we present a theory of the π–0 transition in short SFS junctions. Our goal is to understand what parameters (exchange field, temperature, etc.) stabilize a π state and what the phase diagram looks like. We investigate the current–phase relation and the critical current near the transition to the π state. Most importantly, we find that, in general, the critical current is nonzero at $T_{\pi 0}$, and it may not even reach a local minimum. The identification of the critical current drop and the π–0 transition is only possible if the current is given by the standard Josephson expression $I(\varphi) \propto \sin(\varphi)$, which is valid for the limiting case of tunnel barriers only. Even if the main contribution to the current is of this form, the higher harmonics contribution $I(\varphi) \propto \sin(2\varphi)$ would not vanish at $T_{\pi 0}$. Consequently, $I_c \neq 0$ at the transition point.

We consider SFS junctions in the "short" limit defined by $\hbar/\tau \gg \Delta(T = 0)$; here, τ is the characteristic time needed for an electron to propagate between the superconductors. In this case, we can employ a powerful scattering formalism [7] which allows one to express the energies of Andreev states in the junction in terms of the transmission amplitudes of the junction in the normal state. These Andreev states give the main contribution to the phase-dependent energy of the junction, and therefore $I(\varphi)$ can be calculated. Any junction is characterized by a set of "transport channels" labeled $n = 0, 1, \ldots, N$, each channel being characterized by the transmission coefficient D_n. If one disregards ferromagnetism, the Andreev levels are degenerate with respect to the spin index σ. Their energies are given by $E_{n\sigma} = \pm\Delta(1 - D_n\sin^2(\varphi/2))^{1/2}$.

We generalize the scattering approach to cover SFS junctions. In this case, the phase of the transmission amplitudes also becomes important. To see this, we

---

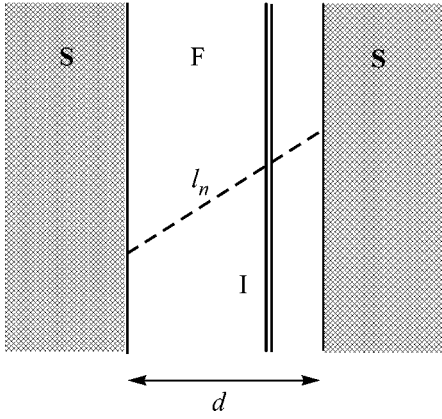[1] This article was submitted by the authors in English.

Fig. 1. Junction configuration. The current flows from one superconductor (S) to the other through the ferromagnetic (F) layer (width d) with a scattering region denoted by I. The exchange field is assumed to be parallel to the SF boundaries.

introduce the parameter γ: $\cos(\gamma(\varphi) \equiv 1 - 2D_n \sin^2(\varphi/2)$. If we assume that ferromagnetism does not change the transport channels, the energies of the Andreev states become

$$E_{n\sigma}(\varphi) = \Delta \left| \cos\left(\frac{\gamma(\varphi) + (\Phi_{n,\sigma} - \Phi_{n,-\sigma})}{2} \right) \right|, \qquad (1)$$

where $\Phi_{n,\sigma}$ is the phase of the transmission amplitude for an electron with spin σ in the channel n. Thus, we observe that the different phase shifts for different spin directions result in a spin-dependent *energy* shift of the Andreev states. To specify the model further, we consider the layout shown in Fig. 1. It consists of two bulk superconductors, a ferromagnetic layer with exchange energy $E_{ex} \ll E_F$, and a scattering region denoted by I. We assume that the F layer is ballistic and that the order parameter Δ is constant in the superconductors $\Delta(x) = \Delta e^{\pm i\varphi/2}$, and $\Delta(x) = 0$ in F.

We believe that the model considered is quite general. It applies to quasiballistic SFS multilayers (recently a quasiballistic SF junction was prepared by Kontos *et al.* [8]) with either specular or disordered interfaces [9]; it also applies to Josephson junctions, where electrons tunnel through small ferromagnetic nanoparticles [10, 11]. We shall restrict ourself to the case where the width of the scattering region is much smaller than the width d of the junction. The transport channels can be associated with different incident angles. Then, $\Phi_{n,\sigma} - \Phi_{n,-\sigma} = \sigma\pi(2E_{ex}d/\pi\hbar v_F)l_n = \sigma\pi\Theta l_n$, where $l_n > 1$ is the length of a quasiparticle path between the superconductors divided by d; see Fig. 1. Equation (1) reproduces the energy spectrum obtained in the limiting case $D = 1$ in [12].

The contribution to the free energy of the junction which depends on φ is given by

$$\Omega(\varphi) = -T \sum_{n,\sigma} \ln\left[\cosh\left(\frac{E_{n\sigma}(\varphi)}{2T} \right) \right]. \qquad (2)$$

The continuous spectrum is neglected in Eq. (2); one can easily check that it gives a φ-independent contribution to the free energy. The summation over the channels n can be evaluated by converting the sum to an integral: $\sum_n \ldots = \int dl \rho(l)$, where $\rho(l) = \sum_n \delta(l - l_n)$ and $\int \rho(l) dl = N$, the number of channels. If there is only one channel in the junction, the weight function ρ defined above reduces to $\delta(l - 1)$. If, on the other hand, the number of channels N is much bigger than unity, $\rho(l) = 2N/l^3 \theta(l - 1)$. (We assumed D to be independent of n.) A similar distribution of l can be found for SFS junctions with disordered boundaries (see [9]). At some points of these notes, we will use the distribution $\rho(l) = N\delta(l - 1)$, since it allows us to proceed analytically, and the results obtained with it are qualitatively the same as with the other distributions. We will refer to this distribution as the δ distribution. (When $\rho(l) = N\delta(l - 1)$, our parameter Θ is closely related to spin-mixing angle introduced in [11].)

What exchange field in F is sufficient to ensure that the SFS junction can be put into a π phase by changing the temperature? The π state is the result of the ferromagnetic exchange field in the F layer. If it is too small, then the junction will remain in the 0 phase at all temperatures. We show below what values of exchange field and temperature guarantee that the junction will be in the π phase.

In an equilibrium situation with zero current, the temperature $T_{\pi 0}$ separating the π and 0 phases is determined from the condition that the free energy Ω reaches its minimum at $\varphi = 2\pi n$ and at $\varphi = \pi + 2\pi n$, $n = 0, \pm 1, \ldots$ (the free energy of an ordinary junction has a global minimum at $\varphi = 2\pi n$). The numerical solution of this equation for $T_{\pi 0}(D)$ is shown in Fig. 2. Here and below, we use the approximation $\Delta(T)/\Delta(0) = \tanh(1.74\sqrt{T_c/T - 1})$ in doing numerical calculations. If $D = 1$, the π phase can exist only in the domain $2n + 1/2 < \Theta < 3/2 + 2n$, $n = 0, \pm 1, \ldots$. At finite D, there are regions of Θ in which either the π phase or the 0 phase is stable for all temperatures; $I_c(T)$ has no cusps in these regions. For $\Theta \longrightarrow 1/2 + n$, $T_{\pi 0} \longrightarrow T_c$ for arbitrary transparency.

There are regions in the phase diagram where Ω has two minima, $\pi = 2\pi n$ and $\varphi = \pi(2n + 1)$, $n = 0, \pm 1, \ldots$. We will consider these regions below.

The (T, Θ) phase diagram of the junction is depicted in the inset in Fig. 2. The diagram is periodic in Θ with period 2π. It follows from the graph that a large value of the exchange field $\Theta = 2E_{ex}d/\pi\hbar v_F$ does not guarantee that the SFS junction is a π junction.

Evidence of the existence of a π phase in SFS junctions was experimentally demonstrated by the group of Ryazanov [4]. The experimental curves $I_c(T)$ showed cusps at a certain temperature (which we will denote by $T_{\pi 0}$); the critical current at the cusp was close to zero. There are qualitative arguments in [4] that the cusp corresponds to transition of the junction to the π state and $I_c \equiv 0$ at the cusp. We agree with the first statement, but disagree with the second. In our opinion, there is no qualitative argument for the critical current to be zero at the temperature of the cusp. Our model gives $I_c(T)$ curves qualitatively similar to those presented by Ryazanov *et al.*, but $I_c \neq 0$ at the cusp, where the junction undergoes transition between 0 and π states. This will be discussed below in more detail.

The Josephson current I carried by the Andreev levels (1) can be found from the free energy (2) using the relation $I(\varphi) = \dfrac{2e}{\hbar}\partial_\varphi \Omega(\varphi)$. Using $\partial_\varphi \gamma = D\sin(\varphi)/\sin(\gamma)$, we obtain

$$I(\varphi) = \sum_\sigma \sum_n \frac{2e}{\hbar}\frac{D\sin(\varphi)}{\sin(\gamma)}\Delta \sin\left(\frac{\gamma + \sigma\pi\Theta l_n}{2}\right)$$

$$\times \tanh\left(\frac{\Delta}{2T}\cos\left(\frac{\gamma + \sigma\pi\Theta l_n}{2}\right)\right). \qquad (3)$$

If $\Theta = 0$ and $D = 1$, Eq. (3) reduces to the usual formula for the Josephson current in a short ballistic SNS junction, leading to the critical current $I_c = Ne\Delta/\hbar$ at $T = 0$ [7, 13].

If $D \ll 1$, we can proceed analytically in the calculation of $I_c(T)$. Then, $\gamma \approx 2\sqrt{D}\,|\sin(\varphi/2)| \ll 1$ and we can expand the Josephson current (3) in γ. This leads to

$$I(\varphi) = \frac{e\Delta D}{2\hbar}\sin(\varphi)g(\Theta, T), \qquad (4)$$

where

$$g(\Theta, T) = \int dl\rho(l)\Bigg\{\cos(\pi\Theta l/2)\tanh\left(\frac{\cos(\pi\Theta l/2)\Delta}{2T}\right)$$

$$- \frac{\Delta \sin^2(\pi\Theta l/2)}{2T\cosh^2(\cos(\pi\Theta l/2)\Delta/2T)}\Bigg\}. \qquad (5)$$

If $g > 0$ in Eq. (5), the junction is in the ordinary state. In the opposite case, the junction is in the π state.

Solving $g(\Theta, T) = 0$ gives us the transition temperature $T_{\pi 0}$. For $\rho(l) \propto \delta(l-1)$, $g(\Theta, T) = 0$ can be solved only in the domain $2n + 3/2 \leq \Theta \leq 1/2 + 2n$, $n = 0, \pm 1, \ldots$. As a consequence, the π phase exists only in these domains. If $\Theta \longrightarrow 1/2 + n$, then $T \longrightarrow T_c$; $\Theta \longrightarrow 1 + 2n$ leads to $T \longrightarrow 0$.

In the region $|T - T_{\pi 0}| \sim DT_c$, the current is no longer given by Eq. (4). Higher harmonics in φ have to be
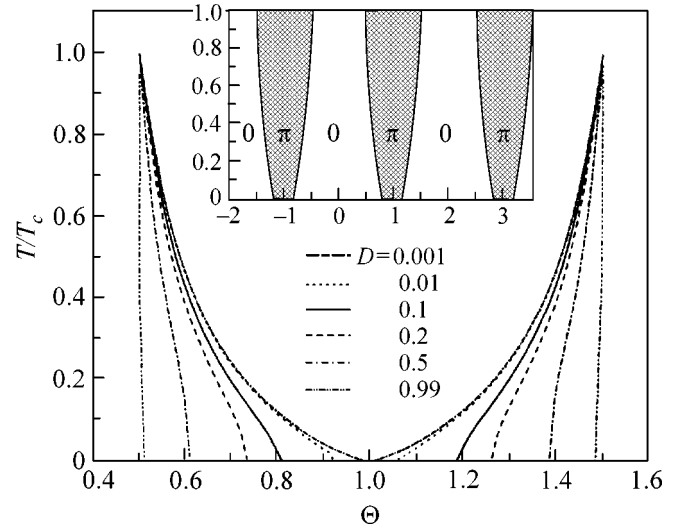
Fig. 2. The temperature of the π–0 transition at zero current versus the dimensionless exchange field $\Theta = 3E_{ex}d/\pi\hbar v_F$ at different values of junction transparencies D. Only trajectories with $l = 1$ are taken into account, which is justified if either one channel or many channels are present. Inset: phase diagram of the junction at $D = 0.1$. The gray regions correspond to the π phase; the white regions, to the 0 phase.

taken into account. Since the nth harmonic is proportional to $D^n \sin(n\varphi)$ [this follows from Eq. (3)] and $D \ll 1$, the second harmonic gives the main contribution to the Josephson current: $I(\varphi) \propto D^2 \sin(2\varphi)$. This means that the critical current is nonzero at the temperature of π–0 transition, $I_c \propto D^2$. Near $T_{\pi 0}$, the currents of the spin channels $\sigma = \pm 1$ flow in opposite directions and nearly compensate each other; therefore, I_c is suppressed.

Near the critical temperature T_c, we also can proceed analytically. Then, we obtain from Eq. (3) for the Josephson current

$$I(\varphi) = \frac{e\Delta^2}{2T\hbar}\sin(\varphi)\int dl\rho(l)D\sin(\pi\Theta l). \qquad (6)$$

Using the δ distribution of the trajectory lengths, we find that the junction is in the π state when $1 + 2n < \Theta < 2 + 2n$, $n = 0, \pm 1, \ldots$.

Figure 3 shows the typical dependence of the critical current on temperature. The critical current in the figure is normalized to the critical current $I_{c0} = N(e\Delta/\hbar)(1 - \sqrt{1-D})$ at zero temperature and zero exchange field. The plot corresponding to $D = 0.22$ exhibits two cusps. When the temperature is low, the junction is in the π state; for intermediate temperatures (between the two cusps), the junction will be in the 0 state, and for $T \lesssim T_c$ again in the π state. [There is a schematic plot in [1] where $I_c(T)$ of an SFS junction has many cusps with nonzero critical current in the cusps. However, [1] does not provide an explanation of this fact.] The critical cur-
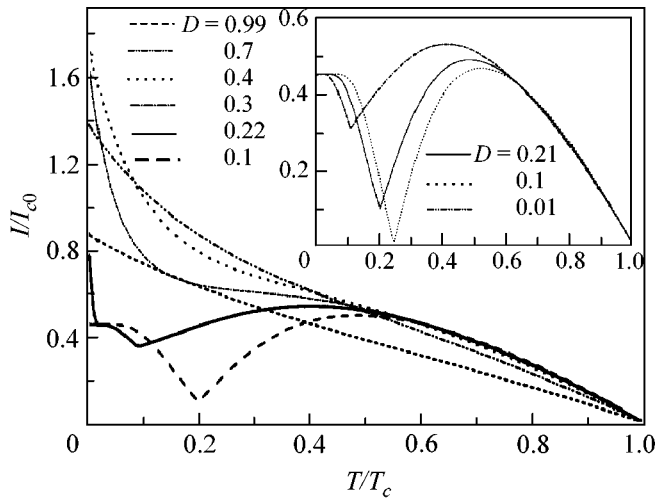
Fig. 3. Dependence of the critical current on temperature for $\Theta = 0.7$ at different transparencies D. Cusps in the $I_c(T)$ curves indicate the π–0 transition. I_c is always nonzero at the cusp; see the inset. The plot of the critical current for $D = 0.22$ has two cusps. At low temperature and $I \lesssim I_c$, the junction with $D = 0.22$ is in the π state; at intermediate temperatures (between two cusps), in the 0 state; and for temperatures near T_c, again in π state.
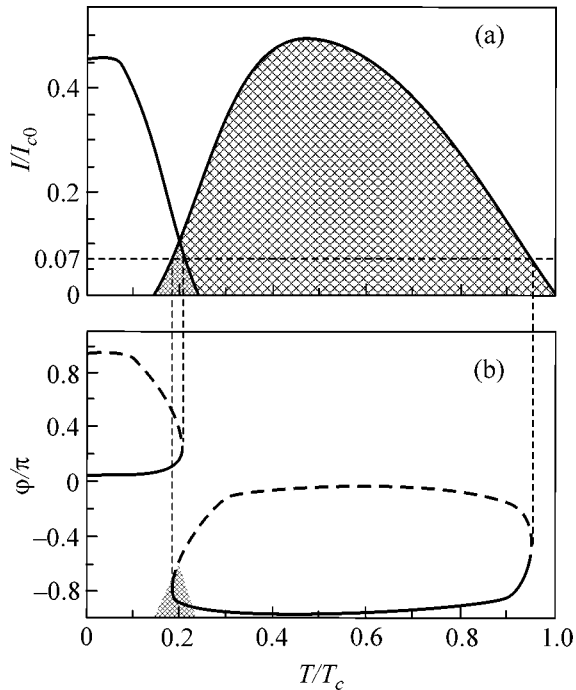

Fig. 4. (a) The phase diagram of the junction for $D = 0.1$, $\Theta = 0.7$. The light gray region corresponds to the π phase; the white, to the 0 phase. The Gibbs potential has two minima of φ in $[-\pi, \pi]$ in the dark gray region. The critical current (solid thick line) is the upper boundary of the phase diagram. (b) Temperature dependence of the phases corresponding to the dc current $I = 0.07 I_{c0}$ [dashed line is parallel to the temperature axes in (a)]. The thick solid line represents the stable solution to the equation $I = I(\varphi)$ (minimum of the Gibbs energy), and the dashed curve exhibits the unstable solution (maximum of the Gibbs energy). The equilibrium transition temperature ($I = 0$) corresponds to $T/T_c = 0.2$.

rent for $D = 0.3, 0.4, 0.7$ in Fig. 3 is greater than the critical current I_{c0} corresponding to zero temperature and zero Θ. The exchange field enhances the Josephson current in the SFS junction [14].

Below, we will investigate the π–0 transition when a dc current $I < I_c$ is injected into the junction. We will pay attention to the regime where I is smaller than I_c at the cusp. Suppose that the temperature is changed at fixed I. Then at the π–0 transition temperature, the phase across the junction will jump approximately by π.

There are several solutions $\varphi(T)$ to the equation $I = I(\varphi)$, where $I(\varphi)$ is given by Eq. (3). We will assume that the damping is large such that the phase is stabilized at one of the minima of the Gibbs energy $\Xi(I, T, \varphi) = \Omega(T, \varphi) - \varphi I \hbar/(2e)$ [15]. The phase values corresponding to the minima of the Gibbs energy are depicted by solid lines in Fig. 4b. If the temperature is increased from $T = 0$, the phase will continuously change with T until T reaches the dark gray region in Fig. 4a, where Ξ has two minima of φ in $[-\pi, \pi]$. Here, the phase will choose one of the minima, depending on the dynamics of the junction, which depends on the properties of the external circuit. Outside of this region at higher temperatures, the phase will also follow continuously adiabatic changes of T.

In conclusion, we have investigated the phase transition between the π and 0 phases in a ballistic SFS junction with a scatterer in the F layer. We calculated the (T, Θ) and (I, T) phase diagrams of the junction. It was shown that there is no reason for the critical current to be zero at the transition temperature $T_{\pi 0}$. The currents of the two spin channels nearly compensate each other at $T_{\pi 0}$, and the current scales as $D^2 \sin(2\varphi)$, $D \ll 1$ instead of $D \sin(\varphi)$, as it does away from the transition.

REFERENCES

1. L. N. Bulaevskii, V. V. Kuzii, and A. A. Sobyanin, Pis'ma Zh. Éksp. Teor. Fiz. **25**, 314 (1977) [JETP Lett. **25**, 290 (1977)].

2. A. V. Andreev, A. I. Buzdin, and R. M. Osgood, Phys. Rev. B **43**, 10124 (1991).

3. A. I. Buzdin, B. Vujicic, and M. Yu. Kupriyanov, Zh. Éksp. Teor. Fiz. **101**, 231 (1992) [Sov. Phys. JETP **74**, 124 (1992)].

4. A. V. Veretennikov, V. V. Ryazanov, V. A. Oboznov, *et al.*, Physica B (Amsterdam) **284-288**, 495 (2000); V. V. Ryazanov, V. A. Oboznov, A. Yu. Rusanov, *et al.*, Phys. Rev.

Lett. **86**, 2427 (2001); V. V. Ryazanov, V. A. Oboznov, A. V. Veretennikov, *et al.*, cond-mat/0103240.

5. M. V. Feigelman, Usp. Fiz. Nauk **169**, 917 (1999).

6. L. V. Ioffe, V. B. Geshkenbein, M. V. Feigelman, *et al.*, Nature **398**, 679 (1999).

7. C. W. J. Beenakker and H. van Houten, Phys. Rev. Lett. **66**, 3056 (1991).

8. T. Kontos, M. Aprili, and J. Lesueur, Phys. Rev. Lett. **86**, 304 (2001).

9. M. Zareyan, W. Belzig, and Yu. V. Nazarov, Phys. Rev. Lett. **86**, 308 (2001).

10. S. Guéron *et al.*, Phys. Rev. Lett. **83**, 4148 (1999).

11. M. Fogelström, Phys. Rev. B **62**, 11812 (2000).

12. S. V. Kuplevakhskii and I. I. Falko, Pis'ma Zh. Éksp. Teor. Fiz. **52**, 957 (1990) [JETP Lett. **52**, 340 (1990)].

13. C. W. J. Beenakker, Phys. Rev. Lett. **67**, 3836 (1991).

14. F. S. Bergeret, A. F. Volkov, and K. B. Efetov, Phys. Rev. Lett. **86**, 3140 (2001).

15. K. K. Likharev, *Dynamics of Josephson Junctions and Circuits* (Nauka, Moscow, 1985; Gordon and Breach, Amsterdam, 1991).

Spin Polaron Approach to Superconductivity

A. F. Barabanov, L. A. Maksimov[1], and A. V. Mikheenkov

Institute of High-Pressure Physics, Russian Academy of Sciences, Troitsk, Moscow region, 142092 Russia
[1] Russian Research Center Kurchatov Institute, pl. Kurchatova 1, Moscow, 123182 Russia
Received May 14, 2001; in final form, August 14, 2001

Superconducting pairing is considered for a two-dimensional system with strong correlation between the carrier subsystem and the subsystem of localized spins. The Kondo lattice model is analyzed for the case where spin polarons are the elementary excitations. It is shown that taking into account only the anomalous Green's functions for bare holes is insufficient for superconducting pairing to occur; it arises only after the introduction of the anomalous Green's functions for spin-polaron operators. © *2001 MAIK "Nauka/Interperiodica".*

PACS numbers: 74.20.Mn; 75.30.Mb

It is well known that, in the standard models of a two-dimensional weakly doped antiferromagnet, bare carriers are described by the Green's function involving both the coherent quasiparticle part and the incoherent part. Such a structure of the Green's function is caused by the strong interaction of bare carriers with the subsystem of localized spins $\hat{\mathbf{S}}_{\mathbf{r}}$. An important point is that the energetically low-lying quasiparticle peak near the band bottom is well defined and its spectral density corresponds to the δ function $Z_{\mathbf{k}}\delta(\omega - \varepsilon_{\mathbf{k}})$ with residue $Z_{\mathbf{k}} \leq 1/2$. This result can be obtained within the framework of the self-consistent Born approximation in the widely used t–J, three-band Hubbard, and Kondo lattice models (see, e.g., [1–4]).

The strong variation of $Z_{\mathbf{k}}$ from unity and the large incoherent part indicate that the bare hole $a_{\mathbf{k}\sigma}^{+}$ is not a good quasiparticle. In this case, a more complex excitation—spin polaron—is a good quasiparticle. It is generally described by the operator

$$p_{\mathbf{k}\sigma}^{+} = a_{\mathbf{k}\sigma}^{+} + b_{\mathbf{k}\sigma}^{+}, \qquad (1)$$

where $b_{\mathbf{k}}^{+}$ is the sum of terms having the following symbolic form: $a_{\mathbf{k} - \mathbf{k}_1 - \mathbf{k}_2 - \ldots - \mathbf{k}_n}^{+}\hat{S}_{\mathbf{k}_1}\hat{S}_{\mathbf{k}_2}\ldots\hat{S}_{\mathbf{k}_n}, \hat{S}_{\mathbf{k}_i}$ (see, e.g., [5]).

In the presently existing theoretical studies of strongly correlated systems, the energetically low-lying spin-polaron states are constructed first to calculate the elementary excitation bands, after which the superconductivity problem is solved by pairing only the bare carriers, without pairing of the operators $a_{\mathbf{k}, \sigma}^{+}$ and $b_{-\mathbf{k}, -\sigma}^{+}$ (see, e.g., [6]).

In this work, the mean-field approach is applied to the simplest model of Kondo lattice [7, 8] to demonstrate that the inclusion of anomalous Green's functions

of the form $\langle\langle b_{-\mathbf{k}, -\sigma}^{+} | a_{\mathbf{k}, \sigma}^{+} \rangle\rangle$ is quite important. Moreover, it will be shown that, within this approach, superconductivity is impossible without inclusion of the indicated Green's functions. In fact, this implies that the strong electron interaction with the excitations of the antiferromagnetically ordered spin subsystem provides superconducting pairing in the model considered.

The Hamiltonian of the Kondo lattice is

$$H^{\text{tot}} = H_0 + H_1 + H_2, \qquad (2)$$

$$H_0 = \sum_{\mathbf{r}, \mathbf{g}} t_{\mathbf{g}} a_{\mathbf{r} + \mathbf{g}, \sigma}^{+} a_{\mathbf{r}, \sigma} = \sum_{\mathbf{k}} \varepsilon_{\mathbf{k}} a_{\mathbf{k}, \sigma}^{+} a_{\mathbf{k}, \sigma}, \qquad (3)$$

$$H_1 = J \sum_{\mathbf{r}, \sigma_1, \sigma_2} a_{\mathbf{r}, \sigma_1}^{+} S_{\mathbf{r}}^{\alpha} \hat{\sigma}_{\sigma_1, \sigma_2}^{\alpha} a_{\mathbf{r}, \sigma_2}, \qquad (4)$$

$$H_2 = \frac{1}{2} I \sum_{\mathbf{r}, \mathbf{g}} S_{\mathbf{r} + \mathbf{g}}^{\alpha} S_{\mathbf{r}}^{\alpha}. \qquad (5)$$

Here, the sites $\mathbf{r}$ form a two-dimensional square lattice, $|\mathbf{g}| = 1$ is the distance to the nearest neighbors, $a_{\mathbf{r}\sigma}^{+}$ is the creation operator for the Fermi particles (holes, for definiteness) with spin indices $\sigma = \pm 1$, H_0 describes the carrier hopping, $t_{\mathbf{g}} = -t$, H_2 is the antiferromagnetic interaction of the localized spins $S = 1/2$ with their nearest neighbors, H_1 is the Hamiltonian of on-site Kondo interaction, $\hat{\sigma}^{\alpha}$ are the Pauli matrices, and α are the Cartesian indices.

Let us write the first two equations of the infinite chain of equations for the Green's functions describing

the hole motion on the antiferromagnetic background. These equations have the following form:

$$\omega \langle\langle a_{\mathbf{r}\sigma}|a_{\mathbf{r}_1, \sigma}^+\rangle\rangle = \delta_{\mathbf{r}, \mathbf{r}_1}$$

$$+ \sum_{\mathbf{g}} t_{\mathbf{g}} \langle\langle a_{\mathbf{r}+\mathbf{g}, \sigma}|a_{\mathbf{r}_1, \sigma}^+\rangle\rangle + J \langle\langle b_{\mathbf{r}\sigma}|a_{\mathbf{r}_1, \sigma}^+\rangle\rangle, \qquad (6)$$

$$\omega \langle\langle b_{\mathbf{r}\sigma}|a_{\mathbf{r}_1, \sigma}^+\rangle\rangle$$

$$= \sum_{\mathbf{g}, \sigma_1} t_{\mathbf{g}} \langle\langle S_{\mathbf{r}}^{\alpha} \hat{\sigma}_{\sigma, \sigma_1}^{\alpha} a_{\mathbf{r}+\mathbf{g}, \sigma_1}|a_{\mathbf{r}_1, \sigma}^+\rangle\rangle$$

$$+ iI e_{\alpha\beta\gamma} \sum_{\mathbf{g}, \sigma_1} \hat{\sigma}_{\sigma, \sigma_1}^{\alpha} \langle\langle S_{\mathbf{r}+\mathbf{g}}^{\beta} S_{\mathbf{r}}^{\gamma} a_{\mathbf{r}, \sigma_1}|a_{\mathbf{r}_1, \sigma}^+\rangle\rangle \qquad (7)$$

$$+ J\frac{3}{4} \langle\langle a_{\mathbf{r}\sigma}|a_{\mathbf{r}_1, \sigma}^+\rangle\rangle - J \langle\langle b_{\mathbf{r}\sigma}|a_{\mathbf{r}_1, \sigma}^+\rangle\rangle$$

$$+ J\sigma \langle\langle 2b_{\mathbf{r}, -\sigma}^+ \sum_{\sigma_1} (\sigma_1 a_{\mathbf{r}, \sigma_1} a_{\mathbf{r}, -\sigma_1})|a_{\mathbf{r}_1, \sigma}^+\rangle\rangle.$$

Here, $b_{\mathbf{r}\sigma} = S_{\mathbf{r}}^{\alpha} \hat{\sigma}_{\sigma, \sigma_1}^{\alpha} a_{\mathbf{r}, \sigma_1}$.

We will take the spherically symmetric singlet state as the ground state of the spin subsystem. This state is characterized by the zero mean spin projection $\langle S_{\mathbf{r}}^{\alpha}\rangle = 0$ for every site and the nonzero antiferromagnetic spin correlations $\langle S_0^{\alpha} S_{\mathbf{r}}^{\alpha}\rangle$ (which are independent of the Cartesian index α [9, 10]).

The last term in Eq. [7] is proportional to the carrier concentration x, which is a small parameter of the problem ($x \le 0.2$ in the region essential to an HTSC).

Let us first consider a weakly doped system in the normal state. The set of Eqs. (6) and (7) for the Green's functions $\langle\langle a_{\mathbf{r}\sigma}|a_{\mathbf{r}_1, \sigma}^+\rangle\rangle$ and $\langle\langle b_{\mathbf{r}\sigma}|a_{\mathbf{r}_1, \sigma}^+\rangle\rangle$ is nonclosed. To close the chain of equations, we use the standard Zwanzig–Mori projection technique [11]. For the set of Eqs. (6) and (7), this means that the first two terms on the right-hand side of Eq. (7) should be approximated by their projections onto a certain operator basis, while the last term can be ignored.

The simplest operator basis set is formed by two operators that appear in the first Eq. (6) of the system of equations. These are the annihilation operators $a_{\mathbf{r}\sigma}$ for the "bare" electron and $b_{\mathbf{r}\sigma}$ for the on-site spin polaron. The choice of this basis implies that the spin polaron is constructed as a coherent superposition of the $a_{\mathbf{k}\sigma}$ operator for the bare hole and $b_{\mathbf{k}\sigma}$ operator for a hole bonded to local spin. Such a local polaron is the analogue of the Zhang–Rice singlet in the three-band Hubbard model. In the limit of strong Kondo interaction J, these local polarons best describe the true lowest quasiparticle band.

After projection, the system of Eqs. (6) and (7) [without the last term in Eq. (7)] takes in the $\mathbf{k}$ representation the form

$$(\omega - \varepsilon_{\mathbf{k}}) G_{\mathbf{k}}^1 = 1 + J G_{\mathbf{k}}^2, \qquad (8)$$

$$(\omega - e_{\mathbf{k}}) G_{\mathbf{k}}^2 = \frac{3}{4} J G_{\mathbf{k}}^1, \qquad (9)$$

$$G_{\mathbf{k}}^1 = \langle\langle a_{\mathbf{k}, \sigma}|a_{\mathbf{k}, \sigma}^+\rangle\rangle; \quad G_{\mathbf{k}}^2 = \langle\langle b_{\mathbf{k}, \sigma}|a_{\mathbf{k}, \sigma}^+\rangle\rangle; \qquad (10)$$

$$\varepsilon_{\mathbf{k}} = -2t(\cos k_x + \cos k_y) - \mu;$$

$$e_{\mathbf{k}} = \left(\frac{4}{3} c_{\mathbf{g}} \varepsilon_{\mathbf{k}} - J - \frac{16}{3} I c_{\mathbf{g}}\right) - \mu. \qquad (11)$$

Here, $b_{\mathbf{k}, \sigma}$, $a_{\mathbf{k}, \sigma}$, and $G_{\mathbf{k}}$ are the Fourier transforms of the corresponding on-site operators and the Green's function, respectively, and $c_{\mathbf{g}} = \langle \mathbf{S}_{\mathbf{r}} \mathbf{S}_{\mathbf{r}+\mathbf{g}}\rangle$ is the spin–spin correlation function. All energies are reckoned from the chemical potential μ.

The solution to the set of Eqs. (8) and (9) leads to the following excitation spectrum in the normal state:

$$\omega_{1, 2}(\mathbf{k}) = \frac{1}{2}\left\{\varepsilon_{\mathbf{k}} + e_{\mathbf{k}} \mp \sqrt{(\varepsilon_{\mathbf{k}} - e_{\mathbf{k}})^2 + \frac{3}{4} J^2}\right\}. \qquad (12)$$

The chemical potential is assumed to lie in the lower ω_1 band.

To describe superconductivity, the operator basis set should be augmented, while projecting, by the operators $a_{\mathbf{r}}^+$ and $b_{\mathbf{r}}^+$. The last term on the right-hand side of Eq. (7) is the only one that has nonzero projection on the additional subspace. Its projection on $a_{\mathbf{r}}^+$ is zero, while the projection on $b_{\mathbf{r}}^+$ has the following form (note that the projection technique gives in this case exactly the same result as does the trivial decoupling):

$$J\sigma \langle\langle 2b_{\mathbf{r}, -\sigma}^+ \sum_{\sigma_1} (\sigma_1 a_{\mathbf{r}, \sigma_1} a_{\mathbf{r}, -\sigma_1}) \Big| a_{\mathbf{r}_1}^+, \sigma\rangle\rangle$$

$$\approx J\eta^* \langle\langle \sigma b_{\mathbf{r}, -\sigma}^+|a_{\mathbf{r}_1}^+, \sigma\rangle\rangle, \qquad (13)$$

$$\eta^* = \left\langle \sum_{\sigma_1} (\sigma_1 a_{\mathbf{r}, \sigma_1} a_{\mathbf{r}, -\sigma_1})\right\rangle. \qquad (14)$$

As a result, the anomalous Green's function $F^2 = \sigma \langle\langle b_{-\mathbf{k}, -\sigma}^+|a_{\mathbf{k}, \sigma}^+\rangle\rangle$ and the anomalous mean η^* appear on the right-hand side of Eq. (7). After standard mathemat-

ics, the above projection technique gives the following closed set of equations for the superconducting case:

$$(\omega - \varepsilon_{\mathbf{k}})G_{\mathbf{k}}^1 = 1 + JG_{\mathbf{k}}^2,$$

$$(\omega - e_{\mathbf{k}})G_{\mathbf{k}}^2 = \frac{3}{4}JG_{\mathbf{k}}^1 + J\eta^*F_{\mathbf{k}}^2,$$

$$(\omega + \varepsilon_{\mathbf{k}})F_{\mathbf{k}}^1 = -JF_{\mathbf{k}}^2, \tag{15}$$

$$(\omega + e_{\mathbf{k}})F_{\mathbf{k}}^2 = -\frac{3}{4}JF_{\mathbf{k}}^1 + J\eta G_{\mathbf{k}}^2;$$

$$F^1 = \sigma\langle\langle a_{-\mathbf{k}, -\sigma}^+ | a_{\mathbf{k}, \sigma}^+ \rangle\rangle; \quad F^2 = \sigma\langle\langle b_{-\mathbf{k}, -\sigma}^+ | a_{\mathbf{k}, \sigma}^+ \rangle\rangle. \tag{16}$$

The great importance of projecting the right-hand side on the spin-polaron operator b^+ is noteworthy. In studies of the spin-polaron excitations, only the projection on the bare-carrier operator $a_{\mathbf{r}}^+$ is usually taken into account (or the approximation equivalent to this projection is used). In some models (t–J or the three-band Hubbard model), such an approach provides the superconducting pairing. Nevertheless, we believe that this approach is limited and may be incorrect because of the vital importance of the b^+ part in the spin-polaron operator p^+ in Eq. (1).

The model under consideration demonstrates this most clearly, because Eq. (13), appearing as a result of projection on the operator b^+, is the only term that gives rise to the superconducting pairing (of both spin polarons and bare holes).

Note that the differentiation of the Green's function F^2 with respect to $a_{\mathbf{k}, \sigma}^+$ allows the polaron–polaron Green's function $F^3 = \sigma\langle\langle b_{-\mathbf{k}, -\sigma}^+ | b_{\mathbf{k}, \sigma}^+ \rangle\rangle$ to be exactly expressed in terms of F^2.

The expressions for the normal Green's functions, the renormalized spectrum, and the renormalized residues $Z_{\mathbf{k}}$ can be obtained by solving the set of Eqs. (15). However, we are interested only in the anomalous Green's function F^1. It has the form

$$F_{\mathbf{k}}^1 = -\left(\frac{3}{4}\right)^2 \eta J^3 D_{\mathbf{k}}^{-1}, \tag{17}$$

$$D_{\mathbf{k}} \equiv \left[(\omega - \varepsilon_{\mathbf{k}})(\omega - e_{\mathbf{k}}) - \frac{3}{4}J^2\right]$$

$$\times \left[(\omega + \varepsilon_{\mathbf{k}})(\omega + e_{\mathbf{k}}) - \frac{3}{4}J^2\right] \tag{18}$$

$$- |\eta|^2(\omega + \varepsilon_{\mathbf{k}})(\omega - \varepsilon_{\mathbf{k}})J^2.$$

The excitation spectrum is found from the equation $D_{\mathbf{k}} = 0$. The latter can conveniently be written as

$$(\omega^2 - \omega_1^2)(\omega^2 - \omega_2^2) - |\eta|^2(\omega^2 - \varepsilon_{\mathbf{k}}^2)J^2 = 0, \tag{19}$$

where $\omega_1(\mathbf{k})$ and $\omega_2(\mathbf{k})$ are given by Eq. (12) for the two-band spin-polaron spectrum.

We assume that the Fermi level lies in the lower polaron band ω_1 and that J is the largest parameter of the problem, $(\omega_2^2 - \omega_1^2) \sim J^2$. We are interested in the solution to Eq. (19) near the Fermi level. For this reason, we can set $(\omega^2 - \omega_2^2) \approx (\omega_1^2 - \omega_2^2)$. Then, $F_{\mathbf{k}}^1$ is given by the expression

$$F_{\mathbf{k}}^1 = \left(\frac{3}{4}\right)^2 \eta J^3 \alpha_{\mathbf{k}}^{-2}[\omega^2 - E_{\mathbf{k}}^2]^{-1}, \tag{20}$$

$$E_{\mathbf{k}} = \sqrt{\omega_1^2\alpha_{\mathbf{k}}^{-2}(\omega_2^2 - \omega_1^2) + \Delta_{\mathbf{k}}^2}, \tag{21}$$

$$\Delta_{\mathbf{k}}^2 = \alpha_{\mathbf{k}}^{-2}\varepsilon_{\mathbf{k}}^2 J^2|\eta|^2, \tag{22}$$

$$\alpha_{\mathbf{k}}^2 = (\omega_2^2 - \omega_1^2) + \frac{3}{4}|\eta|^2 J^2. \tag{23}$$

Using the standard expression for anomalous mean η (14) in terms of the imaginary part of Green's function $F_{\mathbf{k}}^1$ (20), we obtain the self-consistent equation for η

$$\eta = \frac{v}{(2\pi)^2}\int d\omega d\mathbf{k}\, n(\omega)\frac{1}{\pi}\mathrm{Im}F^1, \tag{24}$$

where v is the unit cell area and $n(\omega) = (\exp(\omega/T) + 1)^{-1}$.

It should be emphasized that, although the anomalous Green's function entering Eq. (24) is obtained only for the bare holes, it is related to the polaron functions G_2 and F_2 by Eqs. (15).

After integrating with respect to ω, the equation for η takes the form

$$1 = 2\left(\frac{3}{4}\right)^2 J^3 \frac{v}{(2\pi)^2}\int d\mathbf{k}\,\alpha_{\mathbf{k}}^{-2}\frac{1 - 2n(E_{\mathbf{k}})}{2E_{\mathbf{k}}}. \tag{25}$$

Let us estimate the value of superconducting gap Δ at $T = 0$ in the simplest logarithmic approximation and ignoring the $\mathbf{k}$ dependence for $\Delta_{\mathbf{k}}$ in Eq. (25). Since $\eta^2 \ll 1$, one can set $\alpha_{\mathbf{k}}^{-2}(\omega_2^2 - \omega_1^2) \approx 1$ [see Eq. (23)]. Equation (25) has the standard BCS form with the effective coupling constant $g \sim J^3\alpha_{\mathbf{k}}^{-2} \sim J$ rather than J^2, as would be in the case of weak Kondo interaction.

The typical polaron bands $\omega_1(\mathbf{k}) + \mu$ and $\omega_2(\mathbf{k}) + \mu$ (12) are shown in the figure (for the following parameters: $t_g = -t$, $J = 3t$, $I = 0.4t$, $t = 1$, and $c_g = -0.33$). We assume that the chemical potential is positioned near the center of the lower band. Then, one can easily verify that $\omega_2 \sim J$. The energy cutoff parameter is determined either by the width W_1 of the lower band or by the characteristic spin-excitation energy I. In our case, both are
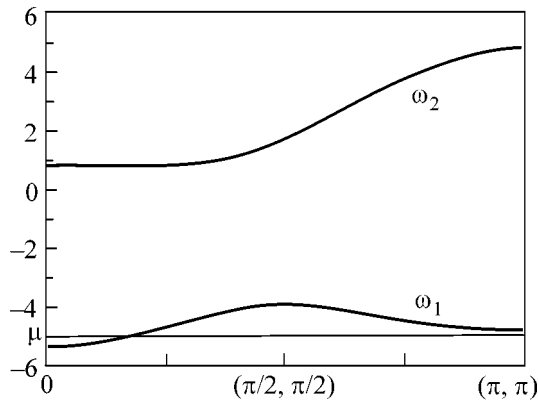
Mutual arrangement of the local spin-polaron (lower curve) $\omega_1 + \mu$ and (upper curve) $\omega_2 + \mu$ bands along the $(0, 0)$–(π, π) direction. The horizontal line indicates (qualitatively) the position of chemical potential in the lower band. The energy parameter is $t = 1$; for the remaining parameters, see text.

on the order of t. Then, one has the following estimate for Δ:

$$\Delta = W_1 \exp\left(-\frac{\pi W_1 \omega_2^2}{2(3/4)^2 J^3}\right) \sim t \exp(-t/J). \qquad (26)$$

The typical value of W_1 for an HTSC is 0.3–0.5 eV, which gives a reasonable estimate $\Delta \approx 100$ K for the gap.

Note that a more accurate estimate of $\Delta_{\mathbf{k}}$ is given by Eq. (22), containing the $\mathbf{k}$ dependence of Δ. This dependence is dominated by the $\varepsilon_{\mathbf{k}}^2$ factor. One can easily see that in our case $\varepsilon_{\mathbf{k}} > 0$ for any $\mathbf{k}$. That is, the gap $\Delta_{\mathbf{k}}$ has no zeros at the Fermi surface. However, as was pointed out above, we used the simplest form of spin-polaron operator, namely, the operator for a local spin polaron. In our recent studies, it was demonstrated by the example of three (s–d [12], effective three-band [13], and t–J [14]) models that the extension of the operator basis, i.e., inclusion of the operators accounting for the "dressing" of local polarons with spin fluctuations on

the scale of spin-correlation length ξ, is highly important for the spin polaron. Such a basis-set extension lowers the spin-polaron band and can lead to a more complicated dependence of Δ on $\mathbf{k}$, including the appearance of zeros for Δ at the Fermi surface.

REFERENCES

1. E. Dagotto, Rev. Mod. Phys. **66**, 763 (1994).
2. Z. Liu and E. Manousakis, Phys. Rev. B **45**, 2425 (1992).
3. G. Martinez and P. Horsch, Phys. Rev. B **44**, 317 (1991).
4. R. O. Kuzian, R. Hayn, A. F. Barabanov, and L. A. Maksimov, Phys. Rev. B **58**, 6194 (1998).
5. O. F. de Alcantara Bonfim and G. F. Reiter, in *Proceedings of the University of Miami Workshop on Electronic Structure and Mechanisms for High Temperature Superconductivity*, Ed. by J. Ashkenazi (Plenum, New York, 1991).
6. N. M. Plakida and V. S. Oudovenko, Phys. Rev. B **59**, 11949 (1999).
7. P. Prelovshek, Phys. Lett. A **126**, 287 (1988).
8. A. Ramsak and P. Prelovshek, Phys. Rev. B **40**, 2239 (1989); **42**, 10415 (1990).
9. A. F. Barabanov and V. M. Beresovsky, Phys. Lett. A **186**, 175 (1994).
10. A. F. Barabanov and V. M. Beresovsky, Zh. Éksp. Teor. Fiz. **106**, 1156 (1994) [JETP **79**, 627 (1994)].
11. H. Mori, Prog. Theor. Phys. **33**, 423 (1965).
12. A. F. Barabanov, O. V. Urazaev, A. A. Kovalev, and L. A. Maksimov, Pis'ma Zh. Éksp. Teor. Fiz. **68**, 386 (1998) [JETP Lett. **68**, 412 (1998)].
13. A. F. Barabanov, R. Hayn, A. A. Kovalev, *et al.*, Zh. Éksp. Teor. Fiz. (2001) (in press); cond-mat/009237.
14. R. Hayn, A. F. Barabanov, and L. A. Maksimov, Physica B (Amsterdam) **259–261**, 749 (1999).

Translated by V. Sakun

Tunnel Nanoengine

A. M. Dykhne[1] and V. V. Zosimov*

Moscow State University, Vorob'evy gory, Moscow, 119899 Russia
* e-mail: zosimov@dubna.ru
[1] Troitsk Institute for Innovation and Thermonuclear Research, Troitsk, Moscow region, 142190 Russia
Received August 14, 2001

The motion of nanoparticles involved in resonance electron tunneling is studied. The motion is caused by the particle charging during the process of resonance tunneling. The possibility of controlling the nanoparticle motion is demonstrated, and the mechanism of self-oscillatory particle motion is considered. © *2001 MAIK "Nauka/Interperiodica"*.

PACS numbers: 82.37.Gk; 82.37.Rs

Nanomechanics—a new direction in the physics of nanoparticles—has emerged primarily due to the advances in tunneling and atomic force microscopies. The essence of this direction consists in the design of various mechanisms (methods) for manipulating nanoparticles, including single molecules.

Part of modern research in nanomechanics amounts to the construction of model potentials which provide directed and controllable molecular motion [1, 2]. At the same time, the method for moving large molecules through the manipulation of an STM tip was already developed several years ago [3–5]. This technique can also be used to accomplish controllable chemical transformations in a single molecule [6]. In the latter case, the reaction is controlled by electron tunneling into the molecule.

One of the possible mechanisms for the control of nanoparticle motion is considered in this work. The model is based on the fact that a particle changes its charge upon electron tunneling in a system configurationally close to a resonance tunneling microscope [7]. The electrochemical variant of the system with a molecule acquiring charge upon electrochemical transition was examined in [8].

The idea is that resonance tunneling involves two steps. An electron first tunnels from a positive electrode to the free level of a particle, after which it tunnels from the particle to the second electrode. At resonance, the electron energy is equal to the energy of the free level, so that its population may be as large as unity (that is why the probability of resonance tunneling is high); i.e., the particle is charged and accelerated in the electric field of the tunnel gap. In the general case, the average charge of the particle is equal to a fraction of the electron charge and depends on the ratio between the probabilities of tunneling from the first electrode to the particle and from the particle to the second electrode. This ratio, in turn, is determined by the ratio of the dis-

tances between the particle and electrodes. As a result, the motion induces a change in the charge of the particle and, hence, changes its acceleration.

Generally speaking, the duration of a single resonance-tunneling event is on the order of electron lifetime at the particle free level; the particle charge may change in this time. On the long-time scale, the resonance current can be regarded as a collection of elementary tunneling events, and the particle charge can be taken equal to the ratio of the electron lifetime at the resonance level to the duration of a single event. Because of this, the method of treating the particle motion depends on the ratio between the duration of an elementary event and the particle time of flight through the gap. This time depends on the particle mass, the gap width, and the applied voltage. The time of flight is

$$t = d\sqrt{\frac{2M}{UeN_A}},$$

where M is the particle molecular weight, U is the applied bias, e is the electron charge, and N_A is Avogadro's number. For a typical gap of 1 nm in STM, a bias of 1 V, and a molecular weight of 100, the time of flight is 5×10^{-11} s. The characteristic electron lifetime at the particle is $t_1 \approx L/vD$, where L is the particle size, v is the electron velocity at the particle free level, $D \approx \exp((-2d/\hbar)\sqrt{2me\varphi})$ is the tunneling probability, and φ is the electron work function. For a typical work function of 1 V, the lifetime is 10^{-13} s.

Therefore, we face the situation where the number of elementary tunneling events during the particle flight time is much larger than unity. We will consider hereafter only this regime. The reverse situation or the general case is also of interest, but they require the solution of a nontrivial quantum-mechanical problem of an ion with a partially occupied level in the electric field. In our case of a pulsed particle motion—the particle

acquires a unit charge for a short time and speeds up, then loses charge to execute inertial motion, and then again acquires a charge, and so on—one can easily show that the motion with a large number of such steps is equivalent to the motion with a fractional charge equal to the ratio of the average charge-residence time on the particle to the average interval between acquiring a charge.

Let us consider a system of two electrodes separated by a vacuum gap, with a nanoparticle placed in it and having free electronic levels. The tunneling current in such a system is determined by the resonance tunneling.

Let w_1 be the probability of tunneling from the first electrode to the particle and w_2 be the same for the second transition (i.e., the width of the resonance level). In this case, the tunneling current is given by

$$i = \frac{e}{\hbar} \frac{\Gamma_1 \Gamma_2}{\Gamma_1 + \Gamma_2}, \quad (1)$$

where $\Gamma_{1,2} = \hbar w_{1,2}$.

At the same time, the current can be expressed in terms of the particle charge e_p and the time $1/w_2$ of tunneling from the particle to the second electrode:

$$i = e_p w_2 = e_p \Gamma_2 / \hbar. \quad (2)$$

By comparing Eqs. (1) and (2), one gets

$$e_p = e \frac{\Gamma_1}{\Gamma_1 + \Gamma_2} = e \frac{1}{1 + w_2/w_1}. \quad (3)$$

If $w_1 \gg w_2$, i.e., if the particle is closer to the first (negative) electrode, then $e_p \approx e$ and the particle is repelled from it. If $w_2 \gg w_1$, then $e \approx 0$ and the electric force does not act on the particle. With the standard STM configuration, a change in the voltage sign at this instant of time will reverse the direction of motion. As for the current, it changes and, according to Eq. (1), increases to a maximum value when $\Gamma_1 = \Gamma_2$, i.e., when the particle is in the middle of the gap, or decreases to a minimum value if the particle is at the end of its motion. Current measurements with high time resolution offer the basic possibility of controlling the particle motion.

Let us now consider another manifestation of this mechanism, namely, the mechanical self-oscillations of a particle, and take into account the van der Waals force, which can restore the particle to the negative electrode. This becomes possible if the second electrode is far away and we are dealing with a field emission in a uniform field. Let us write the set of equations of motion for a particle in such a system. The simplified energy diagram for an electron in this system is presented in Fig. 1. The relevant probabilities are given by the expressions

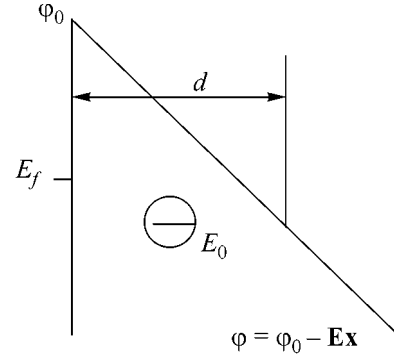$$w_1 = \exp\left[-\frac{2}{\hbar} \int_0^x \sqrt{2m(e(\varphi_0 - Ex) - \epsilon_0)} dx\right],$$

Fig. 1. Energy diagram for an electron under field-emission conditions.

$$w_2 = \exp\left[-\frac{2}{\hbar} \int_x^d \sqrt{2m(e(\varphi_0 - Ex) - \epsilon_0)} dx\right].$$

Let $(4/3\hbar)\sqrt{2eEmd} = \kappa_0$. Then Eq. (2) gives for the particle charge

$$e_p = \frac{e}{1 + \exp(-\kappa_0 d(-1 + 2(1 - x/d)^{3/2}))}.$$

The force acting on the particle is

$$F = E_0 e_p - AR/6x^2,$$

where R is the particle radius and the expression for the van der Waals force is chosen in the form corresponding to the attraction between a sphere and a plane. The maximum particle charge is e, and the constant A is typically on the order of 10^{-19} J. Let $d \sim 1$ nm and $E \sim 10^9$ V/m. Then,

$$\frac{AR}{6x^2} \approx \frac{1}{2} 10^{-10}, \quad eE \approx 10^{-10};$$

i.e., the balance between the van der Waals and electrostatic forces is possible.

The equation of motion is merely

$$m_p \ddot{x} = E_0 e_p - AR/6x^2. \quad (4)$$

Let us introduce the characteristic magnitude of the electrostatic force,

$$f_0^e = E_0^e e,$$

and of the van der Waals force,

$$f_0^e = AR/6d^2.$$

One can easily estimate their ratio:

$$\alpha = \frac{f_0^e}{f_0^e} = \frac{R}{6d} \frac{A}{E_{kin}},$$

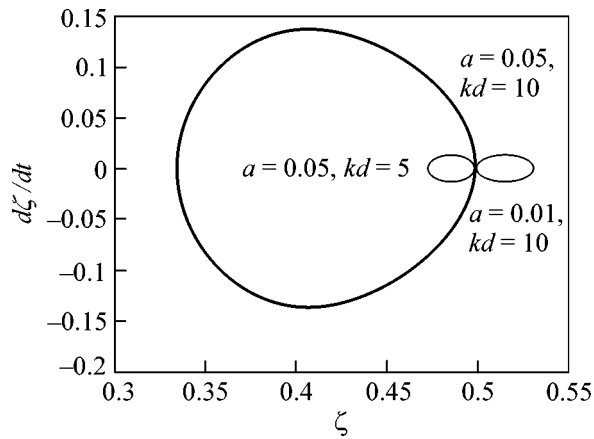**Fig. 2.** Phase portrait of Eq. (5) for different values of parameters.

the system. The oscillation period in physical units is on the order of 0.01–0.1 ns. Note that the charged particle oscillating with this frequency should irradiate an electromagnetic wave in the gigahertz region, which, in principle, is accessible to observation.

Thus, the charging of resonantly tunneling particles can lead to the effects that are of both theoretical and applied interest. Placing such a particle in a transversely nonuniform field, where the translatory motion of the particle can be controlled, may offer considerable promise.

where E_{kin} is the typical electron kinetic energy. The ratio α is on the order of 0.1–0.001. We next set $\xi = x/d$ and $\tau = t/t_0$, where $t_0 = \sqrt{dm_p/f_0^e}$ is the characteristic flight time of a particle with charge e under the action of field E_0, and construct the phase portrait (for different α and $\kappa_0 d$) of the equation (Fig. 2)

$$\frac{d^2\xi}{d\tau^2} = \frac{e_p}{e} - \alpha\frac{1}{\xi^2}, \tag{5}$$

obtained from Eq. (4) after bringing it to the dimensionless form. The $\kappa_0 d$ parameter is on the order of 5–10. One can see that the particle executes periodic oscillations with amplitude depending on the parameters of

REFERENCES

1. M. Porto, M. Urbakh, and J. Klafter, Phys. Rev. Lett. **84**, 6058 (2000).
2. M. Porto, M. Urbakh, and J. Klafter, Phys. Rev. Lett. **85**, 491 (2000).
3. J. A. Stroscio and D. M. Eigler, Science **254**, 1319 (1991).
4. Y. Z. Li, M. Chander, J. C. Partin, *et al.*, Phys. Rev. B **45**, 13837 (1992).
5. P. H. Beton, A. W. Dunn, and P. Moriaty, Appl. Phys. Lett. **67**, 1075 (1995).
6. S.-W. Hla, L. Bartles, G. Meyer, and K.-H. Rieder, Phys. Rev. Lett. **85**, 2777 (2000).
7. A. M. Dykhne, S. Yu. Vasil'ev, O. A. Petriĭ, *et al.*, Dokl. Akad. Nauk **368**, 467 (1999) [Dokl. Phys. **44**, 653 (1999)].
8. F.-R. F. Fan and A. J. Bard, Science **267**, 871 (1995).

Translated by V. Sakun

Diboride Bifullerenes and Binanotubes

L. A. Chernozatonskiĭ

Emanuel Institute of Biochemical Physics, Russian Academy of Sciences, ul. Kosygina 4, Moscow, 119991 Russia
e-mail: cherno@sky.chph.ras.ru
Received August 16, 2001

The structures and energy characteristics of a new class of nanotubes and fullerenes formed by binary layers of a trigonal network of metal atoms M and a graphite-like network of boron atoms are considered by the example of magnesium and zirconium diborides. It is shown that, contrary to the familiar carbon monolayer nanotubes, the dependence of the strain energy of diboride bitubulene on its diameter D deviates from the $1/D^2$ law because of the "crustlike" shape of a free fragment of the MB_2 bilayer, while bitubulenes with axis parallel to the M–M bonds have the optimum shape at a given diameter. Such bitubulenes are expected to be metallic because of the specific features of the band structure of bilayered diborides. © 2001 MAIK "Nauka/Interperiodica".

PACS numbers: 61.48.+c; 61.46.+w; 74.72.-h

Over the last decade, two types of materials—high-temperature superconductors and fullerene structures—have attracted attention because of their remarkable properties and broad spectrum of possible applications in solid-state physics and chemistry. The discovery of the carbon, BN, and dichalcogenide $(Mo, W)S_2$ nanotubes [1] and the superconductivity of MgB_2 at 39 K [2] has led to the explosive activity of researchers in these fields. In both cases, one deals with layered structures. In this communication, the possible existence of a new class of binary diboride nanotubes—MB_2 (M = metal atom) bitubulenes—which, being metals, are expected to possess superconducting properties even at sufficiently high temperatures, is discussed.

Recent structural studies of various diborides have revealed (see, e.g., [3, 4]) that the superconductivity of MgB_2 is caused by the proximity of its structure, which is composed of two-dimensional boron layers and metal atoms intercalated between them, to the lattice instability boundary. Among such diborides, superconductivity at $T_c = 5.5$ K was recently observed in ZrB_2 [5]. For this reason, this material is chosen below as the second example of bitubulene, MgB_2 being the first one.

Bitubulenes. Earlier, Hartree–Fock and LDA calculations [6] demonstrated that the stable tubular boron formations containing a trigonal network of interatomic bonds, with B atoms bonded to six neighbors, are possible. When calculating the optimum geometry of the diboride nanotubes under study, it was also assumed that each boron atom is bonded to six neighbors, but in such a way that the structure of nanotubes corresponded to the two-layer structure of bulk MB_2 diboride, i.e., to the graphite-like B layer and a trigonal metal layer with M atoms at the centers of boron hexagons [6]. Similar to the carbon nanotubes [1], bitubu-

lenes can be classified by two indices of an unrolled two-dimensional hexagonal lattice: $\mathbf{B} = n\mathbf{a}_1 + m\mathbf{a}_2$, where the length of vector $\mathbf{B}$ is equal to the circumference of the outer cylindrical boron sheet. They can also be divided into three classes: $n = m$ (armchair), $n \neq 0$, $m = 0$ (zigzag), and $n \neq m$ (chiral).

As in the bulk MB_2 material, the electron-deficient boron layer in bitubulene is stabilized due to the electron donation from metal atoms M. Therefore, the bonding between atoms M and B is of the intermediate (partially ionic) type, as in hexagonal boron nitride [7]. The Pauling bond ionicity, defined as $f = 1 - \exp[-(x_a - x_b)^2/4]$, is 0.15 in MgB_2, i.e., lower than in BN (0.22), and is the same in ZrB_2 (electronegativities $x_{Mg} = 1.2$, $x_B = 2$, and $x_{Zr} = 1$) [8]. The cylindrical surface of BN is ruffled due to lattice relaxation, so that such a nanotube can be considered as a "two-layer" tube composed of oppositely charged coaxial cylinders [9] to provide the energetically most favorable configuration of the BN nanotubes [10]. However, whereas a small "intercylindrical" separation (0.3 Å) decreases with an increase in the diameter of the BN tube, an analogous distance in the MB_2 bitubulenes approaches its bulk interlayer spacing. The MB_2 bitubulenes also tend to take an energetically favorable configuration. The reason is that the hexagonal fragment of the MB_2 bilayer, contrary to the graphite-like layer, has a "crust," rather than planar configuration. The crust is predominantly rolled up around the axis parallel to the M–M bonds, as in (5, 5) bitubulene shown in Fig. 1; i.e., it takes a nearly cylindrical shape. Because of this, the bitubulenes with such a bilayer roll-up and the outer boron tube of the armchair (n, n) type are more stable. The strain energy E_{strain} of these bitubulenes, hereafter called armchair bitubulenes, has a minimum at a certain diameter D_0 of the outer tube [for the MgB_2 (11, 11) bitubulene, $D_0 \approx$
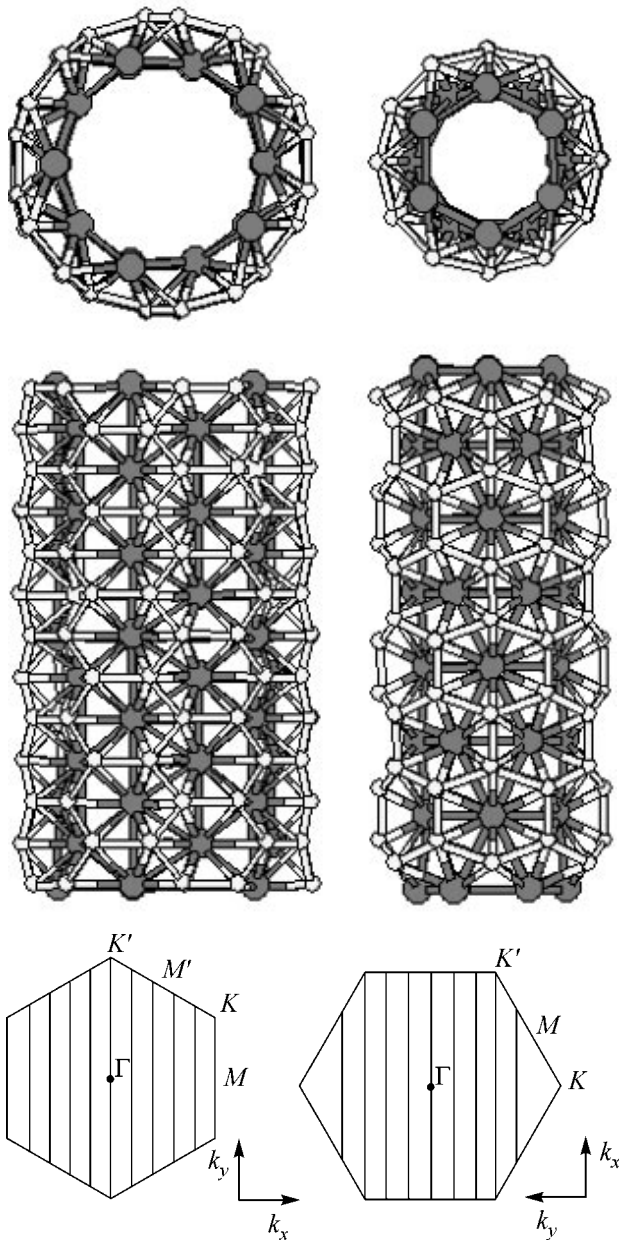
Fig. 1. At the top: (left) the armchair (5, 5) and (right) the zigzag (6, 0) MB_2 bitubulenes. At the bottom: the allowed wave vectors in the Brillouin zones of the hexagonal MB_2 layers in the respective tubulenes. They include the Γ–K direction for the (n, n) bitubulene and the Γ–M direction for the $(n, 0)$ bitubulene, along which the Fermi level always intersects the boron σ and π branches (see Fig. 2 and figures in [4]). The M and B atoms are shown by the dark and light circles, respectively.

19 Å; see table], in contrast to the carbon single-wall nanotubes (SWNTs), for which $E_{\text{strain}}(D) \sim 1/D^2$ [1]. It is also seen in the table that the separation between the cylinders of the (n, n) bitubulene increases with increasing diameter and, most likely, tends in the limit $n \gg 1$ to the value $c = 3.5$ Å corresponding to the MgB_2

crystal. Since the optimum roll-up radius of a fragment of the zirconium diboride bilayer ($r \approx 22$ Å; see table) is larger than the radius of the structurally analogous MgB_2 bilayer, one should expect that the strain energy of the (27, 0) bitubulene with diameter $D_0 \approx 45$ Å is minimal, while the $E_{\text{strain}}(D)$ dependence for $D < D_0$ is closer to $1/D^2$. The geometries of the bitubulene fragments of identical length [11 unit cells for (n, n) bitubulenes and 13 for $(n, 0)$ bitubulenes] were optimized by the molecular dynamics method MM+, which was earlier used, e.g., for calculating the polymer phases of carbon SWNTs [11]. Similar calculations of a four-layer fragment of the MgB_2 crystal gave unit cell parameters close to their experimental values: $a = 3.1$ Å and $c = 3.5$ Å [2–4, 7]. The bitubulene parameters given in the table correspond to the geometry calculated for the central unit cell of the fragment. Note that the values of E_{strain} calculated by the same method for the carbon nanotubes and fullerenes are close to those obtained by the pseudopotential calculations for SWNTs [12] and fullerenes [13].

The bitubulenes with a zigzag $(n, 0)$ outer tube are less stable (see table and Fig. 1). The strain energy of the zigzag bitubulenes also has a minimum at a certain diameter D_0 of the outer tube [e.g., $D_0 \approx 20$ Å for the MgB_2 (20, 0) bitubulene], likely, also because of the crustlike shape of the MB_2 bilayer. Therefore, similar to the BN nanotubes [10], one should expect that it is the armchair bitubulenes which will predominantly grow in the synthesis of the MB_2 bitubulenes.

It is known that the interaction between metal (M) and boron (B) atoms is relatively weak [3, 7]. For this reason, the structure of MB_2 can be considered composed of two mutually bonded sublattices. This is reflected in the band structure of diborides. For example, the boron σ and π branches in MgB_2 and CaB_2 lie near the Fermi level in the Γ–M and Γ–K directions [3, 4], similar to the analogous branches in a hypothetical graphite-like boron layer [4] (Fig. 2). Because of this, the diboride tubes (bitubulenes) considered in this work should be metallic. This follows from the well-known fact that, due to the periodic boundary conditions for the electron wave functions of the nanotubes formed from a hexagonal layer, their two-dimensional Brillouin zones are dissected with lines corresponding to the allowed values of wave vector $\mathbf{k} = (k_x, k_y)$ [1], with at least one section [in the Γ–K direction for the (n, n) bitubulene and Γ–M direction for the $(n, 0)$ bitubulene; cf. the scheme of dissected Brillouin zones in Fig. 1 and the band structure of MgB_2 in Fig. 2] along which the Fermi level intersects the corresponding boron σ and π states in the energy spectrum of MB_2 bitubulene.

Similar to SWNTs [1], the bitubulene can be "capped" with a continuous MB_2 network in the form of a half coaxial polyhedron (Fig. 3). The possible defects necessary for capping the bitubulene are as fol-

Characteristics of bitubulenes and bifullerenes

MgB$_2$					
	n	E_{strain} (eV)	DM (Å)	DB (Å)	$DB–DM$ (Å)
bitubulene (n, n)	6	0.293	8.72	11.54	2.82
	7	0.216	10.18	13.09	2.91
	8	0.170	11.68	14.66	2.98
	9	0.146	13.19	16.18	2.99
	10	0.134	14.73	17.73	3.00
	11	0.132	16.28	19.29	3.01
	12	0.134	17.81	20.83	3.02
	13	0.138	19.36	22.39	3.03
	14	0.145	20.92	23.95	3.03
	15	0.151	22.48	25.52	3.04
layer fragment		0.127	17.80	21.00	3.20
bitubulene $(n, 0)$	14	0.214	11.88	14.85	2.97
	18	0.159	15.40	18.41	3.01
	20	0.155	17.21	20.23	3.02
	22	0.159	18.94	21.97	3.03
	24	0.162	20.73	23.76	3.03
ZrB$_2$					
	n	E_{strain} (eV)	DM (Å)	DB (Å)	$DB–DM$ (Å)
bitubulene (n, n)	7	0.341	10.27	12.98	2.71
	8	0.260	12.37	15.3	2.93
	9	0.206	14.04	16.99	2.95
	10	0.165	15.62	18.62	3.00
	11	0.135	17.19	20.21	3.02
	12	0.113	18.77	21.81	3.04
	13	0.095	20.37	23.43	3.06
	14	0.084	21.96	25.04	3.08
	15	0.075	23.59	26.70	3.11
layer fragment		0.049	41.76	45.04	3.28
Bifullerenes					
		E_{strain} (eV)	DM (Å)	DB (Å)	$DB–DM$ (Å)
Mg$_{32}$B$_{62}$		1.456	7.5	10.3	2.8
$(MgB_2)_{30}^{*}$		1.456			
$(MgB_2)_{30}^{**}$		1.410			
Mg$_{92}$B$_{180}$		0.758	13.4	16.4	3
$(MgB_2)_{90}^{*}$		0.743			
$(MgB_2)_{90}^{**}$		0.661			
Mg$_{182}$B$_{360}$		0.545	18.5	21.4	3.1
$(MgB_2)_{180}^{*}$		0.541			
$(MgB_2)_{180}^{**}$		0.491			
Mg$_{290}$B$_{576}$		0.418	24.2	27.4	3.2
$(MgB_2)_{288}^{*}$		0.415			
$(MgB_2)_{288}^{**}$		0.375			

E_{strain} is the strain energy per one atom; DM is the diameter of the inner metallic shell; DB is the diameter of the outer boron shell. For the fragment of the $(M_{112}B_{215})$ layer, the lowest boron-deficient values of E_{strain} are given, because the energies E_{strain} for the stoichiometric composition of MB$_2$ are several times higher. The mark * denotes bifullerenes with vacancies in two M hexagons, and ** denotes bifullerenes with vacancies in two M pentagons; the corresponding DM and DB values are not presented because of the nonsphericity of these bifullerenes.
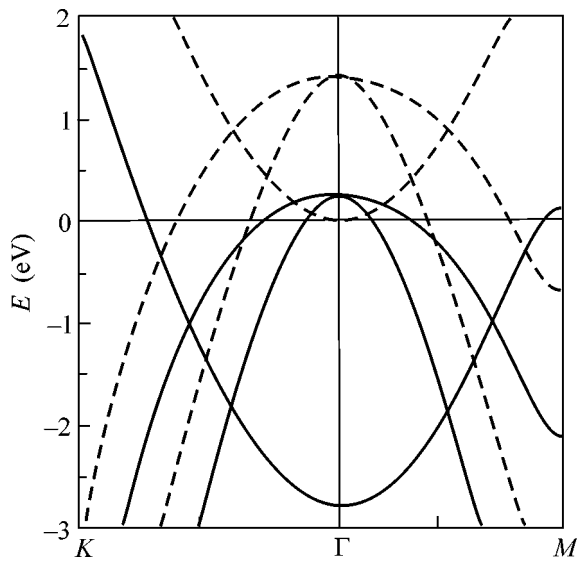
Fig. 2. Energy bands of (solid lines) the MgB_2 crystal [3, 4] and (dashed lines) the hexagonal B_2 layer [4]. The Fermi level ($E = 0.00$ eV) always intersects the boron σ and π branches shown in the figure. It is seen that the metal intercalation in the boron layer raises the Fermi level without a significant change in the band structure near the Fermi level.

Fig. 3. The cap of the zigzag MgB_2 (9, 9) bitubulene: half $(MgB_2)_{90}$ bifullerene with six pentagonal defects. At the bottom: (left) pentagonal and (right) tetragonal defects. The defect-forming atoms in the trigonal Mg network are shown by black circles.

lows (Fig. 3): M pentagon in the M shell and B pentagon in the B shell or M tetragon in the M shell and two edge-shared B pentagons in the B shell. A "stoichiometric" defect formed by the vacancy in the M shell (hexagon or pentagon without central atom M) should always be present in a half stoichiometric MB_2 fullerene [see cap of the (9, 9) bitubulene in Fig. 3].

Bifullerenes. The polyhedral MB_2 structures were also modeled in this work. They are characterized by a "two-layer" structure formed from coaxial fullerenes; the "outer" layer is formed from the boron atoms, and the "inner" layer, from the metal atoms (Fig. 4). Interestingly, the number $N^G(MB_2) = N_M^G + N_B = 3N_M^S + 2$ of atoms in the geometrically filled bifullerene shells differs by two metal atoms from its stoichiometric number $N(MB_2) = 3N_M^S$. The reason is that the number of metal atoms in the geometrically filled trigonal network is equal to the number N_M^f of atoms in the corresponding hexagonal–pentagonal M fullerene plus the number of additional M atoms completing the trigonal fullerene M network ($N_M^G = N_M^f + n_h + n_p = 2 + 0.5N_B/2$, where n_h and n_p are the numbers of hexagons and pentagons, respectively), whereas the number of boron atoms in the usual fullerene network should be $N_B = 6n_h + 5n_p = 2N_M^S$. As a result, the strain energy of the stoichiometric MB_2 bifullerene containing two vacancy defects in the trigonal network of "geometric" fullerene is lower than the energy of a bifullerene of the "geometric"
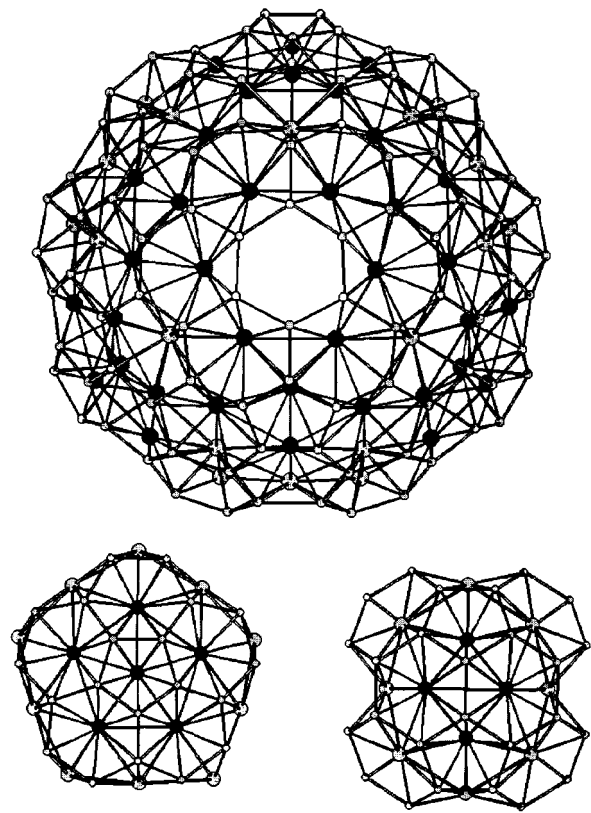
composition (table). Thus, the formation of the MB_2 bifullerene isomers differing by the arrangement of vacancy pairs in their metallic shells is possible. The MM+ method was also used to optimize the shapes and strain energies of typical bifullerenes. The data for the $(MgB_2)_{30, 90\ 180,\ 288}$ bifullerenes whose halves serve as caps for the armchair (n, n) bitubulenes with, respectively, $n = 5, 9, 12$, and 15 are presented in the table.

Similar to other layered materials [1], diborides can form multilayer polyhedral structures, e.g., multilayer bitubulenes and "onions." It follows from the diameters of the MgB_2 bitubulenes and bifullerenes given in the table that these may be, e.g., the MgB_2 (7, 7)@(11, 11)@(15, 15) bitubulene or the $(MgB_2)_{180}$@$(MgB_2)_{288}$ bifullerene.

The MB_2 bitubulenes are attractive for physicochemical studies and practical use because, first, of their possible high-temperature superconductivity and, second, of the enhanced efficiency of field emission from their tips [14]. Since the work function for ZrB_2 (3.6 eV [7]) is lower than for graphite (4.5 eV), one can expect the lowering of the operating voltage for emitters made from ZrB_2 bitubulene. The applications of diboride bifullerenes may be widespread. For instance,
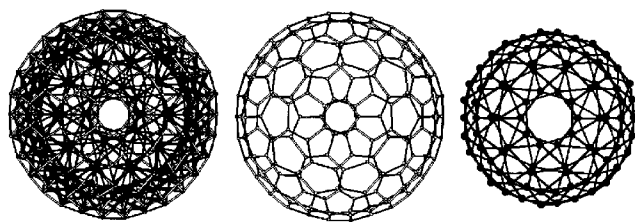
Fig. 4. (Left) $(MgB_2)_{90}$ bifullerene of symmetry S_{12}, (middle) its outer shell (B_{180} fullerene), and (right) its inner Mg_{90} shell (Mg_{92} fullerene with two Mg vacancies in the trigonal network).

these materials can display unusual optical properties and be used as photonic crystals [15]. The polyhedral diboride structures can be prepared, most likely, by the methods that are used for synthesizing the nanotubes and fullerenes [1, 2].

REFERENCES

1. R. Saito, G. Dresselhaus, and M. S. Dresselhaus, *Physical Properties of Carbon Nanotubes* (Imperial College Press, London, 1998).

2. K. J. Nagamatsu, N. Nakagawa, T. Muranaka, *et al.*, Nature **410**, 63 (2001).

3. N. I. Medvedeva, Yu. E. Medvedeva, A. L. Ivanovskiĭ, *et al.*, Pis'ma Zh. Éksp. Teor. Fiz. **73**, 378 (2001) [JETP Lett. **73**, 336 (2001)].

4. J. B. Neaton and A. Perali, cond-mat/0104098 (2001).

5. V. A. Gasparov, N. S. Sidorov, I. I. Zver'kova, and M. P. Kulakov, Pis'ma Zh. Éksp. Teor. Fiz. **73**, 601 (2001) [JETP Lett. **73**, 532 (2001)]; cond-mat/0104323 (2001).

6. I. Boustani, Int. J. Quantum Chem. **52**, 1081 (1994); Phys. Rev. B **55**, 101 (1997).

7. G. V. Samsonov, T. I. Serebryakova, and V. A. Neronov, *Borides* (Nauka, Moscow, 1975); *Boron and Refractory Borides*, Ed. by V. I. Matkovich (Springer-Verlag, Berlin, 1977).

8. J. C. Phillips, Rev. Mod. Phys. **42**, 317 (1970).

9. X. Blasé, A. Rubio, S. D. Louie, and M. L. Cohen, Europhys. Lett. **28**, 335 (1994).

10. M. Menon and D. Srivastava, Chem. Phys. Lett. **307**, 407 (1999).

11. L. A. Chernozatonskii, Chem. Phys. Lett. **297**, 257 (1998).

12. D. H. Robertson, D. W. Brenner, and J. W. Minimire, Phys. Rev. B **45**, 12592 (1992).

13. J. Tersoff, Phys. Rev. B **37**, 6991 (1988).

14. L. A. Chernozatonskii, Yu. V. Gulyaev, Z. Ya. Kosakovskaya, *et al.*, Chem. Phys. Lett. **233**, 63 (1995).

15. B. Temelkuran, E. Ozbay, M. Sigalas, *et al.*, Appl. Phys. A **A66**, 363 (1998).

Translated by V. Sakun

Combined Strain and High-Pressure Oxygen Treatment Effects and Phase Separation in La$_{0.67}$Ca$_{0.33}$MnO$_3$ Thin Films[1]

A. Nossov[1]* and P. Strobel[2]

[1] *Institute of Metal Physics, Ural Division, Russian Academy of Sciences,*
ul. S. Kovalevskoĭ, Yekaterinburg, 620219 Russia
*e-mail: nossov@imp.uran.ru
[2] *Laboratoire de Cristallographie, CNRS, BP 166, 38042 Grenoble, France*
Received August 16, 2001

Evidence for phase separation in high-pressure oxygen-treated La$_{0.67}$Ca$_{0.33}$MnO$_3$/(100)MgO thin films is presented. This phase-separated state is not observed for the $x = 0.33$ classical doping level either for bulk material or for as-prepared thin films. It originates from the combined influence of two factors: large strains due to the film–substrate lattice mismatch and high-pressure (100 bar) annealing in oxygen. These factors weaken double exchange, drastically enhance low-field magnetoresistance, and lead to hysteresis phenomena. The experimental results are interpreted in terms of phase separation of the film volume into the ferromagnetic conductive matrix with inclusions of spin-glass-like clusters. © 2001 MAIK "Nauka/Interperiodica".

PACS numbers: 75.70.-i; 75.80.+q; 75.30.Vn

Hole-doped perovskite manganites of general formula A$_{1-x}$B$_x$MnO$_3$, where A is a trivalent rare-earth ion and B is a divalent alkaline-earth ion, belong to the family of strongly correlated systems with complex interplay between the spin, charge, lattice, and orbital degrees of freedom. Among numerous interesting physical effects observed in doped manganites (the metal–insulator transition, interplay between ferro- and antiferromagnetism, charge ordering, etc.) the most fascinating one is the "colossal" magnetoresistance (CMR) effect that has attracted enormous interest over the last several years [1]. Extremely high CMR values, exceeding 10^6% at 60 K and in a magnetic field of 80 kOe, were reported [2]. This CMR phenomenon is common to the class of doped oxide magnetic semiconductors in which similar, or even greater (exceeding 11 orders of magnitude), CMR values were observed [3] at low temperatures. It was demonstrated that introduction of carriers in the parent antiferromagnetic insulating LaMnO$_3$ compound, either by divalent cation doping [4] or by creation of vacancies in one of sublattices [5], leads to ferromagnetism, conductivity, and CMR. Owing to suppression of spin fluctuations by the magnetic field, maximum magnetoresistance is observed in the vicinity of a ferromagnetic ordering temperature (T_C) and is accompanied by metal–semiconductor transition. Basic physics of doped manganites is described within the framework of the "double exchange" model

[6] assuming domination of ferromagnetic exchange over the antiferromagnetic superexchange and conductivity via carrier hopping with spin memory between the localized states with strong on-site Hund's rule coupling. For a long time, the A$_{1-x}$B$_x$MnO$_3$ compounds with the "classical" $x \approx 0.33$ doping level and large ionic radius of doping cation were considered as model ones for investigations of "double exchange" physics. Recently, the electronic phase separation model [7] (ferromagnetic conductive droplets in antiferromagnetic insulating matrix) was proposed as an alternative for explanation of CMR phenomena in doped manganites. Due to reduced dimensionality, the physical properties of thin-film manganites differ substantially from that of the bulk. For example, evidence for the coexistence of ferromagnetic metallic and charge-ordered insulating phases (with matrix being insulating antiferromagnet) in strained La$_{0.67}$Ca$_{0.33}$MnO$_3$ thin films at low temperatures was recently presented [8].

In this letter, we experimentally show that, by the combined influence of two factors, large film–substrate lattice mismatch and high-pressure oxygen treatment, it is possible to transfer the homogeneous thin film of the classical ferromagnetic conductive La$_{0.67}$Ca$_{0.33}$MnO$_3$ composition into the new phase-separated state.

Epitaxial 2500-Å thin films of La$_{0.67}$Ca$_{0.33}$MnO$_3$ (LCMO) were prepared on (100)MgO substrates by pulsed laser deposition. The target was made using a traditional ceramic technology by mixing high-purity binary oxides and repeated cycles of grinding and sintering. Deposition was carried out at the substrate tem-

---

[1] This article was submitted by the authors in English.

perature 700°C under 300-mtorr partial O_2 pressure. After deposition, the oxygen pressure in the chamber was increased to 1 atm and the films were slowly cooled to the ambient temperature. The first annealing was performed in flowing oxygen at 850°C for two hours. The second annealing was carried out in an autoclave under 100-bar oxygen pressure at the same temperature and for the same duration. Resistivity was measured by conventional four-probe dc or ac techniques at frequencies lower than 80 Hz in a superconducting solenoid with electric current parallel to the magnetic field. Magnetic properties were measured in the $5 \leq T \leq 300$ K temperature range using a vibrating sample magnetometer. Chemical composition of the deposited films was found to be identical to that of the target, as was confirmed by scanning electron microprobe microanalysis and Rutherford backscattering. The results of X-ray diffraction investigations show that, under the above-mentioned conditions, manganite films with lattice parameter $a \approx 3.9$ Å grow epitaxially in "cube-on-cube" mode on the surface of (100)MgO substrate (lattice parameter $a \approx 4.213$ Å). Due to the large film–substrate lattice mismatch, anisotropic strains exist in the film.

The temperature dependences of zero-field resistivity $\rho(0, T)$ and magnetoresistance $MR_H(H, T)$ for as-deposited annealed thin films and the target are compared in Fig. 1. Magnetoresistance is defined here as $MR_H(H, T) = (\rho(H, T) - \rho(0, T))/\rho(H, T) \times 100\%$, where $\rho(H, T)$ and $\rho(0, T)$ are resistivity values under the applied magnetic field H and in zero field, respectively, at temperature T. For the convenience of comparison, the $\rho(0, T)$ curves are normalized to the corresponding resistivity values at 300 K. Note the logarithmic scale in the graphs. In the vicinity of the ferromagnetic ordering temperature, variations of resistivity and magnetoresistance for as-deposited film and the film annealed in flowing oxygen are similar to that of the target. Substantial magnetoresistance, observed for the target at low (<100 K) temperatures, is due to the tunneling of spin-polarized carriers through the grain boundaries of polycrystalline material. Small $MR_H(50\ \text{kOe}, T)$ values at low temperatures, observed for all thin films, indirectly confirm their high crystalline quality. A drastic increase in both resistivity and magnetoresistance are observed for the film subjected to high-pressure treatment. The peak in both curves is shifted by 130 K to lower temperatures, as compared to as-prepared films. This is accompanied by hysteresis phenomena observed both in $\rho(0, T)$ and $MR_H(H, T)$ curves (Fig. 2). Each curve presented in the lower panel of Fig. 2, as well as the magnetization data for this film, were recorded after zero-field warming the film to 300 K and its subsequent cooling to the temperature of measurement. The maximum drop in resistivity upon the application of a magnetic field was observed in low (≤ 2 kOe) fields for the temperature range close to that where the peak in $\rho(0, T)$ curve is observed (compare Fig. 1 and
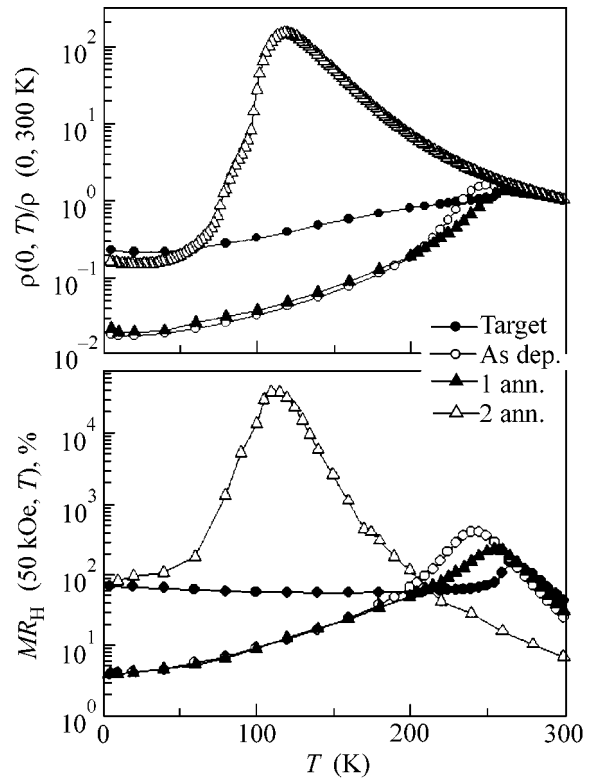

Fig. 1. Temperature dependences of normalized zero-field resistivity $\rho(0, T)/\rho(0, 300\ \text{K})$ (upper panel) and magnetoresistance $MR_H(50\ \text{kOe}, T)$ (lower panel) for $La_{0.67}Ca_{0.33}MnO_3$ thin films and the target.

the lower panel of Fig. 2). No hysteresis phenomena were observed for as-prepared film nor for the film annealed in flowing oxygen. The results of low-temperature magnetic measurements are presented in Fig. 3. Upon application of a magnetic field, typically ferromagnetic hysteresis loops were obtained for all films. Slowly varying background from the substrate was subtracted from all curves shown in the upper panel of Fig. 3. The coercive force increased from $H_C = 310$ Oe for as-prepared film to 413 Oe for the film annealed under high oxygen pressure. Hysteresis phenomena observed for this film are illustrated in the lower panel of Fig. 3. Large differences between the zero-field-cooled and field-cooled curves are observed below 150 K. These results can be understood in terms of phase separation. Under the combined influence of film–substrate strains and high-pressure oxygen treatment, the volume of the film is separated into two phases: the conductive ferromagnetic matrix, giving the dominant contribution to the magnetic properties and conductivity at low temperatures (see upper panels in Figs. 2 and 3), and the presumed antiferromagnetically ordered spin-glass regions which are responsible for the hysteresis phenomena (see upper panel in Fig. 2 and the lower panel in Fig. 3) and sharp drop of resistivity upon the application of a relatively weak magnetic field (see lower panel in Fig. 2). From the data in Fig. 3, we can
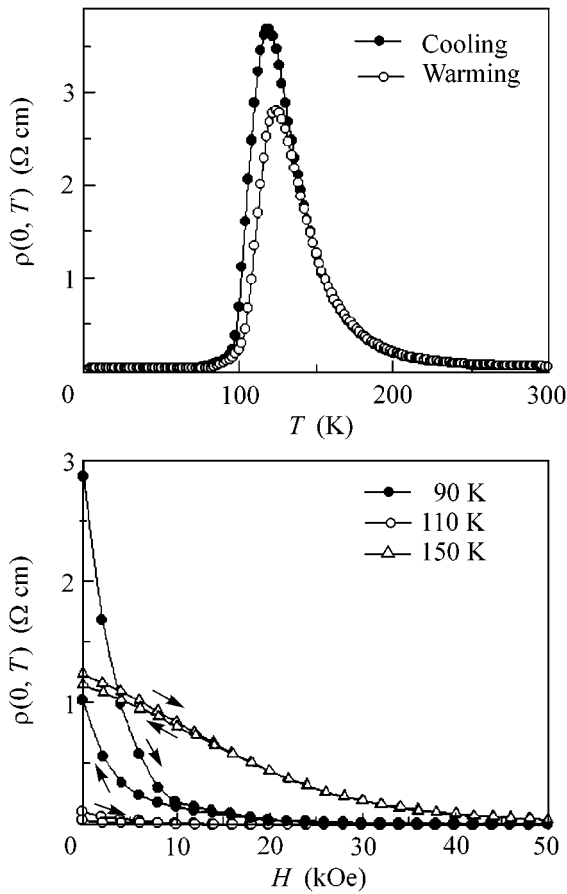
Fig. 2. Temperature variation of resistivity (top panel) and magnetoresistance (lower panel) for $La_{0.67}Ca_{0.33}MnO_3$ thin film annealed under 100-bar oxygen pressure.

Fig. 3. Magnetization curves for thin films at 5 K (top panel); zero-field-cooled (ZFC) and field-cooled (FC) magnetizations recorded in a field of 200 Oe for $La_{0.67}Ca_{0.33}MnO_3$ thin film annealed under high oxygen pressure.

estimate the volume of the ferromagnetic phase in the sample annealed under high oxygen pressure to be ≈0.56 of that in the as-prepared film. The most important fact reported here is the absolutely different nature of the phase-separated state observed. According to the known pictures of phase separation in manganites proposed theoretically [7] and observed in thin films [8], the matrix must consist of the antiferromagnetically ordered insulating phase with small ferromagnetic conductive regions. The phase-separated state observed in our films differs also from the spin-glass state observed in the bulk $Y_{0.7}Ca_{0.33}MnO_3$ material [9], where it is caused by the strain effects associated with the Mn–O–Mn bond angle reduction and variations in one-electron bandwidth (W) of the e_g band owing to the small size of doping cation. The bulk $Y_{0.7}Ca_{0.33}MnO_3$ material is insulating over the whole temperature range. As is clearly seen from the upper panels in Figs. 2 and 3, in our case the major part of the film volume is occupied by the conductive ferromagnetic phase.

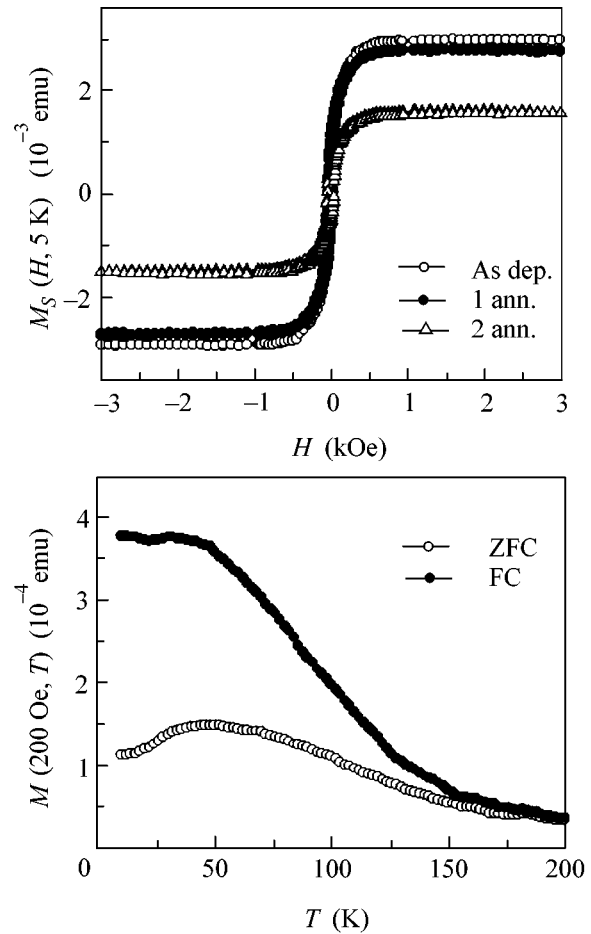Theoretical description of the phase diagram of doped manganites is usually carried out using the following parameters: the nearest neighbor hopping amplitude t for e_g electrons, Hund's coupling J_H, antiferromagnetic coupling between the localized t_{2g} spins J_{AF}, and on-site Coulomb interaction U [10–14]. In the conventional "double-exchange" models, J_H is often considered as infinite and U is neglected. The results of calculations within the ferromagnetic Kondo lattice [11, 12], mean-field [13], and random-field Ising [14] models with allowance for the antiferromagnetic coupling show the possibility of phase separation for some values of the J_{AF}/t parameter. Coexistence of large-sized clusters of ferromagnetic conductive and antiferromagnetic insulating phases in manganese oxides was found to be possible [14] in the case where strong-coupling interactions (t and J_{AF}), which are necessary to produce the ordered phases, are modified by the quenched disorder caused by chemical substitution (or high-pressure oxygen treatment, as in our case) due to the buckling of MnO_6 octahedra and reduction of the Mn–O–Mn bond angle.

In summary, for pulsed laser-deposited $La_{0.67}Ga_{0.33}MnO_3/(100)MgO$ thin films, we have demonstrated experimentally the instability of the classical "double-exchange" ferromagnetic conductive state towards combined influence of two perturbations: high-pressure oxygen treatment and large film–substrate strain effects. The resulting new phase-separated state consists of two phases: ferromagnetic matrix and spin-glass-like inclusions.

REFERENCES

1. J. Coey, M. Viret, and S. von Molnar, Adv. Phys. **48**, 167 (1999).
2. G. Xiong, Q. Li, H. Ju, S. Mao, *et al.*, Appl. Phys. Lett. **66**, 1427 (1995).
3. Y. Shapira, S. Foner, and T. Reed, Phys. Rev. B **8**, 2299 (1973).
4. E. Wollan and W. Koehler, Phys. Rev. **100**, 545 (1955).
5. A. Arulraj, R. Mahesh, G. Subbana, *et al.*, J. Solid State Chem. **127**, 87 (1996).
6. C. Zener, Phys. Rev. B **82**, 403 (1951).
7. E. L. Nagaev, Usp. Fiz. Nauk **166**, 833 (1996) [Phys. Usp. **39**, 781 (1996)].
8. A. Biswas, M. Rajeswari, R. C. Srivastava, *et al.*, Phys. Rev. B **63**, 184 424 (2001).
9. X. L. Wang, J. Horvat, H. K. Liu, *et al.*, J. Magn. Magn. Mater. **182**, L1 (1998).
10. Yu. A. Izyumov and Yu. N. Skryabin, Usp. Fiz. Nauk **171**, 121 (2001).
11. S. Yunoki and A. Moreo, Phys. Rev. B **58**, 6403 (1998).
12. E. Dagotto, S. Yunoki, A. L. Malvezzi, *et al.*, Phys. Rev. B **58**, 6414 (1998).
13. D. I. Golosov, M. R. Norman, and K. Levin, cond-mat/9712094.
14. A. Moreo, M. Mayr, A. Feiguin, *et al.*, Phys. Rev. Lett. **84**, 5568 (2000).